

Doctoral Thesis
Validating Microclimate Simulations to Quantify the Cooling Effect of Green Facades

submitted in satisfaction of the requirements for the degree of
Doctor of Science
of the Vienna University of Technology, Faculty of Civil and Environmental Engineering

Dissertation
Validierung von Mikroklimasimulationen zur Quantifizierung der Kühlwirkung von Fassadenbegrünungen

ausgeführt zum Zwecke der Erlangung des akademischen Grades eines
Doktors der technischen Wissenschaften
eingereicht an der Technischen Universität Wien, Fakultät für Bau- und
Umweltingenieurwesen
von

Florian Teichmann
Matrikelnummer 1527388
Bloch-Bauer-Promenade 24/1/118, A-1100 Wien

Betreuerin: Univ. Prof. Dipl.-Ing. Dr. techn. Azra Korjenic
Forschungsbereich Ökologische Bautechnologien
Institut für Werkstofftechnologie, Bauphysik und Bauökologie
Technische Universität Wien
Karlsplatz 13/207-03, 1040 Wien

Gutachterin: Univ. Prof. in Dipl.-Ing. in Dr. in techn. Kristina Orehounig
Institut für Architekturwissenschaften
Technische Universität Wien
Karlsplatz 13/259-03, 1040 Wien

Gutachterin: Priv.-Doz. Dipl.-Ing. Dr. Ulrike Pitha
Institut für Ingenieurbiologie und Landschaftsbau
Universität für Bodenkultur Wien
Peter-Jordan-Straße 82/III, 1190 Wien

Wien, März 2024

Kurzfassung

Die Untersuchung der Kühlwirkung von Fassadenbegrünungen ist von zunehmendem Interesse, da diese in Anbetracht der sich verschärfenden Auswirkungen des Klimawandels als potenzielle Kompensationsmaßnahme angesehen werden. Zur quantitativen Beurteilung dieses Effekts können bereits in der Planungsphase Mikroklimasimulationen herangezogen werden. Dabei wird neben der Kühlwirkung auch die Auswirkung auf die Luftfeuchtigkeit sowie Luftbewegung im Nahbereich der Fassadenbegrünung berücksichtigt. Die Richtigkeit des Ergebnisses von Mikroklimasimulationen ist naturgemäß abhängig von der Qualität der Eingaben sowie von den getroffenen Annahmen. Je höher der Detaillierungsgrad, desto länger dauert die Simulation – ein geringerer Detaillierungsgrad bringt jedoch eine Zunahme des mittleren Fehlers mit sich. Es muss daher die Frage beantwortet werden: Wie genau muss die Simulation sein und wie lässt sich die Genauigkeit der Simulation bestimmen?

Zur Beantwortung dieser Fragestellung werden im Rahmen dieser Dissertation Vereinfachungen in der Berücksichtigung von unterschiedlichen Bauweisen und Freiraumaufbauten analysiert und anschließend dynamische Wind- und Mikroklimasimulationen von drei begrünten Wiener Schulen mit der Software "uhSolver" durchgeführt und mit Messdaten vor Ort verglichen. Der manuelle Aufwand der Modellerstellung konnte durch die Reduzierung der Parametervielfalt minimiert werden, ohne die Genauigkeit der Simulationsergebnisse wesentlich zu beeinflussen. Die Ergebnisse weisen auf eine sehr geringe Temperaturreduktion bis wenige Zentimeter vor der Fassadenbegrünung hin. Aufgrund der geringen zu messenden Temperaturunterschiede kommt der Genauigkeit der verwendeten Sensoren eine besondere Bedeutung zu. Da Fassadenbegrünungen oft nach Süden ausgerichtet sind, ist mit einem hohen Strahlungseintrag auf die Sensoren vor den begrünten Fassaden zu rechnen. Dies kann bei natürlich belüfteten Strahlenschutzschirmen zu einem erheblichen Messfehler führen. In diesem Zusammenhang wird ein neu entwickelter Strahlenschutzschirm mit mechanischer Belüftung vorgestellt und auf dessen Eignung zur Messung der Lufttemperatur vor besonnten Fassaden untersucht.

Die Validierung von Mikroklimasimulationen zur Quantifizierung der Kühlwirkung von Fassadenbegrünungen ist ein wichtiger Schritt, um das Potenzial dieser grünen Infrastruktur für die Verbesserung des städtischen Mikroklimas zu verstehen. Diese Dissertation evaluiert die Genauigkeit von Simulationen mit der Software uhiSolver zur Bewertung der Auswirkungen von Fassadenbegrünungen auf das lokale Klima, mit einem Fokus auf Lufttemperatur, Luftfeuchtigkeit, Windgeschwindigkeit und reflektierte Solarstrahlung in städtischen Umgebungen. Diese Forschung ist entscheidend, um fundierte Aussagen zur Integration von Fassadenbegrünungen in städtische Planungen zu treffen und die Resilienz gegenüber Hitzeinseln und anderen klimatischen Herausforderungen zu verbessern.

Abstract

Investigating the cooling effect of facade greening is of increasing interest, as it is seen as a potential compensatory measure in view of the worsening effects of climate change. Microclimate simulations can already be used in the planning phase to quantitatively assess this effect. In addition to the cooling effect, the impact on air humidity and air movement in the vicinity of the facade greening is also taken into account. The accuracy of the results of microclimate simulations naturally depends on the quality of the input and the assumptions made. The higher the level of detail, the longer the simulation takes. However, a lower level of detail results in an increase in the mean error. The question must therefore be answered: How accurate does the simulation need to be and how can the accuracy of the simulation be determined?

To answer this question, this dissertation analyzes simplifications in the consideration of different construction methods and ground surfaces and then carries out dynamic wind and microclimate simulations of three greened Viennese schools using the "uhSolver" software and compares them with measurement data on site. The manual effort required to create the models was minimized by reducing the variety of parameters without significantly affecting the accuracy of the simulation results. The results indicate a very small temperature reduction up to a few centimetres in front of the facade greening. Due to the small temperature differences to be measured, the accuracy of the sensors used is of particular importance. As green facades are often south-facing, a high radiation input to the sensors in front of the green facades is to be expected. This can lead to a considerable measurement error with naturally ventilated radiation shields. In this context, a newly developed radiation shield with mechanical ventilation is presented and its suitability for measuring the air temperature in front of sunny facades is examined.

The validation of microclimate simulations to quantify the cooling effect of facade greening is an important step towards understanding the potential of this green infrastructure to improve the urban microclimate. This dissertation evaluates the accuracy of simulations using the uhSolver software to assess the impact of facade greening on local climate, with a focus on air temperature, humidity, wind speed and reflected solar radiation in urban environments. This research is crucial to make informed statements on the integration of green facades into urban planning and to improve resilience to heat islands and other climatic challenges.

Inhalt

Kurzfassung	3
Abstract	5
1 Ausgangssituation und Problemstellung	1
1.1 Stadtklima.....	1
1.2 Mikroklimasimulationen	2
1.3 Modellierung von Begrünung.....	2
1.4 Validierung von Mikroklimasimulationen	5
2 Ziele	7
3 Methodik	9
3.1 Generierung von vereinfachten Materialdaten und Sensitivitätsanalyse.....	9
3.2 Mikroklimasimulationen mit uhiSolver	10
3.3 Entwicklung eines mechanisch belüfteten Strahlenschutzschirms und verwendete Messtechnik	13
4 Zusammenfassung der wissenschaftlichen Aufsätze	15
4.1 Erste Publikation.....	15
4.2 Zweite Publikation.....	17
4.3 Dritte Publikation	19
5 Wissenschaftlicher Beitrag der Dissertation	22
5.1 Ergebnisse.....	22
5.2 Beantwortung der Forschungsfragen.....	23
6 Fazit und Ausblick.....	28
7 Literatur	29
8 Anhang.....	34
8.1 Erste Publikation.....	34
8.2 Zweite Publikation.....	35
8.3 Dritte Publikation	36

1 Ausgangssituation und Problemstellung

1.1 Stadtklima

Der von den Menschen verursachte Klimawandel führt zu einer kontinuierlichen Zunahme der globalen Durchschnittstemperatur. Als wärmstes Jahr seit Beginn der Aufzeichnungen lag die globale Durchschnittstemperatur im Jahr 2023 bereits um 1,79 Grad Celsius über dem langjährigen Durchschnitt [1]. Zusätzlich zum Temperaturanstieg infolge des Klimawandels kommt es in Städten durch den sogenannten Urban Heat Island-Effekt (UHI-Effekt) zu einer zusätzlichen Erhöhung der Temperaturen im Vergleich zu den umliegenden ländlichen Gebieten. Zu den Hauptursachen gehören nach Yang et al. [2]:

- Bebauung und Versiegelung: Städte sind oft durch eine hohe Dichte von Gebäuden und versiegelten Oberflächen wie Asphalt und Beton gekennzeichnet. Diese Materialien absorbieren Wärme während des Tages und geben sie nachts langsam ab, was zu höheren nächtlichen Temperaturen führt.
- Weniger Vegetation: Im Vergleich zu ländlichen Gebieten gibt es in städtischen Gebieten weniger Vegetation wie Bäume und Grasflächen. Diese Vegetation spielt eine wichtige Rolle bei der Kühlung durch Verdunstung und Schattenbildung. Das Fehlen von Vegetation in städtischen Gebieten trägt daher zu höheren Temperaturen bei.
- Abwärme von Gebäuden und Verkehr: Die Aktivitäten in städtischen Gebieten, wie der Betrieb von Gebäuden, Industrieanlagen und Verkehr, erzeugen Wärme, die als Abwärme bezeichnet wird. Diese zusätzliche Wärme trägt zur Erhöhung der lokalen Temperaturen bei.

Auch die Stadt Wien hat mit den Auswirkungen des UHI-Effekts zu kämpfen. Aus diesem Grund wurde im Jahr 2015 der "Urban Heat Islands Strategieplan Wien" (UHI-STRAT Wien) [3] ins Leben gerufen. Darin werden konkrete Maßnahmen zur Reduktion des UHI-Effekts sowie zur Verbesserung des Stadtklimas angeführt und zentrale Handlungsebenen des UHI-STRAT Wien identifiziert. Ziel des UHI-STRAT Wien ist es, die konsequente Berücksichtigung stadtklimatischer Aspekte auf verschiedenen Planungsebenen zu integrieren. Zu den Zielen des Handlungsfeldes "Stadtstruktur und Lebensqualität" gehört die Verfolgung von Maßnahmen zur Steigerung der Lebensqualität im bebauten Stadtgebiet (Begrünung von Straßenräumen, Höfen und Dächern, Verringerung der Bodenversiegelung, Aufwertung von Grün- und Freiflächen) [4]. Es wird jedoch nicht darauf eingegangen, wie stark die einzelnen Maßnahmen zur Reduzierung des UHI-Effekts beitragen und in welchem Maße die Behaglichkeit im Nahbereich der Begrünungsmaßnahmen dadurch beeinflusst wird.

1.2 Mikroklimasimulationen

Um die Effektivität von städtischen Begrünungsmaßnahmen bereits im Vorfeld zu bewerten, können dynamische, dreidimensionale Mikroklimasimulationen durchgeführt werden. Diese basieren meist auf der Methode der numerischen Strömungsmechanik (englisch: Computational Fluid Dynamics, Abk.: CFD) und bieten eine rechnerische Annäherung an die Gleichungen, die die Luftströmung in der städtischen Struktur bestimmen [5]. Die meistverwendeten Programme sind ENVI-met, ANSYS und Phoenics [6]. Während die letzteren beiden allgemeine CFD-Plattformen darstellen, die dem Anwender ein hohes Maß an Simulationsexpertise abverlangen, ist ENVI-met eine rein auf Mikroklimasimulationen spezialisierte Software, die mit etwas weniger Vorwissen angewendet werden kann. Deren Anwendung beschränkt sich jedoch aufgrund hoher Lizenzkosten und hoher Anforderungen an die CPU-Leistung auf spezialisierte Ingenieurbüros. Weitere Einschränkungen von ENVI-met sind nach Stavrakakis et al. [6] die Beschränkung auf kartesische Geometrien und strukturierte Gitter sowie die begrenzten Turbulenzmodellierungsoptionen.

Mit einer horizontalen Auflösung von 0,5 m bis 10 m ist ENVI-met für mikroskalige Simulationen zur Analyse der Wechselwirkungen zwischen einzelnen Gebäuden, Oberflächen und Pflanzen ausgelegt [7]. Durch vereinfachte Eingabe der Wandaufbauten von Gebäuden mit bis zu drei verschiedenen Materialien ist auch eine grobe Abschätzung der Energiebilanz und damit der Temperatur innerhalb einzelner Gebäude möglich. Hierfür werden die Gebäude als leere Luftvolumen betrachtet. Weder die Wärmespeicherkapazität von Elementen im Gebäude noch die internen Wärmeströme werden berücksichtigt [8].

Die Berücksichtigung von Pflanzen und den damit zusammenhängenden physikalischen Effekten (Evapotranspiration und Schattenwurf in Abhängigkeit der Solarstrahlung bzw. der Jahreszeit) in Mikroklimasimulationen ist Thema aktueller Forschung. Im folgenden Abschnitt wird auf die unterschiedlichen Ansätze eingegangen.

1.3 Modellierung von Begrünung

Bisherige Modelle zur Integration von Begrünung in Mikroklimasimulationen beschränken sich in erster Linie auf Bäume oder Dachbegrünung. Dabei wird oft auf die Software ENVI-met zurückgegriffen, wie dies Deng et al. in ihrer Studie zum Einfluss von Stadtbäumen auf das Mikroklima, die thermische Behaglichkeit und die Temperatur von Gebäudefassaden getan haben [9]. Sie haben damit aufgezeigt, dass Bäume das Mikroklima und den thermischen Komfort auf mindestens drei Arten beeinflussen: Einerseits tragen sie durch Evapotranspiration zur Reduktion der Lufttemperatur bei; weiters schützen sie an sonnigen Tagen vor direkter Solarstrahlung; und zuletzt beeinflussen sie die Windströmung in Abhängigkeit ihrer Anordnung sowie der Windrichtung, wobei es sowohl zu einer Erhöhung (Windkanaleffekt) als auch einer Reduktion (Barrikadeneffekt) der Windgeschwindigkeit

kommen kann. Durch Koppelung von CFD-Simulationen mit einem sogenannten Canopy Energy Balance-Modell haben Li et al. außerdem gezeigt, dass eine Erhöhung der Windgeschwindigkeit die kühlende Wirkung von Bäumen abschwächt [10]. Weiters sei der Einfluss der Solarstrahlung auf die Blattoberflächentemperatur (englisch: Leaf Surface Temperature, Abk.: LST) größer als auf die Lufttemperatur. Um die Auswirkungen von Umweltveränderungen auf die LST abschwächen, seien Bäume jedoch in der Lage, den stomatären Widerstand zu regulieren und damit einen größeren Kühleffekt zu initiieren. Als wesentliche Einflussfaktoren von Bäumen auf das städtische Mikroklima nennen Xu et al. die geometrischen Merkmale des Baumes, die Baumart und Laubverteilung, Blatttyp, Transpirationsrate, stomatäre Leitfähigkeit sowie Standort- und Umgebungs faktoren [11], [12]. Diese Faktoren sollten bei Baumrekonstruktionen in Mikroklimasimulationen einbezogen werden, um eine realistische Simulation des städtischen Mikroklimas zu ermöglichen. Ein eindimensionales Gebäudeeffekt-Parametrisierungsmodell zur Abbildung der Mikroklimaeffekte von Bäumen (Abk.: BEP-tree) wurde von Segura et al. vorgestellt [13]. Darin wird die Wechselwirkung von Bäumen mit der ein- und ausgehenden Strahlung innerhalb von Straßenschluchten auf der Grundlage eines vertikalen Blattdichte profils und einer durchschnittlichen Baumverteilung innerhalb der Straßenschluchten parametrisiert. Das mehrschichtige Strahlungsmodell von BEP-tree verwendet Ray-Tracing, um die direkte kurzwellige Exposition aller städtischen Elemente innerhalb der Straßenschluchten in jedem Zeitschritt zu bestimmen. BEP-tree umfasst auch eine Parametrisierung der Auswirkungen von Gebäuden und Bäumen auf die Luftströmung innerhalb der Straßenschluchten.

Die Studien zu Gründächern beschäftigen sich meist mit deren Auswirkung auf die Energiebilanz des Gebäudes oder aber auf den UHI-Effekt auf Stadtbene. Der Einfluss auf das Mikroklima auf Nachbarschaftsebene wurde erstmals von Peng und Jim im Jahr 2012 mithilfe der Simulationsprogramme ENVI-met und RayMan untersucht [14]. Ebenfalls anhand von ENVI-met-Simulationen hat Berardi den Kühleffekt von Gründächern in der Gebäudesanierung analysiert. Er weist auf eine Erhöhung der Kühlwirkung von bis zu 0,4 °C auf Fußgängerebene bei Erhöhung des Blattflächenindex (englisch: Leaf Area Index, Abk.: LAI) hin [15]. Dabei kann es nach Fachinello Krebs et al. von Vorteil sein, wenn die Gründachflächen von Bäumen oder anderen Objekten verschattet werden, da dies die Kühlwirkung des Gründaches um mehr als 50 % erhöhen kann [16]. Berücksichtigt wurden die Pflanzenparameter LAI, Pflanzenhöhe, Blatt-Reflektivität und minimaler stomatärer Widerstand sowie die Substratparameter Substrathöhe, Leitfähigkeit, Dichte und spezifische Wärmekapazität des trockenen Bodens, volumetrischer Sättigungsfeuchtegehalt und Restfeuchtegehalt sowie anfängliche volumetrische Feuchte.

Der Einfluss von Bäumen, Gründächern und Grünwänden auf den thermischen Komfort auf Fußgänger niveau wurde von Geletic et al. anhand des Universal Thermal Climate Index (UTCI) untersucht. Die wirksamste Maßnahme zur Erhöhung des Komforts im öffentlichen Raum seien demnach Allee bäume,

die eine mittlere Temperaturreduktion von 0,3 °C und eine Reduktion des UTCI um 0,6 °C bewirken können [17]. Die Studie unterstreicht jedoch auch die sehr stark ortsabhängige Kühlwirkung von Bäumen, welche direkt unter den Bäumen bis zu 5 °C und bezogen auf den UTCI sogar bis zu 15,1 °C betragen kann. Im Vergleich dazu würde die Berücksichtigung von begrünten Wänden und Dächern zu vernachlässigbaren Ergebnissen in Bezug auf die Reduzierung des UTCI sowie der Lufttemperatur führen. Die Simulationen wurden in dieser Studie mit dem Stadtklimamodell PALM-4U durchgeführt, welches eine Erweiterung des Parallelized Large-Eddy Simulation Model (PALM) der Leibniz Universität Hannover ist, das auf der Programmiersprache Fortran 95 beruht [18]. Das PALM-Modell berücksichtigt die vielfältigen Auswirkungen von Pflanzen nach Krc et al. [19] folgendermaßen: Die dynamischen Auswirkungen auf die turbulente Strömung werden als eine zusätzliche Senke für den Impuls modelliert, wobei Baumblätter die Strömungswirbel auf der Untergitterskala beeinflussen. Die Auswirkungen auf die Untergitterturbulenz werden berücksichtigt, indem eine ähnliche Senke zum Untergittermodell hinzugefügt wird. Die Auswirkungen auf kurz- und langwellige Strahlungsintensitäten werden durch das Strahlungstransportmodell entsprechend den optischen Eigenschaften der 3D-Struktur der Blätter, beschrieben durch die Blattflächendichte (engl.: Leaf Area Density, Abk.: LAD), berechnet. Der sensible Netto-Wärmestrom (Differenz aus auf die Blätter einfallender, transmittierter und emittierter Strahlung) wird folglich von der Umgebungsluft absorbiert. Der latente Wärmestrom wird nach der Jarvis-Stewart-Methode [20] berechnet, während die erforderlichen kurzwelligen Strahlungsflüsse durch das Strahlungstransportmodell bereitgestellt werden.

Mit einem Fokus auf die Modellierung der mikroklimatischen Auswirkungen von Bäumen sowie begrünten Dächern und Fassaden in ENVI-met betonten Liu et al. die Bedeutung einer genauen ENVI-met-Vegetationsmodellierung [21]. Dabei wurden zunächst zahlreiche Sensitivitätstests unter heißen und feuchten Klimabedingungen durchgeführt, um die mikroklimasensiblen Parameter und ihre relative Kühlwirkung auf Fußgängerebene zu ermitteln. Die Ergebnisse zeigten, dass die Blattflächendichte (LAD) der wichtigste Parameter bei der Modellierung von ENVI-met-Bäumen ist. Die Eingabegenaugigkeit der Wurzeleigenschaften beeinträchtigte die Gesamtqualität der Simulation auf Fußgängerebene jedoch nur unwesentlich. Für die Modellierung von Gründächern und begrünten Fassaden haben sich der Blattflächenindex (LAI) und die Blattwinkelverteilung als relevant herausgestellt, um eine hohe Simulationsqualität zu gewährleisten. Die Modellierungsparameter für Grünfassaden in ENVI-met sind in Tabelle 1 aufgelistet. Die nach Liu et al. typischen Modellierungsparameter für Gründächer und Grünfassaden, die sich aus einer umfangreichen Literaturrecherche von ENVI-met-Fallbeispielen ergeben haben, sind in Tabelle 2 angeführt.

Tabelle 1. Modellierungsparameter für Fassadenbegrünung in ENVI-met nach [21].

Begrünungseigenschaften	Eigenschaften der Pflanze	Subrateigenschaften
Pflanzenschichtdicke	Art der CO ₂ -Bindung	Substratschichtdicke
Blattflächenindex	Blatt-Typ	Emissivität des Substrats
Blattwinkenverteilung	Albedo	Albedo des Substrats
	Lichtdurchlässigkeit	Wasserbereitstellungskoeffizient
	Pflanzenhöhe	Luftspalt zwischen Substrat und Wand
	Wurzelschichtdicke	
	Blattdichtheprofil	
	Wurzeldichtheprofil	
	Saisonale Veränderung	

Tabelle 2. Mittlere Parameterwerte für Dach- und Fassadenbegrünung in ENVI-met nach [21].

Parameter	Mittelwert
Blattflächenindex in m ² /m ²	3,15
Blattwinkenverteilung	0,5
Emissivität des Substrats	0,93
Albedo des Substrats	0,28
Wasserbereitstellungskoeffizient	0,5
Luftspalt zwischen Substrat und Wand in m	0,06

1.4 Validierung von Mikroklimasimulationen

Um die Genauigkeit von Mikroklimasimulationen zu bestätigen, werden die Simulationsergebnisse meist im Rahmen von Fallstudien mit Vor-Ort-Messdaten verglichen und mittlere Abweichung zwischen Simulation und Messung berechnet. Diese Abweichung wird sodann als mittlerer Fehler der Simulation tituliert. Den möglichen Fehlerquellen bei der Messung wird dabei oft nur eine untergeordnete Bedeutung beigemessen, wie dies die nachfolgende Auflistung möglicher Gründe für die Abweichungen zwischen Simulation und Messung in einer Fallstudie von Antoniou et al. zeigt, bei der CFD-Simulationen auf Basis der instationären Reynolds-gemittelten Navier-Stokes (engl.: Unsteady Reynolds-Averaged Navier-Stokes , Abk.: URANS)-Gleichungen zur Vorhersage des Mikroklimas in einem Bezirk in Nicosia, Zypern, verwendet wurden [22]:

- vereinfachte Spezifikationen für Baumaterialien;
- Vernachlässigung von Bäumen und Grünflächen;
- geometrische Vereinfachungen in der Abbildung von Fassaden;
- Verwendung von Standard-Wandfunktionen für die Modellierung von Strömungsparametern in wandnahen Bereichen anstelle eines Modellierungsansatzes mit niedriger Reynoldszahl;
- Unzulänglichkeiten des RANS-Ansatzes;
- Verwendung eines vereinfachten Strahlungsmodells.

Alle angeführten Punkte zielen ausschließlich auf die Ungenauigkeit der Simulation ab. Die Messungenauigkeit der Lufttemperaturmessung wird lediglich mit $\pm 1\%$ angegeben und nicht weiter reflektiert. Nach Venkateshan sind jedoch systematische Fehler bei der Temperaturmessung aufgrund der begrenzten Wärmeübertragungsrate zwischen dem System, dessen Temperatur gemessen wird, und dem Sensor, der es abfragt, unvermeidlich [23]. Mögliche Fehlerquellen bei Temperaturmessungen könnten demnach sein:

- Leistungsfehler bei der Oberflächentemperaturmessung (der Sensor stört den Prozess);
- Strahlungsfehler (der Sensor stört sowohl den Prozess als auch andere Umgebungen);
- Fehler aufgrund von Konvektions- und Leitungsprozessen bei sich bewegenden Flüssigkeiten;
- Fehler durch viskose Dissipationseffekte bei hohen Strömungsgeschwindigkeiten.

Die komplizierte Beziehung zwischen verschiedenen Umweltfaktoren und der Temperatur ist bereits in zahlreichen Studien untersucht worden. Avraham et al. postulieren einen deutlichen und schnellen Zusammenhang zwischen Lufttemperaturmessungen und Änderungen der absoluten Luftfeuchtigkeit, welcher auf die Strahlungsleistung zurückgeführt wird [24]. Wie Erell et al. betonen, kann das Vorhandensein von kurz- oder langwelliger Strahlung zu inakzeptablen Fehlern bei der Messgenauigkeit führen [25]. Direkte Sonneneinstrahlung auf die Oberfläche des Temperatursensors heizt den Sensor auf und erhöht die Temperatur um ihn herum im Vergleich zur Umgebungsluft. Um dies abzumildern, werden in Wetterstationen üblicherweise Strahlenschutzschirme vor den Temperatursensoren angebracht. Durch die Alterung der Beschichtungen verringert sich jedoch deren Fähigkeit, Sonnenlicht zu reflektieren, was zu Fehlern von bis zu $1,63\text{ }^{\circ}\text{C}$ führt [26]. Darüber hinaus kann eine verringerte Luftzirkulation in nicht belüfteten Strahlenschutzschirme die Reaktionsgeschwindigkeit des Sensors beeinträchtigen, was an klaren, windstillen Tagen zur Mittagszeit zu einem Temperaturfehler von $2\text{-}4\text{ }^{\circ}\text{C}$ führt [27]. Zusammenfassend lässt sich sagen, dass für das Verständnis der Genauigkeit von Temperaturmessungen die Berücksichtigung zahlreicher Umweltfaktoren erforderlich ist.

2 Ziele

Die vorliegende Dissertation beschäftigt sich mit der Validierung von Mikroklimasimulationen zur Quantifizierung der Wirkung von Fassadenbegrünung auf das Klima sowie die Behaglichkeit im unmittelbaren Nahbereich. Dabei werden Messdaten von Sensoren im Nahbereich von Fassadenbegrünungssystemen mit den Simulationsergebnissen einer neuartigen Software zur Mikroklimasimulation verglichen, welche – im Vergleich zu gängiger Mikroklimasimulationssoftware – eine detailliertere Geometrieeingabe mit hoher Auflösung erlaubt. Um die Rechenzeit für die Simulation dennoch in einem akzeptablen Rahmen zu behalten, werden hierfür die wesentlichen Einflussgrößen untersucht. Darauf aufbauend wird eine Methodik zur vereinfachten Eingabe der Materialien von Gebäude- und Bodenoberflächen vorgeschlagen und anhand einer Fallstudie (siehe Abschnitt 4.1) validiert. Im Zuge der Auswertung der Simulationsergebnisse erfolgt eine kritische Diskussion und Analyse der Gründe für die Abweichungen zwischen Simulation und Messung.

Im Rahmen einer weiteren Fallstudie (siehe Abschnitt 4.2) wird die vorab validierte Methodik mit dem Ziel der realistischen Abbildung von kleinskaliger Fassadenbegrünung und deren hygrothermischer Wirkung in Mikroklimasimulationen erneut angewandt. Die Genauigkeit der Simulationsergebnisse wird dabei anhand eines hochaufgelösten Rasters an Temperatur- und Feuchtesensoren verifiziert, welche mit einem neu entwickelten, 3D-gedruckten Strahlenschutzschirm mit mechanischer Belüftung ausgestattet sind, dessen Einsatztauglichkeit erstmals wissenschaftlich unter Beweis gestellt wird.

Der letzte Teil dieser Dissertation (siehe Abschnitt 4.3) widmet sich im Detail der Strahlenschutzwirkung des neu entwickelten Strahlenschutzschirms und hat zum Ziel, die Genauigkeit von Temperaturmessungen in der Sonne ohne, mit konventionellem unbelüfteten sowie mit dem neuen belüfteten Strahlenschutzschirm zu vergleichen. Ein besonderer Fokus wird dabei auf den Einfluss der Windgeschwindigkeit sowie Windrichtung auf den Strahlungsfehler in Abhängigkeit des verwendeten Strahlenschutzschirms gelegt.

Aus den oben angeführten Zielstellungen lassen sich folgende Forschungsfragen ableiten:

- Forschungsfrage 1: Hat Fassadenbegrünung einen Einfluss auf die hygrothermische Behaglichkeit im Außenraum?
- Forschungsfrage 2: Können Mikroklimasimulationen diesen Einfluss mit ausreichender Genauigkeit bestimmen und welche Genauigkeit kann in diesem Zusammenhang als ausreichend angesehen werden?
- Forschungsfrage 3: Was ist bei der Temperaturmessung vor Fassaden zu beachten, damit diese Messdaten zur Validierung von Simulationsergebnissen herangezogen werden können?

Um diese Fragen zu beantworten, werden eine Sensitivitätsanalyse der wesentlichen Parameter für eine ausreichend genaue Geometrie- und Materialeingabe sowie Mikroklimasimulationen von Schulgebäuden mit Fassadenbegrünung durchgeführt. Anschließend werden Messfehler von Temperaturmessungen in der Sonne analysiert. Die angewandte Methodik ist im nachfolgenden Abschnitt im Detail beschrieben.

3 Methodik

Im Zentrum dieser Dissertation stehen die Mikroklimasimulationen mit der Software uhiSolver, deren Modellstruktur sowie Vorteile gegenüber anderen Simulationsprogrammen in Abschnitt 3.2 beschrieben werden. Zuvor wird in Abschnitt 3.1 auf die Vorgangsweise bei der Generierung der vereinfachten Materialdaten sowie die Sensitivitätsanalyse eingegangen, welche die Grundlage für die Geometrie- und Materialeingabe im dreidimensionalen Simulationsmodell legt. Abschließend wird in Abschnitt 3.3 der neu entwickelte Strahlenschutzschild vorgestellt und die verwendete Messtechnik mit den jeweiligen Fehlermargen angeführt.

3.1 Generierung von vereinfachten Materialdaten und Sensitivitätsanalyse

Im Zuge einer Machbarkeitsstudie zur Entwicklung der Software uhiSolver wurden die Albedo, die Dichte, der Wärmedurchlasswiderstand und die spezifische Wärmespeicherkapazität von Gebäuden und Bodenflächen als wesentliche Parameter für die Simulation des städtischen Mikroklimas identifiziert. Diese Parameter werden verwendet, um das thermische Verhalten der verschiedenen, für Wien üblichen Gebäudetypen und Bodenoberflächen (siehe Tabelle 3) zu berechnen. Die Bodenschichten werden dabei nur bis zu einer Tiefe von 1 m berücksichtigt.

Tabelle 3. Für Wien repräsentative Gebäude- und Bodentypen zur Integration in uhiSolver

Gebäudetypen	Bodentypen
G1: Gründerzeitgebäude	B1: Asphaltstraße
G2: Betongebäude der 1970er-Jahre	B2: Betonstraße
G3: Ziegelgebäude der 1970er-Jahre	B3: gepflasterte Straße
G4: Betongebäude (Neubau)	B4: Schotterweg
G5: Ziegelgebäude (Neubau)	B5: Wiese

Um die Gebäude- und Bodentypen und deren Einfluss auf die Umgebungstemperatur in die Software uhiSolver zu implementieren, müssen diese in ihrer Komplexität so weit vereinfacht werden, dass das gesamte Gebäude als homogener Monolith mit – verglichen mit dem realen Gebäude – vergleichbaren Wärmespeichereigenschaften modelliert werden kann. Hierfür werden zuerst für jeden Gebäudetyp die Massen der einzelnen Außen- und Innenbauteile sowie die Gesamtgebäudemasse bestimmt. Dabei wird eine Fehlertoleranz von 5 % gewählt. Damit können Innenbauteile mit einem Massenanteil kleiner oder gleich 5 % der Gesamtmasse vernachlässigt werden. Anschließend wird ermittelt, welche Bauteile maßgebend zur Wärmespeicherung beitragen. Je nach Wärmedurchlasskoeffizient des Außenbauteils wird zwischen zwei Szenarien unterschieden: Szenario 1 für gut gedämmte Bauteile, bei denen nur die äußeren Schichten der Außenbauteile zur Wärmespeicherung beitragen; und Szenario 2 für schlecht gedämmte Bauteile, wo die Wärmespeicherung sowohl durch Außen- als auch durch Innenbauteile erfolgt.

Ausgehend von der festgelegten Fehlertoleranz von 5 % wird im Szenario 1 jener Punkt X der Konstruktion bestimmt, an dem der Temperaturgradient zwischen Außen- und Innentemperatur 95 % entspricht. In weiterer Folge wird die Wärmespeicherkapazität der Gebäudehülle nur bis zu diesem Punkt X berücksichtigt – alle weiter innen liegenden Schichten und Bauteile werden vernachlässigt. Im Fall von Szenario 2 müssen weitere Vereinfachungen vorgenommen werden, um das gesamte Gebäude ausschließlich durch die Gebäudehülle beschreiben zu können. Hierbei werden diejenigen Innenbauteile, deren Massenanteil > 5 % der Gesamtgebäudemasse ist und die zur Wärmespeicherung beitragen, als innerste homogene Schicht der Außenhülle modelliert. Dazu wird ein fiktives Material mit gewichteten Eigenschaften der Innenbauteile bestimmt. Die flächenbezogene effektive Wärmekapazität χ kann daraufhin gemäß ÖNORM EN ISO 13786 [34] nach Formel 1 ermittelt werden.

$$\chi = \frac{T}{2\pi} \cdot \left(\left| \frac{Z_{11}-1}{Z_{12}} \right| \right) \text{ mit } Z = Z_i \cdot \dots \cdot Z_2 \cdot Z_1. \quad (1)$$

χ flächenbezogene effektive Wärmespeicherkapazität des Bauteils in $J/(m^2K)$

Z Wärmeübertragungsmatrix

T Periodendauer in s

Der Boden kann ohne Vereinfachungen als Monolith betrachtet werden, der aus einem homogenen Körper und einer umgebenden Grenzfläche besteht. Für die Berechnung der Wärmespeicherkapazität ist das Verfahren dasselbe wie bei Gebäuden. Zunächst wird der Punkt X bestimmt und dann der wärmespeichernde Teil des Bodenaufbaus ermittelt.

Auf diesem Berechnungsmodell aufbauend wurden an einem fiktiven Gebäude eindimensionale Modellrechnungen für die Bestimmung der Temperatur und des Wärmestroms an der Gebäude- und Bodenoberfläche durchgeführt, um eine Tendenz für die verschiedenen Parameter (Temperaturen und Wärmestrom) in Abhängigkeit von Albedo, Wärmekapazität und Wärmedurchlasswiderstand abzuleiten. Die Modellrechnungen wurden in Microsoft Excel für nur zwei Zeitschritte von je einer Sekunde durchgeführt, um drei Datenpunkte zu erhalten, die eine Ableitung des dynamischen Verhaltens für die Temperatur und den Wärmestrom an der Gebäude- und Bodenoberfläche ermöglichen. Eine detaillierte Beschreibung der Modellrechnungen ist in [28] zu finden.

3.2 Mikroklimasimulationen mit uhiSolver

Die im Rahmen dieser Dissertation durchgeföhrten Mikroklimasimulationen wurden mit der Software uhiSolver der Rheologic GmbH durchgeföhr. uhiSolver basiert auf der OpenFOAM-Programmiersprache. Es kombiniert kompressible Fluidströmung, Auftriebseffekte aufgrund der Luftdichte, Wärmeleitung in Festkörpern (innerhalb von Gebäuden und im Boden), Solarstrahlung und den Verlauf

der Sonne, Schatten von Gebäuden und Vegetation, Evapotranspiration sowie die Beeinflussung der Luftströmung durch Vegetationszonen in einem Programm. Genauso wie ENVI-met und ANSYS verwendet uhiSolver einen vollständig gekoppelten Ansatz, d.h. das Gebäudevolumen interagiert mit der umgebenden Luftströmung in Bezug auf Strahlungswärmeübertragung, Wärmeleitung und advektiver Wärmeübertragung. Im Vergleich zu ENVI-met, ANSYS etc. hat uhiSolver einige Vorteile:

- solide Code-Basis mit langer Historie und regelmäßigen Updates;
- höhere Genauigkeit der Strömung in der Nähe von Gebäuden, Böden und architektonischen Details im Vergleich zu voxelisierten Simulationsmethoden aufgrund der Finite-Volumen-Methode und beliebig geformten Finite-Volumen-Zellen;
- Unterstützung allgemeiner sowie gekrümmter Gebäudeformen und moderner Architektur;
- Gebäudedetails, die kleiner als 0,5 m sind, können mit einer räumlichen Genauigkeit im Zentimeterbereich berücksichtigt werden;
- validierte Verdunstungsmodellierung (Verdunstung von feuchten Oberflächen und Kondensation auf glatten Oberflächen);
- die erzwungenen Einlassbedingungen können nach tatsächlichen meteorologischen Daten des simulierten Standorts modelliert werden;
- hochgradig skalierbare Software, die sowohl auf Einzelrechnern als auch auf Hochleistungscomputerclustern läuft;
- erreicht Echtzeit-Simulationsgeschwindigkeit für städtische Mikroklimafälle.

Die Geometriebasis ist eine Kombination aus öffentlich verfügbaren 3D-Daten und manueller Gebäudemodellierung, wobei Giebel in den Gebäudemodellen enthalten sind. uhiSolver kann alle 3D-Geometrien lesen, zu denen die OpenFOAM-Bibliothek in der Lage ist, hat aber keinen eigenen 3D-Modellierer. Die 3D-Modellierung erfolgt daher mit externen Programmen. Die räumliche Simulationsauflösung ist nicht einheitlich über das gesamte Simulationsvolumen: sie ist in der Nähe der Gebäude höher (in der Größenordnung von 0,3 m an der Gebäudeoberfläche) und in größerer Entfernung von den Gebäuden niedriger.

Neben der Interaktion von Strahlung und Luft mit den Gebäuden werden auch die vorhandenen Pflanzen (grüne Wände, Bäume) mit all ihren thermodynamischen Effekten wie Reflexion, Schatten und Evapotranspiration in die Simulation einbezogen. In der aktuellen Version von uhiSolver werden alle Vegetationszonen gleich behandelt:

- Die Evapotranspirationsrate wird durch die lokale Strahlungsdichte und die Trockenkugeltemperatur moduliert und durch die lokale relative Luftfeuchtigkeit (treibende Kraft) und die lokale Windgeschwindigkeit begrenzt.

- Für Strahlung (optische Absorptions- und Emissionskoeffizienten) und Impuls (über Porositätsterme) werden geeignete Senken-Terme verwendet.
- Die Absorption durch die Vegetation (Abschattung) wird mit Hilfe von Multiband-Absorptions- und Emissionskoeffizienten, d. h. der "optischen" Blattdichte, modelliert.
- Alle Substratmaterialien, die nicht in direktem Kontakt mit einem Gebäude stehen, werden in der aktuellen Version nicht berücksichtigt.

Im Rahmen des Vegetationsmodells in uhiSolver wird die Transpiration von Pflanzen wie folgt berücksichtigt: Der lokale Wasserdampfdruck und der Wasserdampfsättigungsdruck werden mit der Antoine-Gleichung berechnet, woraus sich der lokale Taupunkt und die Sättigungsfeuchte ableiten lassen. Die Verdunstungsrate ist gleich Null, wenn die lokalen Bedingungen gesättigt sind. Die maximale Evapotranspirationsrate wird erreicht, wenn die relative Feuchte sehr niedrig und der Evapotranspirationsmodulator (aufgrund von Temperatur und Strahlung) sehr hoch ist. Die spezifische Blattdichte geht in die Darcy-Forchheimer-Koeffizienten der porösen Zone der Volumenzellen ein, die die Vegetation bezeichnen, sowie in die Absorptions- und Emissionskoeffizienten für die Dämpfung der Sonnenstrahlung (Beschattung) der genannten Volumenzonen. Die Wärme für die Evapotranspiration wird direkt aus der finiten Volumenzelle entnommen (unter Berücksichtigung der thermodynamischen Eigenschaften der Gasmischung). Der lokale Zustand wird sofort aktualisiert und die Berechnung geht im nächsten Zeitschritt weiter.

Eine Übersicht über die Modellstruktur von uhiSolver ist in Abbildung 1 dargestellt.

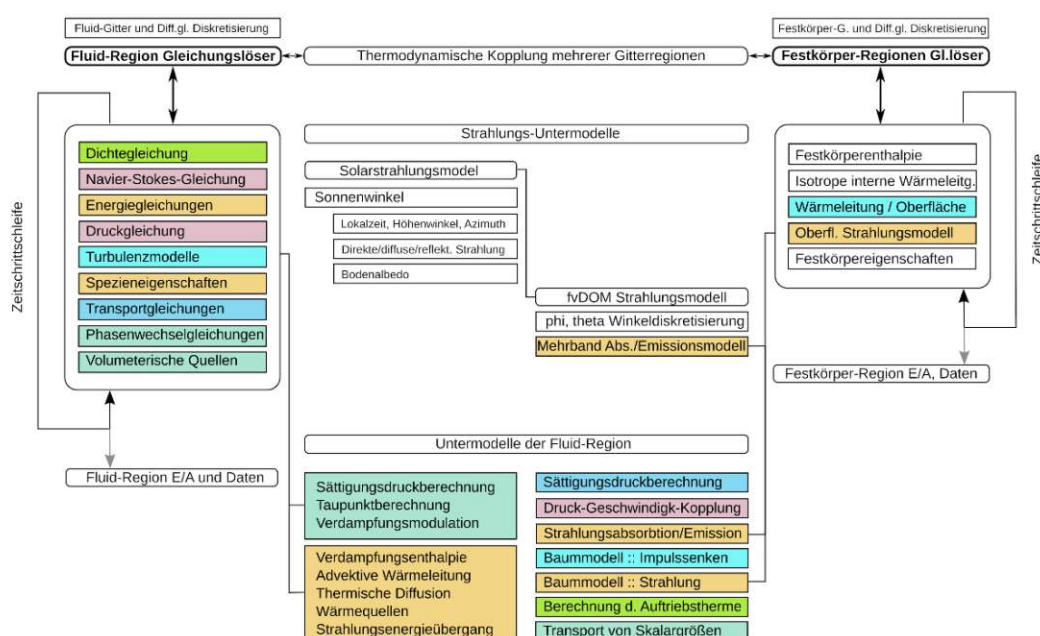


Abbildung 1. Modellstruktur von uhiSolver gemäß [29].

3.3 Entwicklung eines mechanisch belüfteten Strahlenschutzschirms und verwendete Messtechnik

Die in den Studien [30], [31] verwendeten belüfteten Strahlenschutzschirme wurden im Jahr 2022 an der TU Wien entwickelt, um Messfehler bei Temperaturmessungen mit maßgeblichem Strahlungseinfluss zu reduzieren. Zur Herstellung dieser Strahlenschutzschirme wurden insgesamt 7 Kunststoffteile mit einem 3D-Drucker gedruckt (Modell Ultimaker 2+, XYZ-Auflösung 12,5/12,5/5 Mikrometer). Diese können zusammen mit einem elektrischen Ventilator (Abmessungen $60 \times 60 \times 15$ mm, 4200 U/min, $0,58 \text{ m}^3/\text{min}$) und einem weiß lackierten, doppelwandigen Aluminiumgehäuse (Blechstärke 2 mm, Durchmesser 60 mm bzw. 80 mm) zu einem Strahlenschutzschirm zusammengesetzt werden (siehe Abbildung 2). Das Aluminiumgehäuse bietet eine wirksame Abschirmung von direkter und diffuser Solarstrahlung und heizt sich aufgrund der erzwungenen Luftströmung von mind. 3 m/s zwischen den beiden Aluminiumrohren weniger stark auf als unbelüftete Strahlenschutzschirme. Zur Messung von Temperatur und Luftfeuchtigkeit können die Rotronic HC2A-Sensoren von unten in den Strahlenschutzschirm eingeführt werden.

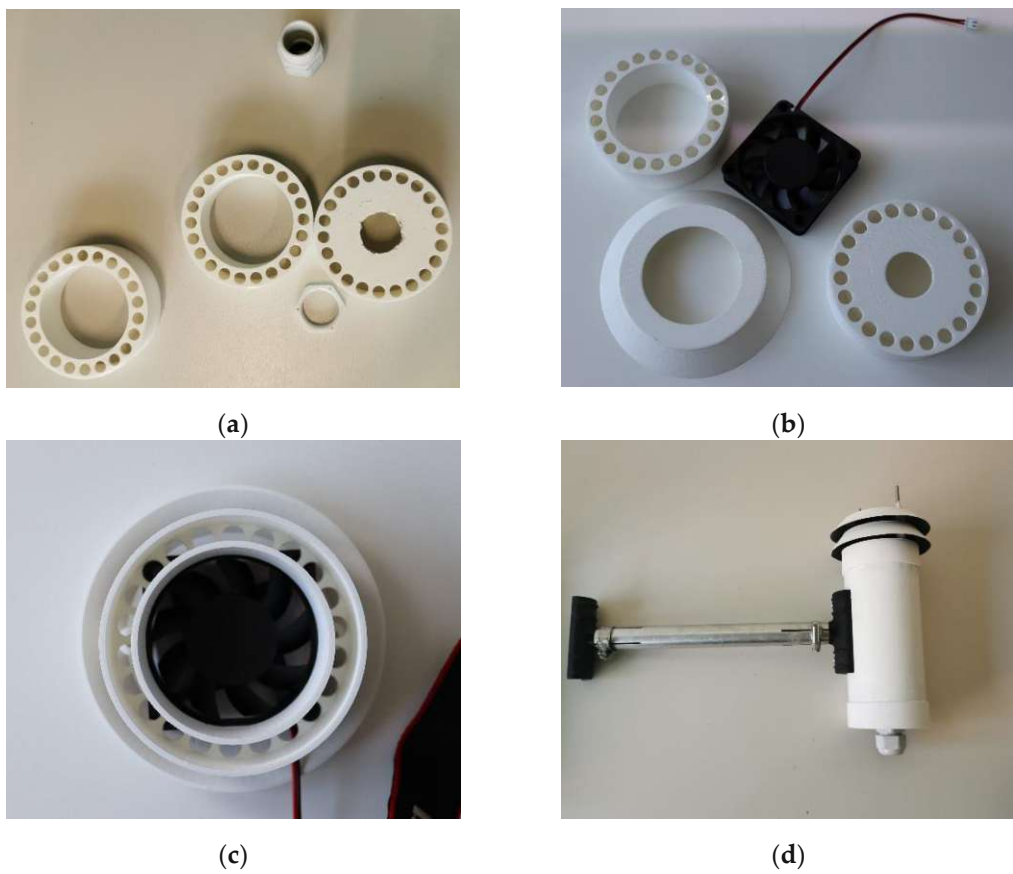


Abbildung 2. Aufbau des entwickelten, mechanisch belüfteten Strahlenschutzschirms: (a) Einzelteile aus dem 3D-Drucker; (b) Einzelteile einschließlich des Lüfters für den Deckel; (c) zusammengebauter Deckel; (d) montierter Strahlenschutzschirm.

Die drei im Rahmen dieser Dissertation durchgeführten Studien wurden mit unterschiedlicher Messtechnik durchgeführt (siehe Tabelle 4). Für Details zur Position und Montage der Sensoren wird auf die jeweiligen Publikationen verwiesen.

Tabelle 4. Für Wien repräsentative Gebäude- und Bodentypen zur Integration in uhiSolver

	Publikation 1	Publikation 2	Publikation 3
Datenlogger	Comnova RTR 53 A	Driesen + Kern DataCollectorXP-R bzw. Keysight DAQ970A	Keysight 34980A
Temperatur-/ Luftfeuchtesensoren	Lin Piccos A05	Rotronic HC2As	Rotronic HC2A Temperatur- und Feuchtefühler
Oberflächentemperatur- sensoren	PT1000-Fühler	PT1000-Fühler	PT1000-Fühler
Strahlenschutzschirme	unbelüftet	belüftet	belüftet
Wetterstation	-	Vantage Pro2 bzw. Vantage Pro2 Aktiv	Vantage Pro2 Plus

Die Rotronic HC2A Temperatur- und Luftfeuchtigkeitssensoren wurden bei einer Temperatur von 30 °C und einer Luftfeuchtigkeit von 35, 50 und 70 %rF unter Verwendung des Feuchtegenerators Rotronic HygroGen2 mit einer Stabilität von 0,1 %rF und 0,01 °C kalibriert.

In den folgenden Abschnitten werden die drei Publikationen, die den Kern dieser Dissertation bilden, vorgestellt und deren Ergebnisse zusammengefasst. Die vollständigen Artikel sind im Anhang zu finden.

4 Zusammenfassung der wissenschaftlichen Aufsätze

Die erste Publikation [29] untersucht den Einfluss von Bauweisen und Bodenoberflächen auf den städtischen Wärmeinsel-Effekt unter Zuhilfenahme der Simulationssoftware uhiSolver, wobei erstmals die Anwendbarkeit stark vereinfachter Annahmen von Gebäudematerialien für hinreichend genaue Simulationsergebnisse bestätigt wird. Die zweite Publikation [30] verwendet ebenfalls die Simulationssoftware uhiSolver, um die Kühlwirkung von kleinflächigen Fassadenbegrünungen sowie einer begrünten Pergola zu bewerten. Im Rahmen der dritten Publikation [31] werden die Messfehler bei Temperaturmessungen in der Sonne unter die Lupe genommen. Im Zuge dessen wird ein neu entwickelter Strahlenschutzschirm vorgestellt, mit dem die Messfehler deutlich reduziert werden können. Damit wird es in Zukunft möglich sein, eine noch bessere Datengrundlage für die Validierung von Mikroklima-Simulationssoftware bereitzustellen.

4.1 Erste Publikation

*Simulation des städtischen Mikroklimas mit uhiSolver: Validierung der Software
anhand vereinfachter Materialdaten*

Die erste Studie untersucht den Einfluss verschiedener Bauweisen und Bodenoberflächen auf den städtischen Wärmeinsel-Effekt (UHI-Effekt) angesichts der zunehmenden Urbanisierung und globalen Erwärmung. Ein OpenFOAM-basierter Solver namens "uhiSolver" ermöglicht es bereits in der Planungsphase, den Einfluss der städtischen Struktur, der verwendeten Baumaterialien und ihrer Oberflächen auf den UHI-Effekt zu beurteilen und durch gezielte Anpassung signifikant zu reduzieren. Dabei zeigt die Forschung, dass innere Gebäudedetails vernachlässigt werden können, während immer noch ausreichend genaue Ergebnisse erzielt werden. Die Studie gliedert sich in zwei Teile: Der erste Teil untersucht die Auswirkungen von Albedo, Wärmekapazität und thermischem Widerstand auf die Komponenten- und Oberflächentemperaturen von Gebäuden. Im zweiten Teil werden dynamische Wind- sowie Mikroklimasimulationen für einen Gründerzeit-Schulblock mit begrüntem Innenhof in Wien durchgeführt und mit vor-Ort-Messdaten verglichen. Trotz vereinfachter Annahmen für Gebäudematerialien zeigen die Simulationsergebnisse eine gute Übereinstimmung mit den Messdaten.

Im Detail werden die fünf relevantesten Gebäudetypen und Bodenoberflächen in Wien für die Berücksichtigung in uhiSolver herangezogen. Durch Fehlergewichtung und Sensitivitätsanalyse wird bestimmt, welche Parameter in jedem Fall wesentlich sind und welche vernachlässigt werden können. Schließlich werden die definierten Gebäudetypen und Bodenoberflächen in ihren inhomogenen

Materialeigenschaften so reduziert, dass sie im Computermodell als homogener Monolith mit bekannten Fehlermargen dargestellt werden können. Die dynamischen 3D-Simulationen im zweiten Teil bestätigen, dass die vereinfachte Annahme homogener Materialdaten für Gebäude sehr gute Ergebnisse liefert. Die Simulationen zeigen auch, dass die gefühlte Temperatur im begrünten Innenhof der Schule trotz niedrigerer Lufttemperatur manchmal wärmer wahrgenommen wird als in den benachbarten Straßen. Dies hängt mit der reduzierten Luftbewegung im geschlossenen Innenhof und der erhöhten Luftfeuchte zufolge der umfangreichen Gebäudebegrünungsmaßnahmen zusammen.

In einer vergleichbaren Studie von Antoniou et al. [22] wurden CFD-Simulationen des städtischen Mikroklimas für ein dicht besiedeltes Stadtviertel in Nikosia, Zypern, mithilfe der Unsteady Reynolds-Averaged Navier-Stokes (URANS)-Methode durchgeführt und anhand eines dichten Netzes von vor-Ort-Messungen der Lufttemperatur, Windgeschwindigkeit und Oberflächentemperatur an vier aufeinanderfolgenden Tagen im Juli 2010 validiert. Hierbei wurde gezeigt, dass die Vorhersagegenauigkeit der CFD-Simulationen einen durchschnittlichen absoluten Unterschied von 1,35 °C bei den Lufttemperaturen, 0,57 m/s bei den Windgeschwindigkeiten und 2,31 °C bei den Oberflächentemperaturen aufweist. Eine weitere Fallstudie von Maiullari et al. [32] verwendet einen Kopplungsansatz, der die Simulationstools ENVI-met und City Energy Analyst verbindet. Der Vergleich der Lufttemperatur der Wetterstationen und der durchschnittlichen Lufttemperatur von ENVI-met rund um die Gebäude eines städtischen Entwicklungsprojekts in der Stadt Zürich, Schweiz, zeigt eine maximale Abweichung von 2,5 °C hauptsächlich nachts an einem kühlen Tag und von 3 °C um 11 Uhr morgens an einem heißen Tag. Eine Koppelung von ENVI-met und EnergyPlus wurde von Natanian et al. [33] vorgenommen, um Energie- und mikroklimatische Modellierung für eine synergistische Bewertung auf Häuserblockebene im klimatischen Kontext von Tel Aviv zu verbinden. Ein Vergleich der Lufttemperatur für drei verschiedene Wetterdateien (EnergyPlus, Urban Weather Generator (UWG) und ENVI-met) für den 26. Juli zeigt für das Szenario mit der höchsten Bebauungsdichte für drei verschiedene Typologien (Innenhof-, Streu- und Hochhaus-Bebauung), eine nächtliche Lufttemperatursteigerung von bis zu 1,5 °C innerhalb der UWG-Datei im Vergleich zur ländlichen EnergyPlus-Datei. Die ENVI-met-Wetterdaten führten zu einer höheren nächtlichen Temperatursteigerung von bis zu 3 °C, jedoch auch um bis zu 1,5 °C niedrigeren Temperatur tagsüber. Einen ganz anderen Ansatz zur Vorhersage des Mikroklimas in Innenhöfen verwendeten Diz-Mellado et al. [34] mit der Verwendung eines Machine Learning-Modells. Support Vector Machines ausgewählt. Anhand von zwei ausgewählten Validierungsfällen im Süden Spaniens wurde für den Tagesabschnitt mit der höchsten städtischen Überhitzung ein relativer Fehler von ca. 0,05 % und ein Root-Mean-Square-Fehler (RMSE) von etwa 1 °C berechnet.

Verglichen mit den oben genannten Studien wurden mit der Software uhiSolver am Validierungsfall Kandlgasse gleich gute oder bessere Ergebnisse erzielt. Der absolute Fehler zwischen Messung und

Simulation lag trotz der angewendeten Vereinfachungen im Bereich von +/- 2 °C. Während im Validierungsfall Kandlgasse die Sensoren relativ nahe beieinander platziert waren (einige Meter) und ihre transiente Reaktion überwacht wurde, wurden in einem weiteren Validierungsfall in der Gablenzgasse in Wien verteilte Messorte (mit Abständen von zehn bis hundert Metern) zu verschiedenen festen Zeitpunkten betrachtet. Durch eine statistische Analyse der beiden Validierungsfälle können die Qualität der transienten Antwort (wie gut folgen die Simulationsergebnisse den gemessenen Werten) und die Qualität der räumlichen Antwort (wie gut passen die Simulationsergebnisse an verschiedenen Orten) voneinander getrennt analysiert werden. Sowohl räumliche als auch zeitliche Standardabweichungen der Temperaturdifferenzen liegen in beiden Validierungsfällen unter 1,00 °C. Die relative thermische Genauigkeit liegt im Bereich von 10 % für heiße, wolkenlose Tage im Vergleich zu einer täglichen thermischen Schwankung von 10 °C. Eine Genauigkeit von 10 % kann für Planungswerzeuge in der Entwurfsphase als ausreichend angesehen werden.

4.2 Zweite Publikation

*Die Auswirkung von Begrünungsmaßnahmen kleinen Maßstabs auf das lokale
Mikroklima – eine Fallstudie an zwei Schulgebäuden in Wien*

In der zweiten Publikation wurde die Software uhiSolver verwendet, um die sommerlichen Kühlleffekte und die Feuchtigkeitsproduktion von kleinflächigen Fassadenbegrünungen und einer begrünten Pergola an zwei Wiener Schulen zu bewerten. Der Vergleich mit Messdaten vor Ort hat die Simulationsergebnisse bestätigt, welche keine signifikante Reduktion der Lufttemperatur zufolge der untersuchten Begrünungsmaßnahmen zeigen. An einem heißen Sommertag um 15 Uhr Ortszeit (MESZ) betrug die maximale Temperraturreduktion 0,3 °C in 0,1 m Entfernung von der Fassadenbegrünung und im Inneren der grünen Pergola. In Bezug auf die gefühlte Temperatur wurde unter der begrünten Pergola im Vergleich zur unbeschatteten Dachterrasse eine Absenkung um bis zu 4 °C festgestellt. Die Simulationsergebnisse zeigen also deutlich, dass es keinen signifikanten lokalen (0,5 m bis 3 m Abstand von der Wand) Effekt kleinskaliger begrünter Wände auf die thermodynamische sowie die wahrgenommene Temperatur gibt, abgesehen von Gebäudeschattierung und reduzierter Einstrahlung hinter der begrünten Wand. Die begrünte Pergola ist ein Sonderfall, da diese im Vergleich zu den begrünten Wänden wesentlich mehr Schatten spendet und dadurch einen größeren Einfluss auf die gefühlte Temperatur unter der Pergola ausübt. Dieser Effekt wird jedoch durch die Beschattung dominiert und nicht durch die Kühlwirkung und Evapotranspiration der Pflanzen.

Die Ergebnisse dieser Studie werden durch die Ergebnisse von Daemei et al. [35] unterstützt, die eine Temperaturreduktion von bis zu 0,36 °C um 12 Uhr mittags vor einer direkt nach Norden ausgerichteten begrünten Fassade nachgewiesen haben. Der gleiche Wert der Lufttemperaturreduktion wurde von Galagoda et al. [36] in einem Abstand von 1 m von nach Süden und Osten ausgerichteten begrünten Wänden gemessen, was auf eine größere Tiefenwirkung des Kühlungseffekts bei vertikalen Begrünungssystemen hinweist, die stärker der Sonneneinstrahlung ausgesetzt sind. Es scheint also offensichtlich zu sein, dass ein einzelnes vertikales Begrünungssystem, das nur eine Fläche von wenigen Quadratmetern bedeckt, nicht ausreicht, um die Umgebungslufttemperatur maßgeblich zu senken und den thermischen Komfort im Sommer zu erhöhen. Die Begrünung von Fassaden muss in viel größerem Maßstab angewendet werden, wobei eine geschätzte Lufttemperaturreduktion von 0,3 °C bei Anwendung von begrünten Fassaden mit einem Deckungsgrad von 50 % in einer ost-west-ausgerichteten mittelhohen Straßenschlucht [37] und etwa 1 °C vollflächiger Begrünung aller Fassaden bei sehr dichter und hoher Bebauung [38] zu erwarten ist. Die zusätzliche Verwendung von großvolumiger Vegetation wie Alleenbäumen könnte zu noch höheren Lufttemperaturreduktionen von bis zu 2 °C führen, insbesondere im Schatten der Bäume. Um wesentlich zu einer Reduzierung des UHI-Effekts in großen Städten beizutragen, ist eine Kombination von Begrünungssystemen mit anderen mikroklimatischen Maßnahmen erforderlich, wie z. B. Nebelduschen oder Springbrunnen, die eine lokale Lufttemperaturabnahme von maximal 7 °C ermöglichen [39]. Hierbei muss jedoch auch der Einfluss der erhöhten Luftfeuchtigkeit auf die gefühlte Temperatur berücksichtigt werden: Bei niedrigen Windgeschwindigkeiten wird die erhöhte Luftfeuchtigkeit zufolge von Begrünungssystemen und/oder der Wassersprays nicht abtransportiert, wodurch es trotz reduzierter Lufttemperatur zu einer Erhöhung der gefühlten Temperatur kommen kann. Um sicherzustellen, dass ein implementiertes Begrünungssystem die gewünschte Wirkung auf das Mikroklima hat, muss daher eine kombinierte Betrachtung der unterschiedlichen Effekte der Begrünung auf Lufttemperatur, Luftfeuchtigkeit, Oberflächentemperatur sowie Strahlungsintensität durchgeführt werden.

4.3 Dritte Publikation

Messfehler bei der Temperaturmessung in der Sonne

Die Validierung von Mikroklima-Simulationssoftware erfolgt oft durch den Vergleich von Simulationsergebnissen mit vor-Ort-Messungen. Die Verwendung hochwertiger Temperatursensoren mit einer geringeren Abweichung als der durchschnittliche absolute Fehler der Simulationssoftware ist entscheidend für eine zuverlässige Validierung. Zudem sind Temperatursensoren so gut wie möglich vor direkter Solarstrahlung zu schützen, um eine Verfälschung der Messergebnisse zu vermeiden. Hierfür werden Strahlenschutzschirme verwendet, die entweder natürlich oder mechanisch belüftet werden können. Aufgrund der deutlich höheren Kosten von mechanisch belüfteten Strahlenschutzschirmen werden diese jedoch nur für Spezialanwendungen verwendet. Diese Studie stellt einen belüfteten Strahlenschutzschirm vor, der mit geringem Kosteneinsatz mit dem 3D-Drucker hergestellt werden kann. Das Ziel ist es, die Genauigkeit von Temperaturmessungen an wolkenlosen Sommertagen mit intensiver Sonneneinstrahlung zu verbessern. Die Ergebnisse zeigen, dass mit Sensoren mit nicht belüftetem Strahlenschutzschirm vor Fassaden mit hoher Albedo (weißer Anstrich) um bis zu 2,8 °C und vor Fassaden mit niedriger Albedo (schwarzer Anstrich) um bis zu 1,9 °C höhere Lufttemperaturen gemessen werden als mit belüftetem Strahlenschutzschirm. Eine weiterführende Analyse verdeutlicht die starke Abhängigkeit des Strahlungseinflusses der nicht belüfteten Sensoren von der Windgeschwindigkeit.

Die Ergebnisse dieser Studie unterstreichen die erhebliche Auswirkung direkter Sonneneinstrahlung auf die Genauigkeit von Temperaturmessungen und betonen in diesem Zusammenhang die entscheidende Rolle der Sensorbelüftung, die durch vorherrschende Windbedingungen und in Strahlenschutzschirme eingebaute mechanische Ventilatoren beeinflusst wird. Bei Windstille können nicht belüftete Strahlenschutzschirme aufgrund der Erhitzung bei Sonneneinstrahlung Messfehler von bis zu 5 °C verursachen. Die Verwendung belüfteter Strahlenschutzschirme verringert diese Fehler; jedoch kann an heißen Sommertagen bei direkter Bestrahlung auch hier der Messfehler bis zu 3 °C erreichen. Ein Messfehler von weniger als einem Grad erscheint bei Temperaturmessung in der Sonne nur bei hohen Windgeschwindigkeiten von mehr als 4 m/s möglich zu sein.

Die beobachteten Messfehler mit nicht belüftetem Strahlenschutzschirm stimmen mit den Ergebnissen von Lin et al. [27] überein, die Temperaturfehler von 2–4 Grad an klaren, windstillen Tagen zur Mittagszeit gemessen haben. Als Referenzmessung wurde ein belüfteter Sensor des US-Klimareferenznetzes herangezogen. Nakamura und Mahrt stützten ihre Bewertungen ebenfalls auf

einen Sensor mit belüftetem Strahlenschutzschirm und stellten einen Strahlungsfehler von mehr als einem Grad Celsius in 2,6% der Messdaten fest, wobei einzelne Punkte um mehr als 2 °C abwichen [40]. Die Ungenauigkeit des belüfteten Strahlenschutzschirms wurde in den Auswertungen beider Studien vernachlässigt.

Die Bestimmung der Genauigkeit von Temperatursensoren im Vergleich zu Sensoren in mechanisch belüfteten, beschatteten, mehrschichtigen Röhren, deren Messfehler üblicherweise als vernachlässigbar ($<0,1$ °C) angenommen wird, ist ein gängiger Ansatz. In der beschriebenen Studie [31] erfüllte der Referenzsensor unter dem Prüfstand diese Kriterien. Die Genauigkeit aller Messungen in einem Abstand von 30 cm vor der Fassade wurde im Vergleich zu diesem Referenzsensor bestimmt. Sowohl nicht belüftete als auch belüftete Sensoren zeigten signifikante Messfehler, wenn die Lufttemperatur unter dem Einfluss direkter Sonneneinstrahlung gemessen wurde. Der Strahlungsfehler blieb in 95% der Fälle bei nicht belüftetem bzw. belüftetem Strahlungsschirm innerhalb von $\pm 2,4$ bzw. $\pm 1,3$ Grad vor der weißen sowie innerhalb von $\pm 2,0$ bzw. $\pm 1,5$ Grad vor der schwarzen Fassade. Dies unterstreicht die Notwendigkeit einer zusätzlichen Referenzmessung mit einem belüfteten Sensor an einem dauerhaft beschatteten Ort, wenn Temperaturen in der Sonne gemessen werden, um anschließend eine Datenkorrektur vornehmen zu können.

Die lokale Windgeschwindigkeit erwies sich ebenfalls als entscheidender Parameter für die Genauigkeit der Temperaturmessung. Laut Kurzeja [41] sind zuverlässige Temperaturmessungen erst bei einer Windgeschwindigkeit von mehr als 1 m/s möglich. Gleichfalls berichten Nakamura und Mahrt [40] von einem Messfehler zufolge Solarstrahlung von 0,6 °C bei Windgeschwindigkeiten unter 1 m/s, der sich bei höheren Windgeschwindigkeiten auf 0,3 °C verringert. Richardson et al. [42] registrierten Messfehler von bis zu 1,8 °C während windstiller Zeiträume. In beiden Studien ist die Referenz ein Temperatursensor in einem mechanisch belüfteten Strahlenschutzschirm, der selbst eine Genauigkeit von 0,3 °C und einen Strahlungsfehler von 0,2 °C bei 1000 W/m² aufweist. Im Vergleich dazu betragen in der beschriebenen Studie die Temperaturunterschiede von nicht belüfteten Sensoren im Vergleich zu belüfteten Sensoren für 95% der Fälle weniger als 0,6 bzw. 1,1 °C für schwarze bzw. weiße Fassaden. Die bedeutendsten Temperaturunterschiede (mit 95% Fraktilen von 1,1 bzw. 1,6 °C) traten bei Windgeschwindigkeiten unter 2 m/s auf, wobei die Unterschiede bei Windgeschwindigkeiten von mehr als 4 m/s innerhalb der Messgenauigkeit lagen.

Die Nähe der Sensoren zur Fassade kann ebenfalls aufgrund des Schattenwurfs durch das Gebäude die Messgenauigkeit beeinflussen. In einer Studie von Fang et al. zur Untersuchung einer neuen Methode zur Messung der mittleren Strahlungstemperatur wurden Unterschiede in den Messgenauigkeit von beschatteten und unbeschatteten Sensoren bzw. in Abhängigkeit des Sonnenstandswinkels sowie abhängig vom Material der reflektierenden Oberfläche festgestellt [43]. Zusätzlich kommt es bei

niedrigen Windgeschwindigkeiten zu einem zusätzlichen Strahlungsfehler. Je nach Fassadenausrichtung und Windrichtung können sich Sensoren in unmittelbarer Nähe zur Fassade im (Wind-) Schatten des Gebäudes befinden oder aber Sonnen-/Wind-exponiert sein, wodurch der Messfehler stark beeinflusst werden kann.

Zusammenfassend unterstreicht die dritte Publikation die entscheidende Bedeutung belüfteter Strahlenschutzschirme für die Erzielung hochwertiger Temperaturmessungen in der Sonne. Dennoch können auch belüftete Strahlenschutzschirme an nach Süden ausgerichteten Fassaden zu erheblichen Messfehlern zufolge Solarstrahlungseinfluss führen. Weiße Fassaden können diesen Fehler aufgrund zusätzlicher Reflexionen von Sonnenstrahlung noch weiter verschärfen, während schwarze Fassaden eine Erwärmung der Luftschicht vor der Fassade verursachen und somit zu zusätzlichen Messfehlern beitragen können.

Im Anschluss folgt nun die Erörterung des wissenschaftlichen Beitrags dieser Dissertation, wobei die Ergebnisse der Dissertation nochmals zusammenfassend dargestellt werden, um daraus Antworten auf die eingangs definierten Forschungsfragen abzuleiten.

5 Wissenschaftlicher Beitrag der Dissertation

5.1 Ergebnisse

Im Rahmen dieser Dissertation wurde die neuartige Software uhiSolver zur computergestützten Simulation des Mikroklimas anhand von drei Fallbeispielen validiert. Die Simulationsgebiete umfassen drei Schulgebäude in Wien, an denen im Rahmen der FFG-Forschungsprojekte GrünPlusSchule [44] und GRÜNEZukunftSCHULEN [45] Fassadenbegrünungssysteme installiert wurden. Dabei wurde die Annahme bestätigt, dass kleinflächige Fassadenbegrünungssysteme an nördlich ausgerichteten Wänden einen vernachlässigenden Einfluss auf das Mikroklima ausüben.

Im Zuge der Softwarevalidierung wurde zudem untersucht, inwiefern die Geometrieeingabe von Gebäuden und Freiraumaufbauten vereinfacht werden kann, ohne die Genauigkeit der Simulationsergebnisse maßgebend zu beeinflussen. Hierfür wurde eine akzeptable Fehlertoleranz von 5 % festgelegt, womit eine Vernachlässigung von Innenbauteilen von Gebäuden mit einem Massenanteil von weniger als 5 % (z.B. Treppenläufe) gerechtfertigt werden kann. Bei gut wärmegedämmten Neubauten tragen die Innenbauteile generell nur in geringem Maße zur Wärmespeicherung bei, weshalb diese hier für die Berechnung der Wärmekapazität des Gesamtgebäudes gänzlich vernachlässigt werden können.

Die Auswertung der ersten Mikroklimasimulationen vom Validierungsfall Diefenbachgasse hat im Vergleich zu den Vor-Ort-Messungen größere Temperaturabweichungen am späten Nachmittag ergeben, wenn die Sensoren vor der nordseitigen Fassadenbegrünung allmählich direkt von der Sonne bestrahlt wurden und sich dadurch deutlich aufgeheizt haben. Diese ungewollte Abweichung zwischen Simulation und Messung war auf die Verwendung unbelüfteter Strahlenschutzschirme zurückzuführen. Aus diesem Anlass wurde ein mechanisch belüfteter Strahlenschutzschirm entworfen, mit dem die Messungen im darauffolgenden Sommer wiederholt wurden.

Zusätzlich wurde die Performance des neu entwickelten Strahlenschutzschirms im Zuge von Vergleichsmessungen mit unbelüfteten Sensoren vor einer weiß sowie einer schwarz gestrichenen Fassade am Freiluftprüfstand des Forschungsbereichs für Ökologische Bautechnologien am Campus Science Center der TU Wien im Detail untersucht. Dabei hat sich herausgestellt, dass mit Sensoren mit unbelüftetem (sprich nicht mechanisch belüftetem) Strahlenschutzschirm vor Fassaden mit hoher Albedo (weißer Anstrich) um bis zu 2,8 °C und vor Fassaden mit niedriger Albedo (schwarzer Anstrich) um bis zu 1,9 °C höhere Lufttemperaturen gemessen werden als mit (mechanisch) belüftetem Strahlenschutzschirm. Am größten sind die Abweichungen mit unbelüftetem Strahlenschutzschirm bei Windgeschwindigkeiten unter 2 m/s, da in diesem Fall die erforderliche Kühlung des Sensors nicht mehr sichergestellt ist.

Unter direktem Solarstrahlungseinfluss weisen jedoch sowohl Sensoren mit nicht belüftetem als auch mit belüftetem Strahlenschutzschirm signifikante Messfehler verglichen mit einer Referenzmessung in strahlungsgeschützter Lage auf. Der Strahlungsfehler blieb in 95% der Fälle innerhalb von $\pm 2,4$ Grad mit nicht belüftetem sowie innerhalb von $\pm 1,5$ Grad mit belüftetem Strahlungsschirm. Es kann somit festgehalten werden, dass der Messfehler bei Verwendung von mechanisch belüfteten Strahlenschutzschirmen maßgeblich reduziert werden kann. Bei Temperaturmessungen in der Sonne ist dennoch mit nicht unwesentlichen strahlungsbedingten Messfehlern zu rechnen, weshalb in solchen Fällen einer qualitativ hochwertigen Referenzmessung in strahlungsgeschützter Lage eine große Bedeutung zukommt.

5.2 Beantwortung der Forschungsfragen

Anhand der oben präsentierten Ergebnisse dieser Dissertation können die einleitend definierten Forschungsfragen wie folgt beantwortet werden:

FORSCHUNGSFRAGE 1: HAT FASSADENBEGRÜNUNG EINEN EINFLUSS AUF DIE HYGROTHERMISCHE BEHAGLICHKEIT IM AUßenRAUM?

In den durchgeföhrten Studien konnten keine signifikanten Auswirkungen von (kleinflächiger) Fassadenbegrünung auf die hygrothermische Behaglichkeit im Außenraum festgestellt werden. Für die Beurteilung der hygrothermischen Behaglichkeit wurde in den untersuchten Validierungsfällen die „Scheinbare Temperatur“ (engl.: Apparent Temperature, Abk.: AT) nach Steadman [46] herangezogen. Dies ist ein gut dokumentierter und robuster Standard für die subjektiv empfundene Temperatur.

Die Scheinbare Temperatur im begrünten Innenhof des Validierungsfalles Kandlgasse ist vergleichbar mit jener der angrenzenden Straßen und teilweise sogar höher. Die Gründe dafür sind:

- geringere Luftströmungsgeschwindigkeiten im Innenhof (kaum Wind und daher kaum Feuchtigkeitsabtransport);
- höhere relative Luftfeuchtigkeit im Innenhof im Vergleich zu den umliegenden Straßen aufgrund der Evapotranspiration der Pflanzen, wobei der größte Anteil davon auf den Baum und die Stauden und nur ein geringer Anteil auf die Fassadenbegrünungssysteme entfallen;
- und „Zwickel“ im Innenhof, wo direkte Solarstrahlung und zusätzlich von den Wänden reflektierte Sekundärstrahlung zusammenfallen.

Der Einfluss der Evapotranspiration auf die simulierten Temperaturen ist nahezu vernachlässigbar und nimmt mit zunehmendem Abstand zur Fassadenbegrünung rasch ab.

Im Validierungsfall Diefenbachgasse beschränkt sich die Wirkung der Grünwand auf das Mikroklima ausschließlich auf die Luftsicht direkt vor der Begrünung. Die von den Pflanzen produzierte

Feuchtigkeit wird sofort durch den Wind abtransportiert. Auch die durch Evapotranspiration abgekühlte Luft wird sofort in Windrichtung entlang der Fassade abtransportiert. Die Kühlwirkung beträgt am Modelltag um 15:00 Uhr MESZ 0,3 °C in einem Abstand von 0,1 m bzw. 0,1 °C in einem Abstand von 0,5 m von der Begrünung. In einem Abstand von 1 m von der Grünwand ist kein Einfluss auf die Lufttemperatur mehr zu erkennen. Ähnlich verhält es sich im Validierungsfall Schuhmeierplatz. Hier ist am Modelltag um 15:00 Uhr MESZ kein Effekt der Grünwand innerhalb der numerischen Schwankungsbreite der CFD-Simulation nachweisbar. Dies gilt sowohl für die Lufttemperatur als auch die scheinbare (gefühlte) Temperatur. Letztere wird allerdings von der begrünten Pergola auf der Dachterrasse der Schule Schuhmeierplatz deutlich beeinflusst, wo sich am Modelltag im Schatten unter der Pergola eine Reduktion der scheinbaren Temperatur (AT) von etwa 4 °C einstellt. Der Kühlereffekt wird jedoch primär durch die Beschattung und weniger durch die Evapotranspiration der Pflanzen hervorgerufen.

Tabelle 5. Mikroklimatische Auswirkungen kleinflächiger Begrünungssysteme an einem heißen Sommertag in Wien.

	Lufttemperatur	Luftfeuchtigkeit	Beschattung	AT ¹
Fassadenbegrünung	Nein	Ja	Ja	Nein
Begrünte Pergola	Nein	Ja	Ja	Ja

¹ Scheinbare Temperatur nach Steadman [46].

Tabelle 5 fasst zusammen, inwiefern die Parameter Lufttemperatur, Luftfeuchtigkeit, Beschattung und scheinbare Temperatur durch kleinflächige Fassadenbegrünungssysteme bzw. schattenspendende Begrünungskonstruktionen wie begrünte Pergolen oder ähnliche Systeme beeinflusst werden. Demzufolge haben kleinflächige Begrünungssysteme keinen signifikanten Einfluss auf die Lufttemperatur, einen – wenn auch geringen – positiven Einfluss auf die Luftfeuchtigkeit und in der Regel einen deutlichen Einfluss auf die Beschattung – entweder der dahinter befindlichen Wand (Fassadenbegrünung) oder der Fläche darunter (Pergola). Hinsichtlich der scheinbaren Temperatur nach Steadman ist ausschließlich bei Systemen wie der begrünten Pergola ein Einfluss feststellbar, welcher sich auf den Bereich unter der Pergola beschränkt.

FORSCHUNGSFRAGE 2: KÖNNEN MIKROKLIMASIMULATIONEN DIESEN EINFLUSS MIT AUSREICHENDER GENAUIGKEIT BESTIMMEN UND WELCHE GENAUIGKEIT KANN IN DIESEM ZUSAMMENHANG ALS AUSREICHEND ANGESEHEN WERDEN?

Grundsätzlich eignen sich Mikroklimasimulationen gut für Variantenvergleiche. Es kann zum Beispiel „per Knopfdruck“ die Evapotranspiration der Begrünung ausgeschalten werden, um deren Einfluss auf die Lufttemperatur zu prüfen. Der Einfluss auf die Windströmung sowie auf Strahlungsreflexionen bleibt jedoch erhalten, sofern nicht in einer separaten Simulation das Begrünungssystem als Ganzes aus dem Modell entfernt wird.

In Bezug auf die Simulationsgenauigkeit weist der instationäre Validierungsfall Kandlgasse eine hohe Korrelation zu den Messdaten auf. Innerhalb eines Zeitraums von 24-Stunden beträgt die Standardabweichung der Temperaturunterschiede (simuliert zu gemessen) 0,99 °C. Der räumlich verteilte Validierungsfall Gablenzgasse zeigt ebenfalls geringe Abweichungen der simulierten Temperaturen im Vergleich zu den gemessenen Temperaturen. Die Standardabweichung der Temperaturunterschiede (simuliert zu gemessen) beträgt hier 0,93 °C und der mittlere absolute Fehler nur -0,53 °C zwischen 15:00 und 16:10 Uhr MESZ. Im Validierungsfall Diefenbachgasse ist eine zunehmende Abweichung zwischen gemessenen und simulierten Werten in den Nachmittagsstunden zu beobachten, welche auf den Einfluss direkter Solarstrahlung und die Verwendung unbelüfteter Strahlenschutzschirme zurückgeführt werden kann. Dadurch liegt hier der durchschnittliche absolute Fehler bei -2,78 °C und die Standardabweichung der absoluten Fehler bei 1,12 °C um 15:00 Uhr MESZ. Mit einer Standardabweichung von nur 0,74 °C weist der Validierungsfall Schuhmeierplatz die beste Korrelation mit den Messwerten auf. Der mittlere absolute Fehler beträgt -0,78 °C um 15:00 Uhr MESZ. Eine Übersicht über die gesammelten Simulationsergebnisse wird in Tabelle 6 geboten.

Tabelle 6. Mittlere absolute Fehler und 24h-Standardabweichungen der absoluten Fehler der Windgeschwindigkeit (U), Temperatur (T) und Luftfeuchtebeladung (X) zwischen den uhiSolver-Simulationsergebnissen und den Vor-Ort-Messungen für die untersuchten Validierungsfälle.

Validierungsfälle:	Kandlgasse	Gablenzgasse	Diefenbachgasse	Schuhmeierplatz
Mittlere absolute Fehler:				
U [m/s]	-	-0,18	-1,0	-3,7
T [°C]	-2,43	-0,53	-2,78	-0,78
X [kg/kg]	-	0,143	0,0025	0,0001
Standardabweichungen der absoluten Fehler:				
U [m/s]	-	0,50	-	-
T [°C]	0,99	0,93	1,12	0,74
X [kg/kg]	-	0,302	0,0014	0,0005

uhiSolver zeigt eine relativ hohe räumliche und zeitliche Genauigkeit für Temperaturvorhersagen. Die absolute Genauigkeit (definiert über die Standardabweichung) liegt in den präsentierten Validierungsfällen im Allgemeinen innerhalb von 1,00 °C, wobei nur im Validierungsfall Diefenbachgasse eine geringfügig höhere Abweichung aufgetreten ist. Die relative thermische Genauigkeit liegt im Bereich von 10 % für heiße, wolkenlose Tage im Vergleich zu einer täglichen thermischen Variation von 10 °C. Eine Genauigkeit von 10 % wird für Berechnungen in der Entwurfsphase häufig als ausreichend angesehen.

Die maximale gemessene Kühlwirkung der Fassadenbegrünung im Validierungsfall Diefenbachgasse von 0,3 °C ist deutlich geringer als die Standardabweichung bzw. der mittlere absolute Fehler zwischen Simulation und Messung. Die Genauigkeit der Simulation ist in dieser Hinsicht nicht ausreichend, um den Einfluss der Fassadenbegrünung zweifelsfrei zu bestimmen – oder anders ausgedrückt: Der

Einfluss der Fassadenbegrünung ist in Relation zur Simulationsgenauigkeit nicht signifikant. Es stellt sich jedoch die Frage, ob eine Anpassung der Simulationsparameter zur Erreichung einer besseren Übereinstimmung mit den Messwerten in einem spezifischen Validierungsfall Sinn macht. In diesem Zusammenhang ist es notwendig, auch die Genauigkeit der Messdaten in die Betrachtung einzubeziehen, da es wenig Sinn macht, die Simulation unreflektiert an „falsche“ Messwerte anzupassen. Da für die Beurteilung der (maximalen) Kühlwirkung von Begrünungssystemen möglichst wolkenlose, sonnige Sommertage herangezogen werden, ist ein gewisser Strahlungseinfluss auf die Messwerte nicht auszuschließen – wie in Abschnitt 5.1 erörtert, kann dieser selbst bei Verwendung mechanisch belüfteter Strahlenschutzschirme bis zu 1,5 °C ausmachen. In Anbetracht dieser zu erwartenden Messgenauigkeit erscheint es wenig zweckmäßig, weiter an der Genauigkeit der Simulationsergebnisse zu schrauben. Vielmehr sollte Augenmerk auf qualitativ hochwertige Messtechnik und eine sinnvolle Positionierung der Sensoren gelegt werden, worauf in den nachfolgenden Ausführungen näher eingegangen wird.

FORSCHUNGSFRAGE 3: WAS IST BEI DER TEMPERATURMESSUNG VOR FASSADEN ZU BEACHTEN, DAMIT DIESE MESSDATEN ZUR VALIDIERUNG VON SIMULATIONSERGEBNISSEN HERANGEZOGEN WERDEN KÖNNEN?

Bei der Validierung von Mikroklimasimulationen ist es wichtig, die Simulationsergebnisse mit geeigneten Messdaten zu vergleichen. Wenn zum Beispiel die simulierte Lufttemperatur an einem bestimmten Ort durch Messdaten validiert werden soll, muss sich genau an dieser Stelle ein Sensor zu Lufttemperaturmessung befinden. Dabei verfälscht jedoch jeglicher Strahlungseinfluss das Ergebnis des Vergleiches, da dieser in den Simulationsergebnissen von der Lufttemperatur losgelöst ausgegeben wird. Aus diesem Grund sollte für die Validierung eine Messposition gewählt werden, bei der mit keinem nennenswerten Strahlungseinfluss zu rechnen ist, damit ein sauberer Vergleich möglich ist. Messpositionen, die zum Zeitpunkt, der für die Software-Validierung gewählt wird, direkt von der Sonne beschienen werden, sind daher nicht geeignet.

Zusätzlich ist bei allen Lufttemperaturmessungen ein mechanisch belüfteter Strahlenschutzschirm zu verwenden, um jeglichen restlichen Strahlungseinfluss auszuschließen. Bei Temperaturmessungen in der Sonne verursacht die Verwendung von unbelüfteten Strahlenschutzschirmen einen zusätzlichen Messfehler von im Mittel 0,9 °C und im Extremfall sogar bis zu 2,8 °C. Bei Messungen im Schatten ist mit einer geringeren Abweichung zwischen belüfteten und unbelüfteten Strahlenschutzschirmen zu rechnen, wobei dieser Fall in der vorliegenden Dissertation nicht untersucht wurde. Gemäß Kurzeja ist dies jedoch ein gängiger Ansatz, um die Genauigkeit von Temperatursensoren zu evaluieren [41]. Die Empfehlung des Autors ist es, die Verwendung solcher mechanisch belüfteten, beschatteten,

mehrwandigen Strahlenschutzschirme als Standard für die Validierung von Mikroklimasimulationssoftware vorzuschreiben.

Ein weiterer Faktor, der für die Verwendung von mechanisch belüfteten Strahlenschutzschirmen spricht, ist deren geringere Abhängigkeit von den lokalen Windverhältnissen. Während unbelüftete Strahlenschutzschirme bei geringen Windgeschwindigkeiten von unter 2 m/s signifikante Messfehler aufweisen und erst bei höheren lokalen Windgeschwindigkeiten zuverlässige Ergebnisse liefern, ist die Performance von mechanisch belüfteten Strahlenschutzschirmen unabhängig von der Windgeschwindigkeit und Windrichtung weitestgehend konstant und es ist keine Korrektur der Messdaten für einen Vergleich mit den Simulationsergebnissen erforderlich.

Sofern die Temperaturmessung vor einer Fassade bzw. Fassadenbegrünung erfolgt, sollte auf eine möglichst geringe Albedo der dahinterliegenden Fassade bzw. Fassadenbegrünung (inkl. Substrat) geachtet werden, da es bei hellen Fassaden zu mitunter signifikanten Reflexionen kommen kann, die einen zusätzlichen Messfehler von bis zu 0,9 °C ausmachen können.

Zusammenfassend werden folgende Parameter als wesentlich für eine exakte Temperaturmessung vor Fassaden bzw. Fassadenbegrünungen zur Validierung von Mikroklimasimulationen festgestellt:

- Messposition im Schatten bzw. ohne direkten Strahlungseinfluss;
- Verwendung eines mechanisch belüfteten, mehrschaligen Strahlenschutzschirms;
- Möglichst geringe Albedo der Fassade.

Da die Albedo von Fassadenbegrünung in der Regel nicht so hoch ist, dass sie signifikante Reflexionen verursacht, ist der letzte Punkt hier nicht relevant. Die beiden wesentlichen Parameter sind in diesem Fall somit die Messposition und die Art der Belüftung der verwendeten Strahlenschutzschirme. Während die Verwendung geeigneter, mechanisch belüfteter Strahlenschutzschirme leicht umzusetzen ist, kann sich insbesondere an nach Osten, Süden und Westen ausgerichteten Fassaden das Kriterium einer Messposition im Schatten als Herausforderung erweisen. Der Autor schlägt in solchen Fällen in Anlehnung an den von Liu et al. [47] entworfenen natürlich belüfteten Strahlenschutzschirm eine örtliche Überdachung der Sensoren inkl. der belüfteten Strahlenschutzschirme vor, um einen direkten Strahlungseinfluss auszuschließen.

6 Fazit und Ausblick

Die vorliegende Dissertation hat einen Beitrag zur Bewertung des Einflusses von Fassadenbegrünung auf das Mikroklima geleistet und gleichzeitig wichtige Erkenntnisse zur Verbesserung der Genauigkeit von Mikroklimasimulationen und zur Validierung dieser Simulationen durch Messungen geliefert. Die wichtigsten Ergebnisse und Erkenntnisse lassen sich wie folgt zusammenfassen:

- Die durchgeführten Studien haben gezeigt, dass kleinflächige Fassadenbegrünungssysteme, insbesondere an nördlich ausgerichteten Wänden, nur einen vernachlässigbaren Einfluss auf das Mikroklima haben. Die hygrothermische Behaglichkeit im Außenraum wird durch diese Systeme nicht signifikant verändert.
- Die entwickelte Software uhiSolver ermöglicht eine zuverlässige Simulation des Mikroklimas. Die Genauigkeit der Simulationsergebnisse wurde anhand von Validierungsfällen nachgewiesen, wobei eine hohe Übereinstimmung mit den gemessenen Daten erzielt wurde. Die räumliche und zeitliche Genauigkeit der Temperaturvorhersagen liegt innerhalb üblicher Grenzen für vergleichbare Simulationsprogramme.
- Bei der Validierung von Mikroklimasimulationen ist es entscheidend, geeignete Messdaten zu verwenden und die Messposition sowie die Art des Strahlenschutzes sorgfältig zu wählen. Mechanisch belüftete Strahlenschutzschirme haben sich als besonders effektiv erwiesen, um strahlungsbedingte Messfehler zu minimieren.

Für zukünftige Forschungsvorhaben im Bereich der Mikroklimamodellierung und Fassadenbegrünung bieten sich verschiedene Perspektiven an. Eine Weiterentwicklung der Simulationssoftware zur Berücksichtigung zusätzlicher Einflussfaktoren wie beispielsweise unterschiedlicher Begrünungstypen könnte die Genauigkeit der Vorhersagen weiter verbessern. Darüber hinaus könnten Langzeitstudien durchgeführt werden, um den langfristigen Einfluss von Fassadenbegrünung auf das lokale Mikroklima zu untersuchen.

Die vorliegende Arbeit liefert somit nicht nur Erkenntnisse für die wissenschaftliche Gemeinschaft, sondern auch wertvolle Informationen für Stadtplaner, Architekten und andere Fachleute, die sich mit der Gestaltung und Bewertung urbaner Räume befassen. Durch die Integration von Fassadenbegrünung in städtische Planungsprozesse kann nicht nur das Stadtklima verbessert, sondern auch das Wohlbefinden und die Lebensqualität der Bewohnerinnen und Bewohner nachhaltig gesteigert werden.

7 Literatur

- [1] Statista Research Department, „Klimawandel: Entstehung und Folgen“. Zugegriffen: 15. März 2024. [Online]. Verfügbar unter:
<https://de.statista.com/themen/689/klimawandel/#editorsPicks>
- [2] L. Yang, F. Qian, D. X. Song, und K. J. Zheng, „Research on Urban Heat-Island Effect“, in *Procedia Engineering*, Elsevier Ltd, 2016, S. 11–18. doi: 10.1016/j.proeng.2016.10.002.
- [3] C. Brandenburg, D. Damyanovic, F. Reinwald, B. Allex, B. Gantner, und C. Czachs, „Urban Heat Islands - Strategieplan Wien“, Wien, 2015.
- [4] D. Damyanovic *u. a.*, „Pilot action city of Vienna - UHI-STRAT Vienna“, in *Counteracting Urban Heat Island Effects in a Global Climate Change Scenario*, Springer International Publishing, 2016, S. 257–280. doi: 10.1007/978-3-319-10425-6_9.
- [5] M. H. Zawawi *u. a.*, „A review: Fundamentals of computational fluid dynamics (CFD)“, 2018, S. 020252. doi: 10.1063/1.5066893.
- [6] G. M. Stavrakakis, D. Al Katsaprakakis, und M. Damasiotis, „Basic principles, most common computational tools, and capabilities for building energy and urban microclimate simulations“, *Energies (Basel)*, Bd. 14, Nr. 20, Okt. 2021, doi: 10.3390/en14206707.
- [7] „ENVI-met Model Architecture“. Zugegriffen: 23. September 2020. [Online]. Verfügbar unter:
<http://envi-met.info/>
- [8] S. Huttner und M. Bruse, „Numerical modeling of the urban climate - a preview on ENVI-MET 4.0“, *The seventh International Conference on Urban Climate*, Nr. July, S. 4, 2009.
- [9] L. Deng, X. Jia, W. Wang, und S. A. Hussain, „Revealing Impacts of Trees on Modeling Microclimate Behavior in Spaces between Buildings through Simulation Monitoring“, *Buildings*, Bd. 12, Nr. 8, Aug. 2022, doi: 10.3390/buildings12081168.
- [10] R. Li *u. a.*, „CFD simulations of the tree effect on the outdoor microclimate by coupling the canopy energy balance model“, *Build Environ*, Bd. 230, Feb. 2023, doi: 10.1016/j.buildenv.2023.109995.
- [11] H. Xu, C. C. Wang, X. Shen, und S. Zlatanova, „3d tree reconstruction in support of urban microclimate simulation: A comprehensive literature review“, *Buildings*, Bd. 11, Nr. 9, Sep. 2021, doi: 10.3390/buildings11090417.

- [12] H. Xu, C. C. Wang, X. Shen, und S. Zlatanova, „EVALUATING THE PERFORMANCE OF HIGH LEVEL-OF-DETAIL TREE MODELS IN MICROCLIMATE SIMULATION“, in *ISPRS Annals of the Photogrammetry, Remote Sensing and Spatial Information Sciences*, Copernicus Publications, Okt. 2022, S. 277–284. doi: 10.5194/isprs-annals-X-4-W3-2022-277-2022.
- [13] R. Segura *u. a.*, „How do street trees affect urban temperatures and radiation exchange? Observations and numerical evaluation in a highly compact city“, *Urban Clim*, Bd. 46, Dez. 2022, doi: 10.1016/j.ulim.2022.101288.
- [14] L. L. H. Peng und C. Y. Jim, „Green-roof effects on neighborhood microclimate and human thermal sensation“, *Energies (Basel)*, Bd. 6, Nr. 2, S. 598–618, 2013, doi: 10.3390/en6020598.
- [15] U. Berardi, „The outdoor microclimate benefits and energy saving resulting from green roofs retrofits“, *Energy Build*, Bd. 121, S. 217–229, 2016, doi: 10.1016/j.enbuild.2016.03.021.
- [16] L. Fachinello Krebs und E. Johansson, „Influence of microclimate on the effect of green roofs in Southern Brazil – A study coupling outdoor and indoor thermal simulations“, *Energy Build*, Bd. 241, Juni 2021, doi: 10.1016/j.enbuild.2021.110963.
- [17] J. Geletič *u. a.*, „High-fidelity simulation of the effects of street trees, green roofs and green walls on the distribution of thermal exposure in Prague-Dejvice“, *Build Environ*, Bd. 223, Sep. 2022, doi: 10.1016/j.buildenv.2022.109484.
- [18] B. Maronga *u. a.*, „The Parallelized Large-Eddy Simulation Model (PALM) version 4.0 for Atmospheric and Oceanic Flows: Model Formulation, Recent Developments, and Future Perspectives The Parallelized Large-Eddy Simulation Model“, *Geosci. Model Dev. Discuss*, Bd. 8, S. 1539–1637, 2015, doi: 10.5194/gmdd-8-1539-2015.
- [19] P. Krč, J. Resler, M. Sühring, S. Schubert, M. H. Salim, und V. Fuka, „Radiative Transfer Model 3.0 integrated into the PALM model system 6.0“, *Geosci Model Dev*, Bd. 14, Nr. 5, S. 3095–3120, Mai 2021, doi: 10.5194/gmd-14-3095-2021.
- [20] J. B. Stewart, „Modelling surface conductance of pine forest“, *Agric For Meteorol*, Bd. 43, Nr. 1, S. 19–35, Juni 1988, doi: 10.1016/0168-1923(88)90003-2.
- [21] Z. Liu *u. a.*, „Modeling microclimatic effects of trees and green roofs/façades in ENVI-met: Sensitivity tests and proposed model library“, *Build Environ*, Bd. 244, Okt. 2023, doi: 10.1016/j.buildenv.2023.110759.

- [22] N. Antoniou, H. Montazeri, M. Neophytou, und B. Blocken, „CFD simulation of urban microclimate: Validation using high-resolution field measurements“, *Science of the Total Environment*, Bd. 695, Dez. 2019, doi: 10.1016/j.scitotenv.2019.133743.
- [23] S. P. Venkateshan, „Systematic Errors in Temperature Measurement“, in *Mechanical Measurements*, Springer International Publishing, 2022, S. 197–220. doi: 10.1007/978-3-030-73620-0_5.
- [24] M. Avraham, H. Yadid, T. Blank, und Y. Nemirovsky, „Air Temperature Measurement Using CMOS-SOI-MEMS Sensor Dubbed Digital TMOS +“, *Engineering Proceedings*, Bd. 27, Nr. 1, 2022, doi: 10.3390/ecsa-9-13224.
- [25] E. Erell, V. Vić, V. Leal, und E. Maldonado, „MEASUREMENT OF AIR TEMPERATURE IN THE PRESENCE OF A LARGE RADIANT FLUX: AN ASSESSMENT OF PASSIVELY VENTILATED THERMOMETER SCREENS“, 2005.
- [26] G. Lopardo, F. Bertiglia, S. Curci, G. Roggero, und A. Merlone, „Comparative analysis of the influence of solar radiation screen ageing on temperature measurements by means of weather stations“, *International Journal of Climatology*, Bd. 34, Nr. 4, S. 1297–1310, März 2014, doi: 10.1002/joc.3765.
- [27] X. Lin, K. G. Hubbard, und C. B. Baker, „Surface air temperature records biased by snow-covered surface“, *International Journal of Climatology*, Bd. 25, Nr. 9, S. 1223–1236, Juli 2005, doi: 10.1002/joc.1184.
- [28] C. M. Baumgartner, „Influence of different construction methods and soil types on the Urban Heat Island-Effect“, master thesis, Vienna University of Technology, 2019.
- [29] F. Teichmann, C. M. Baumgartner, A. Horvath, M. Luisser, und A. Korjenic, „Simulation of urban microclimate with uhiSolver: software validation using simplified material data“, *EcoI Process*, Bd. 10, Nr. 1, 2021, doi: 10.1186/s13717-021-00336-y.
- [30] F. Teichmann, A. Horvath, M. Luisser, und A. Korjenic, „The Impact of Small-Scale Greening on the Local Microclimate — A Case Study at Two School Buildings in Vienna“, *Sustainability (Switzerland)*, Bd. 14, Nr. 20, Okt. 2022, doi: 10.3390/su142013089.
- [31] F. Teichmann, A. Pichlhöfer, A. Sulejmanovski, und A. Korjenic, „Measurement Errors When Measuring Temperature in the Sun“, *Sensors*, Bd. 24, Nr. 5, März 2024, doi: 10.3390/s24051564.

- [32] D. Maiullari, M. Mosteiro-Romero, und M. Pijpers-Van Esch, „Urban microclimate and energy performance: An integrated simulation method“, *PLEA 2018 - Smart and Healthy within the Two-Degree Limit: Proceedings of the 34th International Conference on Passive and Low Energy Architecture*, Bd. 1, S. 384–389, 2018.
- [33] J. Natanian, D. Maiullari, A. Yezioro, und T. Auer, „Synergetic urban microclimate and energy simulation parametric workflow“, *J Phys Conf Ser*, Bd. 1343, Nr. 1, 2019, doi: 10.1088/1742-6596/1343/1/012006.
- [34] E. Diz-mellado, S. Rubino, S. Fern, und G. Macarena, „Applied Machine Learning Algorithms for Courtyards Thermal Patterns Accurate Prediction“, *mathematics*, Bd. 9, Nr. 1142, S. 1–19, 2021, [Online]. Verfügbar unter: <https://doi.org/10.3390/math9101142>
- [35] A. B. Daemei, E. Shafiee, A. A. Chitgar, und S. Asadi, „Investigating the thermal performance of green wall: Experimental analysis, deep learning model, and simulation studies in a humid climate“, *Build Environ*, Bd. 205, S. 108201, 2021, doi: 10.1016/j.buildenv.2021.108201.
- [36] R. U. Galagoda, G. Y. Jayasinghe, R. U. Halwatura, und H. T. Rupasinghe, „The impact of urban green infrastructure as a sustainable approach towards tropical micro-climatic changes and human thermal comfort“, *Urban For Urban Green*, Bd. 34, S. 1–9, Aug. 2018, doi: 10.1016/j.ufug.2018.05.008.
- [37] C. Gromke, B. Blocken, W. Janssen, B. Merema, T. van Hooff, und H. Timmermans, „CFD analysis of transpirational cooling by vegetation: Case study for specific meteorological conditions during a heat wave in Arnhem, Netherlands“, *Build Environ*, Bd. 83, S. 11–26, 2015, doi: 10.1016/j.buildenv.2014.04.022.
- [38] L. L. H. Peng, Z. Jiang, X. Yang, Y. He, T. Xu, und S. S. Chen, „Cooling effects of block-scale facade greening and their relationship with urban form“, *Build Environ*, Bd. 169, Feb. 2020, doi: 10.1016/j.buildenv.2019.106552.
- [39] J. Fahed, E. Kinab, S. Ginestet, und L. Adolphe, „Impact of urban heat island mitigation measures on microclimate and pedestrian comfort in a dense urban district of Lebanon“, *Sustain Cities Soc*, Bd. 61, S. 102375, 2020, doi: 10.1016/j.scs.2020.102375.
- [40] R. Nakamura und L. Mahrt, „Air Temperature Measurement Errors in Naturally Ventilated Radiation Shields“, 2005.
- [41] R. Kurzeja, „Accurate temperature measurements in a naturally-aspirated radiation shield“, *Boundary Layer Meteorol*, Bd. 134, Nr. 1, S. 181–193, Jän. 2010, doi: 10.1007/s10546-009-9430-2.

- [42] S. J. Richardson, F. V Brock, S. R. Semmer, und C. Jirak, „Minimizing Errors Associated with Multiplate Radiation Shields“, *J Atmos Ocean Technol*, Bd. 16, Nr. 11, S. 1862–1872, Nov. 1999, doi: [https://doi.org/10.1175/1520-0426\(1999\)016<1862:MEAWMR>2.0.CO;2](https://doi.org/10.1175/1520-0426(1999)016<1862:MEAWMR>2.0.CO;2).
- [43] Z. Fang, H. He, Y. Mao, X. Feng, Z. Zheng, und Z. Guo, „Investigating an accurate method for measuring the outdoor mean radiation temperature“, *International Journal of Thermal Sciences*, Bd. 188, Juni 2023, doi: 10.1016/j.ijthermalsci.2023.108219.
- [44] A. Korjenic *u. a.*, „GrünPlusSchule@Ballungszentrum Hocheffiziente Fassaden- und Dachbegrünung mit Photovoltaik Kombination; optimale Lösung für die Energieeffizienz in gesamtökologischer Betrachtung“, Endbericht, Stadt der Zukunft, FFG/BMVIT, Wien, 2018.
- [45] A. Korjenic, R. Dopheide, B. Knoll, und U. Pitha, „GRÜNEzukunftSCHULEN - Grüne Schuloasen im Neubau. Fokus Planungsprozess und Bestandsgebäude: Endbericht“. Wien.
- [46] R. G. Steadman, „Norms of apparent temperature in Australia“, *Aust. Met. Mag.* 43, S. 1–16, 1994.
- [47] Q. Liu, W. Jin, J. Yang, H. Zhu, und W. Dai, „Design and Experiments of a Naturally-Ventilated Radiation Shield for Ground Temperature Measurement“, *Atmosphere (Basel)*, Bd. 14, Nr. 3, S. 523, März 2023, doi: 10.3390/atmos14030523.

8 Anhang

8.1 Erste Publikation

Status	Veröffentlicht am 29. Oktober 2021
Original Titel (Englisch)	Simulation of urban microclimate with uhiSolver: software validation using simplified material data
Titel (Deutsch)	Simulation des städtischen Mikroklimas mit uhiSolver: Validierung der Software anhand vereinfachter Materialdaten
Autor:innen	Florian Teichmann, Christine Maria Baumgartner, Andras Horvath, Markus Luisser, Azra Korjenic
ISBN/ISSN	ISSN: 2192-1709 (electronic) DOI: 10.1186/s13717-021-00336-y
Sprache	Englisch
Schlagwörter	Urban heat island effect, Urban microclimate, CFD simulation, Microclimate simulation, Apparent temperature
Quelle	<i>Ecological Processes</i> , Vol. 10, Artikel 67 (2021), Collection: Sustainable Urban Systems, SpringerOpen [Peer Reviewed Journal]

RESEARCH

Open Access



Simulation of urban microclimate with uhiSolver: software validation using simplified material data

Florian Teichmann^{1*} Christina Maria Baumgartner¹, Andras Horvath², Markus Luisser² and Azra Korjenic¹

Abstract

Background: Increasing urbanization as well as global warming requires an investigation of the influence of different construction methods and ground surfaces on the urban heat island effect (UHI effect). The extent of the influence of the urban structure, the building materials used and their surfaces on the UHI effect can be significantly reduced already in the planning phase using a designated OpenFOAM-based solver “uhiSolver”.

Results: In the first part of this research work, it is shown that inner building details and components can be neglected while still obtaining sufficiently accurate results. For this purpose, the building model was divided into two layers: a surface layer without mass, where the interaction with radiation takes place, and a component layer, which contains all relevant components and cavities of the building represented with mass-averaged material properties. It has become apparent that the three parameters—albedo, heat capacity and thermal resistance—which have a decisive influence on the interaction, have different effects on the component temperatures and the surface temperatures. In the second part of this research work, dynamic 3D computational fluid dynamics (CFD) simulations are performed with uhiSolver for a residential block in Vienna. Comparing the simulation results with measurement data collected on site, it is shown that the simplified assumption of homogeneous material data for building bodies provides very good results for the validation case investigated. However, the influence of the greening measures in the courtyard of the residential block on the air temperature is found to be negligible. Furthermore, it was observed that due to locally higher radiation density, lower air velocities and higher air humidity, the apparent temperature in the courtyard is sometimes perceived to be higher than in the adjacent streets, despite the lower air temperature.

Conclusions: Simplifying the modeling process of the uhiSolver software by reducing the model complexity helps to reduce manual work for setting up appropriate boundary conditions of buildings. Compared to market competitors, good results are obtained for the validation case Kandlgasse presented in this research work, despite the simplifications proposed. Thus, uhiSolver can be used as a robust analytical tool for urban planning.

Keywords: Urban heat island effect, Urban microclimate, CFD simulation, Microclimate simulation, Apparent temperature

Introduction

Background

Over the past 40 years, the temperature in Austria has risen significantly during the summer months. The

seasonal increase in temperature during this period is about 2 °C (Zentralanstalt für Meteorologie und Geodynamik 2002). Especially in cities, the issue of heat stress is becoming increasingly important. The decisive factor for the heat stress is the lower night-time cooling of urban areas compared to the rural environment. During the day, the difference in temperature between the city and the surrounding area is generally up to 1 °C, whereas at

*Correspondence: florian.teichmann@tuwien.ac.at

¹ Vienna University of Technology, Vienna, Austria

Full list of author information is available at the end of the article

night it can exceed 5 °C (Schmid and Pröll 2020). During a heat wave in August 2015, a night-time air temperature of up to 25 °C was measured in the city center of Vienna, which is about seven degrees above the average night-time air temperature of the years 1971–2000 (Zentralanstalt für Meteorologie und Geodynamik 2002). At such high night-time temperatures, living spaces can no longer be cooled down sufficiently by natural ventilation and the human organism is unable to recover from the heat stress during the day (Schmid and Pröll 2020).

Urban heat islands are of great global importance because today more people live in urban than in rural areas already. This number will continue to rise—according to predictions, two-thirds of the world population will live in cities by 2050 (United Nations Department of Economic and Social Affairs 2018). Climatically driven urban planning is essential to keep overheating of cities to a minimum (Schmid and Pröll 2020). The urban heat island effect can be reduced not only by careful planning of the urban structure, but also by a well-considered use of building materials and surfaces. Greening measures on the building scale (e.g., green walls and roofs) can have a decisive effect in terms of urban heat mitigation, which was shown in several research studies already (Mursch-Radlgruber et al. 2009; Technische Universität Wien and Universität für Bodenkultur Wien 2018; Korjenic et al. 2018, 2020; Hollands et al. 2018; Mitterböck and Korjenic 2017). In most construction projects, however, the effects on the microclimate are not yet taken into account, since often both the planners and the construction companies lack an understanding of this topic. Numerical simulation models using computational fluid dynamics (CFD) simulations can help to understand the complex interactions between the building structure and the microclimate and thus create the basis for mitigating urban heat island effects (Toparlar et al. 2015).

To avoid thermal stress caused by urban heat islands, it is important to take into account all relevant factors in the assessment of thermal comfort. The four environmental factors are air temperature, humidity, air flow and radiation. The personal factors are the clothing and the level of physical activity (B. of M. Commonwealth of Australia 2010). There are many methods of combining these factors into a single number to assess the outdoor thermal environment—for example, the Wet Bulb Globe Temperature (WBGT) (B. of M. Commonwealth of Australia 2010), the Universal Thermal Climate Index (UTCI) (Jendritzky et al. 2001), the Physiologically Equivalent Temperature (PET) (Honjo 2009) as well as the Apparent Temperature (AT) (Steadman 1994). Another way to assess thermal comfort is to calculate the thermal comfort indices Predicted Mean Vote (PMV) and Predicted Percentage of Dissatisfied (PPD), using the Fanger's

method proposed in ISO Standard 7730 (Gameiro da Silva 2013), or the Human Thermal Model (HTM) which can be used for predicting thermal behavior of the human body under both steady-state and transient indoor environment conditions (Holopainen 2012).

Within the validation case investigated in this study the apparent temperature is used for the assessment of thermal comfort, being a well-documented and relatively robust standard for subjective, felt temperature. It is determined by the simulation program uhiSolver, which is described in detail in the following section.

Numerical models in microclimate modeling

There are several numerical models in microclimate modeling at different spatial scales available nowadays, ranging from the meteorological mesoscale (<200 km) over the meteorological microscale (<2 km) to the building scale (<100 m) and the indoor environment (<10 m) (Toparlar et al. 2017). Some exemplary numerical models at the meteorological microscale are ENVI-met, Ladybug, Urban Weather Generator (UWG) and ANSYS (ENVI_MET Decoding urban nature. <https://www.envi-met.com/de/>; Ladybug. <https://www.ladybug.tools/ladybug.html>; Urban Weather Generator 4.1 urban heat island effect modeling software. <http://urbanmicroclimate.scripts.mit.edu/uwg.php>; Ansys. <https://www.ansys.com/>). In Austria, the application of the Greenpass Editor is widely used, which is based on a microclimate simulation with the ENVI-met software (GREENPASS Software <http://envi-met.info/>). The three-dimensional microclimate simulation model ENVI-met is used in the fields of climatology, urban planning, architecture and construction. It is designed for microscale simulations with a horizontal resolution from 0.5 m to 10 m and a time frame of 24–48 h with a time step of 1–5 s. This resolution allows to analyze small-scale interactions between individual buildings, surfaces and plants (ENVI-met Model Architecture 2019). The physical properties of the wall or façade that are considered in the model are reflectivity, absorption, transmittance, emissivity, thermal conductivity, specific heat storage capacity and the thickness of the wall. Heat flows parallel to the surface of the building component are not taken into account (Huttner and Bruse 2009). In the latest release of ENVI-met up to 3 different materials can be assigned to a wall structure (ENVI-met Model Architecture 2019; Terjung and O'Rourke 1980).

The calculation method allows a rough estimate of the energy balance and thus the temperature within individual buildings. For this calculation, the buildings are considered as empty air volumes. Neither the heat storage capacity of elements in the building nor the internal heat flows are taken into account. In order to enable the

comparability of the simulation results with measured data, the daily variations of the atmospheric boundary conditions (main wind flow, temperature, humidity and air turbulence) as well as the incoming radiation can be defined (Huttner and Bruse 2009).

Another microclimate simulation program currently under development is the so-called uhiSolver from Rheologic GmbH in Vienna. As part of the “UHI Black Box” research project funded by the FFG (Austrian Research Promotion Agency), the technical feasibility of a “black box model” was tested between May 2019 and April 2020 in order to implement different building types and ground surfaces in the uhiSolver software. The manual effort of model creation was to be minimized by reducing the parameter diversity without significantly influencing the accuracy of the simulation with regard to the results for the assessment of the urban microclimate.

uhiSolver is a microclimate simulation program based on the OpenFOAM library. It combines compressible fluid flow (of air), buoyancy effects due to air density, heat conduction in solids (within buildings and ground), radiation and sun’s movement across the sky, shadows from buildings and vegetation, air flow modulation through zones of vegetation and evapotranspiration in one program. In the same way as ENVI-met and ANSYS, uhiSolver uses a fully coupled approach, i.e., the building volume interacts with radiative heat transfer (incoming and outgoing), thermal conduction (incoming and outgoing) and advective heat transfer with the surrounding airflow.

Compared to market competitors (like ENVI-met, ANSYS, etc.) uhiSolver has a few advantages:

- solid code base with long history and an open/international review process and regular core code updates;
- higher accuracy of fluid flow close to buildings, ground and any architectural details compared to voxelized simulation methods due to finite volume method and arbitrarily shaped polyhedral finite volume cells;
- support for general building shapes and modern architecture like 3D curved walls and roofs, thoroughfares;
- building details smaller than 0.5 m can be included, with spatial precision in the range of centimeters;
- validated evaporation modeling (FFG IS5k, Final report, Nr. 849231, project ‘vmSol’, Rheologic GmbH and TU Vienna, 20.10.2015, internal communication) (evaporation from wet surfaces and condensation on smooth surfaces);
- the forced inlet conditions can be modeled after actual historic meteorological data from the simu-

lated site—e.g., inlet air temperature, humidity, etc., can change minute-by-minute;

- highly scalable software running from workstation to many/multi-core systems and high-performance computer clusters;
- achieves real-time simulation speed for urban microclimate cases.

The models shown in Fig. 1 are for the most part a combination of standard CFD models for flow and radiation that have been extensively covered in literature (see Coelho et al. 1998; Knaus et al. 1999; Ismail and Salinas 2004; Pecka 2014; Cid and Vianna 2016; Sá da Costa 2016; Mould 2019). Solar radiation, for example, is implemented using the finite volume Discrete Ordinates Method (fvDOM). Absorption through vegetation (shading) is modeled using multi-band absorptivity and emissivity coefficients, i.e., “optical” leaf density.

Geometry basis is a combination of publicly available 3D data and manual building modeling. Gables are included in the building models. uhiSolver can read all 3D geometries the OpenFOAM library is capable of but has no own 3D modeler included. 3D modeling is done with external programs and importing geometry from common, industrial software for architecture is supported. The spatial simulation resolution is not uniform across the simulated volume; it is higher closer to the buildings (in the order of 0.3 m at the building surface) and lower further away from the buildings.

Scope of study

The study aims to simplify the modeling process of the above mentioned uhiSolver software. The main reason for the reduction of model complexity, i.e., level of inner detail for buildings, is to reduce manual work for setting up appropriate boundary conditions of buildings. For higher levels of internal detail each and every façade and roof would have to be treated differently because of its differing thermal coefficients, leading to an unfeasible and thus uneconomic complexity and amount of manual work in setting up large scale simulations. Although this is possible using the simulation software and it is not limited by algorithmic or modeling restrictions, the greatest parts of manual set-up work and program interaction were reduced to prioritize automation, scalability and ease of variability of input data over possible higher local modeling accuracy. The development and practical application of uhiSolver are therefore driven not only by scientific insights, but also by stringent economic considerations.

For better reading, this research work is divided into two parts, the first part (Sect. “[Generation of simplified material data](#)”) including the elaboration of the simplified

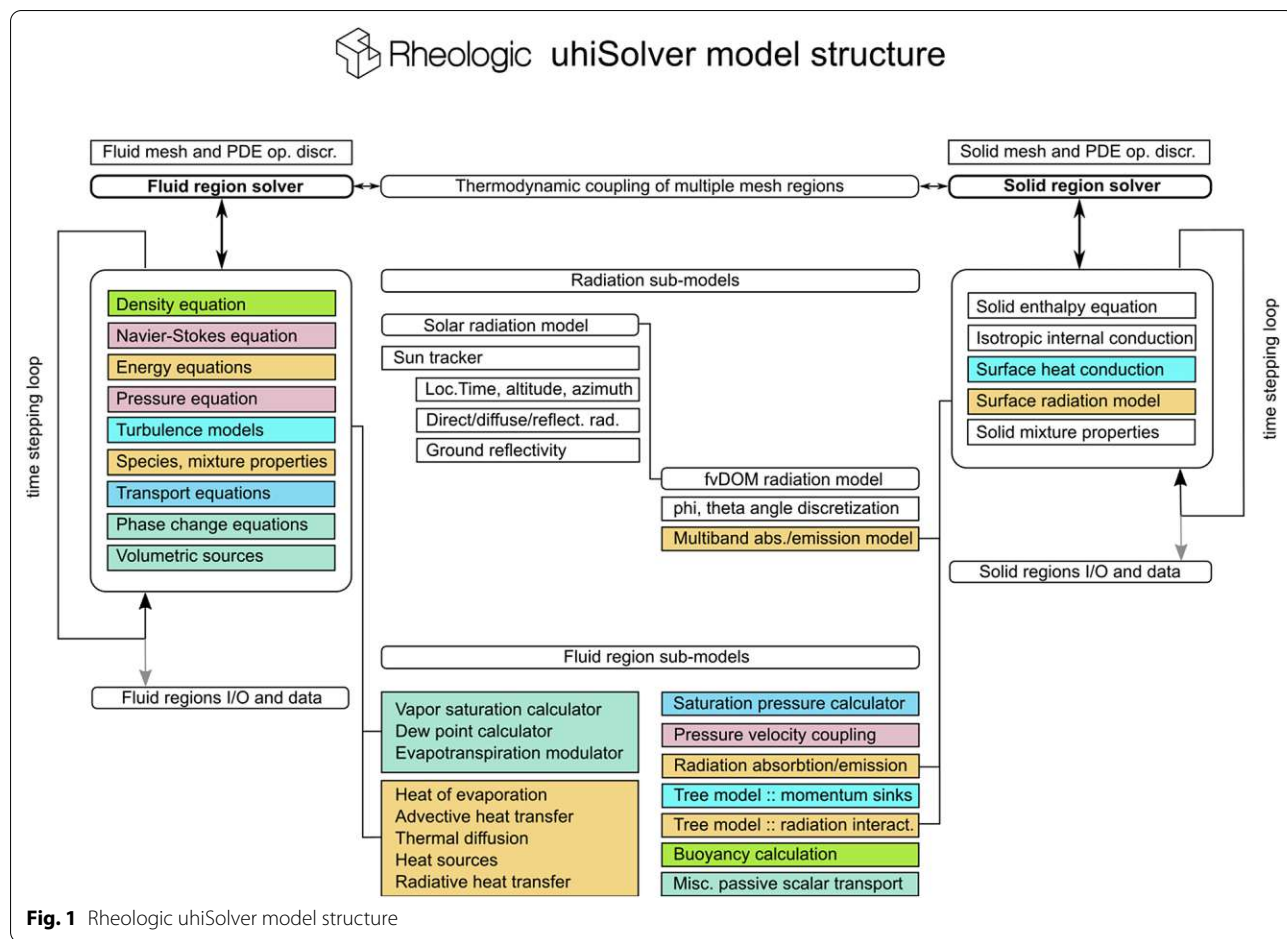


Fig. 1 Rheologic uhiSolver model structure

material data using a fictitious model building, whereas the second part (Sect. “Validation case Kandlgasse”) covers the validation on an actual residential block in Vienna. Furthermore, a recent larger scale model validation of a few urban blocks is provided in the Additional file 1: Appendix E.

In detail, specific algorithms as described in ÖNORM EN ISO 13786 are presented in the first part of this research work and applied to a fictitious building construction. Examining the two cases of a low U-value component (well insulated) and a high U-value component (poorly insulated), it is determined which components contribute to the heat storage capacity. Using this knowledge, simplified monolith components and corresponding material data are constructed that emulate the complex and layered component. On behalf of this newly derived monolith model, five building types representative of Viennese building styles are examined to determine which of the components in a real building composite may be omitted for future modeling purposes. Besides, five typical ground surfaces are defined to allow further simplifications of the modeling process.

Within the second part, using the uhiSolver software and taking into account the simplifications for building types and ground surfaces elaborated in the first part of this research work, dynamic 3D simulations are carried out for an intensively greened inner courtyard of a school in the seventh district of Vienna to determine air temperature, humidity, airflow velocities and radiation density within the courtyard and its surroundings. In order to validate the software, the simulation results are compared to measurement data collected in 2017 within the framework of the research project “Grün-PlusSchule” (Korjenic 2018), showing a good agreement. Based on these simulation results, the apparent temperature (Steadman 1994) is calculated to assess the impact of façade greening within a typical courtyard of a residential block on human thermal comfort.

Generation of simplified material data

In the course of the feasibility study for the development of a “black box model” for the assessment of the urban microclimate, the albedo, density, thermal resistance and specific heat storage capacity of buildings and ground

surfaces were identified as essential parameters. These parameters are used to calculate the thermal behavior of the different types of buildings and ground surfaces using the algorithm according to ÖNORM EN ISO 13786 (Austrian Standards Institute 2008).

For the definition of the five building types, the following typical Viennese building styles are chosen, which represent a large part of the Viennese building stock (see Fig. 2):

- Type G1: Gründerzeit building
- Type G2: reinforced concrete building of the 1970s
- Type G3: hollow brick building of the 1970s
- Type G4: new reinforced concrete building
- Type G5: new high-rise brick building.

Constructional systems of walls and ceilings corresponding to the respective epoch are included in the Additional file 1: Appendix A.

For the definition of the five ground types, the following typical ground surfaces of Vienna are chosen (see Fig. 3):

- Type B1: asphalt road
- Type B2: concrete road
- Type B3: paved road

- Type B4: gravel path
- Type B5: meadow.

For the calculation model, it is sufficiently accurate to consider the ground layers down to a depth of 1 m. The reason for this is that seasonal heat conduction only penetrates to about this depth due to the low thermal conductivity of soils and rocks. At night it is emitted as terrestrial, long-wave radiation (Clauser 2014). The individual layers of the ground surfaces are included in the Additional file 1: Appendix B.

Based on these building and ground types, one-dimensional model calculations are carried out in Microsoft Excel for only two time steps of one second in order to get three data points, which allows the derivation of the dynamic behavior for the temperature and heat flow at the building and ground surface depending on the three most influential parameters—albedo, area-related effective heat capacity and thermal resistance (this yields the simplified model parameters for the following transient simulations in uhiSolver which will be described in part two of this research work—see Sect. “Validation case Kandlgasse”).

Beforehand, the calculation model with the goal of simplifying the building components and ground types is presented, followed by the equations as described in



Fig. 2 Typical Viennese building types for the implementation in uhiSolver: G1 = Gründerzeit building, G2 = reinforced concrete building of the 1970s, G3 = hollow brick building of the 1970s, G4 = new reinforced concrete building, G5 = new high-rise brick building



Fig. 3 Typical Viennese ground surfaces for the implementation in uhiSolver: B1 = asphalt road, B2 = concrete road, B3 = paved road, B4 = gravel path, B5 = meadow

ÖNORM standards to determine where the heat transfer becomes negligible for engineering type calculations at building scale.

Calculation of the area-related effective heat capacity

In order to implement the building and soil properties and their influence on the ambient temperature into the uhiSolver software, a reduction of complexity is necessary. The goal of simplification is to model the whole building as a homogeneous monolith, with comparable thermal storage properties.

In the first step, the masses of the individual exterior and interior components as well as the total building mass are determined for each building type. An error tolerance of 5% is chosen. Thus, interior components with a mass fraction smaller or equal to 5% of the total mass can be neglected. Subsequently, it was determined which components contribute to the heat storage capacity. Based on the defined error tolerance of 5%, the point X of the construction was determined where the temperature gradient between the outside and inside temperature corresponds to 95%. The cross-sectional area between the outer surface and the point X just calculated stores heat.

Depending on the heat transfer coefficient of the external component, a distinction is made between two scenarios (see Fig. 4): Scenario 1: low heat transfer

coefficient (well insulated component)—heat storage through external components of reduced thickness; and scenario 2: high heat transfer coefficient (poorly insulated component)—heat storage by both external and internal components.

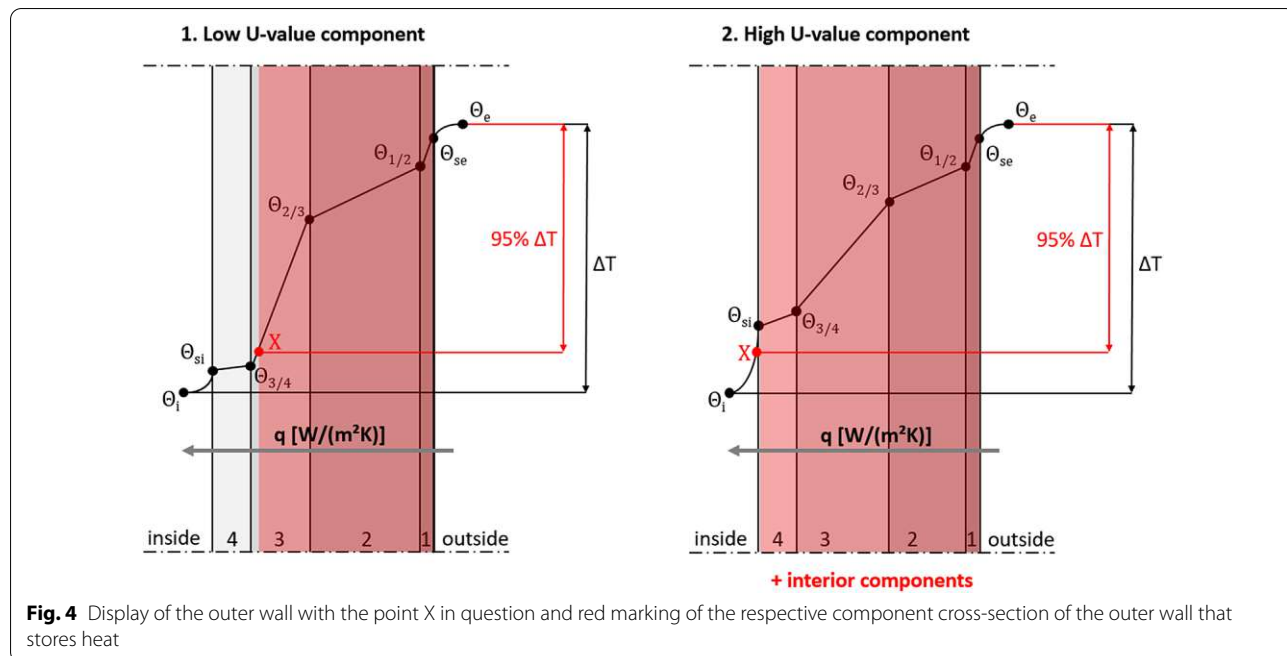
A green roof is a special case of modeling. For a building with a green roof, it is assumed that the construction will not be heated due to shading and evapotranspiration caused by the green roof as well as the insulation properties by soil substrate. Conversely, such roofs do also not radiate heat at night.

In the case of scenario 1 (insulated exterior component), the area-related effective heat capacity χ of the exterior components can be determined according to ÖNORM EN ISO 13786 (Austrian Standards Institute 2008):

$$\chi = \frac{T}{2\pi} \cdot \left(\left| \frac{Z_{11} - 1}{Z_{12}} \right| \right) \text{ in which } Z = Z_1 \cdot \dots \cdot Z_2 \cdot Z_1. \quad (1)$$

χ area-related effective heat storage capacity of the building component in $J/(m^2 K)$. Z heat transfer matrix. T period duration in s.

It should be emphasized that it is not the real component structure that is included in the calculation, but the reduced cross-section (external surface to point X).



Further simplifications must be made in the case of heat storage by means of exterior and interior components (scenario 2—uninsulated exterior component) so that the entire building can be described exclusively by the building envelope. Those interior components whose mass share is >5% of the total mass and those that contribute to heat storage are modeled as the innermost homogeneous layer of the outer shell. For this purpose, a fictitious material with weighted properties of the inner components is determined: a fictitious component layer is determined from the structure of the uppermost floor and added as the innermost layer of the roof structure; inner walls, standard floor slabs and stairs are also combined to a fictitious component layer and added on the inside of the external wall structure. The area-related effective heat capacity χ is calculated from the extended component cross-section (real component structure plus fictitious innermost component layer).

In order to take the albedo of the real building envelope into account, the short-wave albedo of the outer wall or roof and the solar reflectance of the windows are averaged in relation to the respective surface areas.

Without simplifications, the ground can be considered as a monolith consisting of a homogeneous body and a surrounding boundary surface. For the calculation of the heat storage capacity, the procedure is the same as for buildings. First the point X is determined and then the heat-storing part of the ground structure is identified. The albedo of the monolith corresponds to the albedo of the actual ground surface. No averaging is necessary.

Temperature and heat flow at the building/ground surface
The one-dimensional model calculations on a fictitious building, as described below, were carried out in the context of the master thesis of Christina Maria Baumgartner at Vienna University of Technology (Baumgartner 2019). The presented calculation model for the temperature and heat flow at the building and ground surface was used exclusively within the scope of this master thesis to derive a tendency for the different parameters (temperatures and heat flow) depending on albedo, heat capacity and thermal resistance.

To calculate the temperature changes during the course of the day and the heat flow at the surface of the building, within these simplified model calculations the monolith is considered as a homogeneous body surrounded by an infinitely thin interface between the solid and the surrounding air. A stationary state is assumed in which the inside and outside temperature and, as a result, the heat flow density q are constant. Supposing a uniform temperature distribution on the outer wall surface, according to Mu et al. (2018) the steady-state heat balance can be described as

$$q_{\text{solar}} = q_{\text{conduc}} + q_{\text{convex}} + q_{lw}, \quad (2)$$

with the absorbed solar radiation being calculated as

$$q_{\text{solar}} = q_s \cdot (1 - \rho_s) \quad (3)$$

q_{solar} absorbed solar radiation in W/m^2 . q_{conduc} heat conduction from the outer wall surface to inner in W/m^2 . q_{convex} heat convection exchange between the outer wall

surface and the ambience in W/m^2 . q_{lw} long-wave radiation heat exchange between the outer wall surface and the surroundings in W/m^2 . q_s heat flux density of solar radiation on the earth's surface in W/m^2 . ρ_s short-wave albedo.

The calculation of the temperature and the heat flow at the building surface is performed separately for the fictitious exterior wall and the fictitious roof of each building type using the equations given in Sect. "Day" (day) and "Night" (night). In the first step, the following boundary conditions must be defined for the calculation:

- Solar radiation q_s (day) or long-wave counter radiation q_{lw} (night) in W/m^2 ;
- Temperature difference between outside air temperature T_a and fictitious homogeneous inside temperature T_{i0} in K;
- Heat transfer coefficient U in $\text{W}/(\text{m}^2\text{K})$;
- Area-related heat capacity χ in $\text{kJ}/(\text{m}^2\text{K})$;
- Short-wave albedo ρ_s .

The fictitious homogeneous internal temperature T is the internal temperature of the homogeneous monolith. This temperature is not the real internal temperature, but a temperature averaged over all relevant components. The monolith has two temperatures: a homogeneous temperature of the building and a homogeneous

temperature of the surface. For the determination of the internal temperature of the monolith, the temperature gradient in the external components is decisive, as for the determination of the relevant component cross-section. Depending on the heat transfer coefficient, again a distinction is made between two scenarios (see Fig. 5):

Scenario 1: low heat transfer coefficient

The temperature at point X is used for the fictitious homogeneous interior temperature and the room-side heat transfer resistance R_{si} is zero:

$$T_{i0} = T_a - 0.95 \cdot \Delta T, \quad (4)$$

$$R_{si} = 0. \quad (5)$$

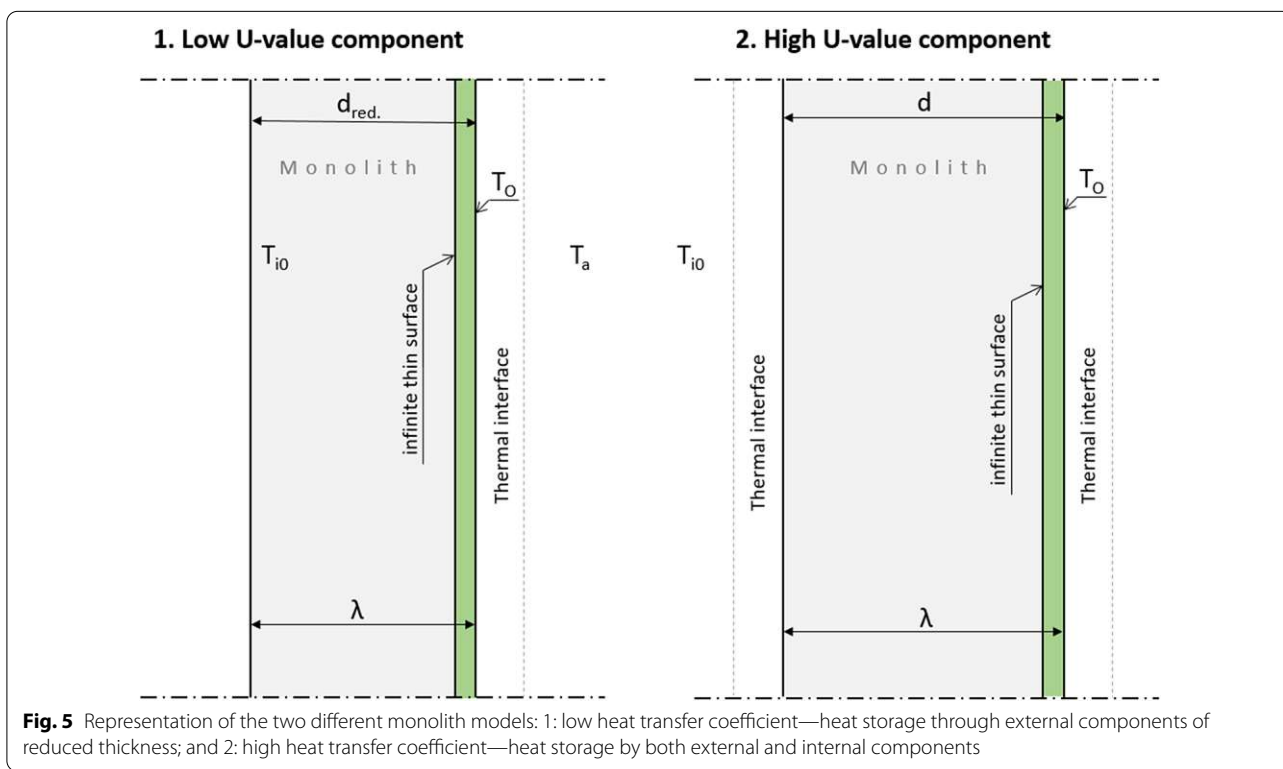
Scenario 2: high heat transfer coefficient

The real interior temperature T_i of the building is used in the first step for the fictitious homogeneous interior temperature. The room-side heat transfer resistance is not equal to zero:

$$T_{i0} = T_i, \quad (6)$$

$$R_{si} \neq 0. \quad (7)$$

The calculation of the temperature and the heat flow at the ground surface is identical. The explanations are



therefore limited to the observation of the building surface.

The following two sections describe in detail how the temperature and the heat flow at the building surface are calculated within the one-dimensional model calculations in Microsoft Excel. A distinction is made between day and night, with the equations differing mainly by the solar radiation during the day and the direction of heat flow. The boundary conditions used are presented in Sect. "General boundary conditions".

Day

During the day, the surface of a building heats up due to solar radiation and by contact with warm air. Part of the solar radiation is immediately reflected when it hits the surface and therefore does not contribute to the heating of the building. The other part is absorbed and converted into heat. Depending on the building materials used, the heat is stored as thermal energy in the building components, conducted further inside and subsequently heats the interior. In the calculation model, the heat input through unshaded windows is taken into account by choosing a higher fictitious interior temperature as a boundary condition.

The change of the surface temperature and the heat flux density between the surface and the surrounding air after a defined time unit can be determined iteratively by means of the following four calculation steps (see Eqs. (8) to (11) and Fig. 6). The time unit of one calculation process is chosen small enough (e.g., 1 s) to obtain valid results. If the plus/minus sign of the heat flow density is positive, heat flows from outside to inside; a negative sign means the opposite direction of flow.

- heat conduction—heat flow $q_{L,1}$ due to temperature difference, resulting in a rise of the fictitious homogeneous internal temperature of the monolith

$$q_{L,1} = \frac{1}{R_T} \cdot (T_a - T_{i0}). \quad (8)$$

$q_{L,1}$ heat flow due to temperature difference in W/m². R_T total heat transfer resistance of the component including the heat transfer resistance of the inner and outer surface in m² K/W. T_a outside air temperature in K. T_{i0} fictitious homogeneous internal temperature at the beginning of the first time step in K.

- thermal radiation and convection—fictitious outer surface temperature T_{O1f} due to solar radiation

$$T_{O1f} = T_a + (q_{solar} + q_{L,1}) \cdot R_{se}. \quad (9)$$

T_{O1f} fictitious outer surface temperature of the monolith in K. R_{se} heat transfer resistance of the outer surface in m² K/W.

- updated heat conduction—heat flow q_1 in the monolith and updated fictitious homogeneous internal temperature T_{i1}

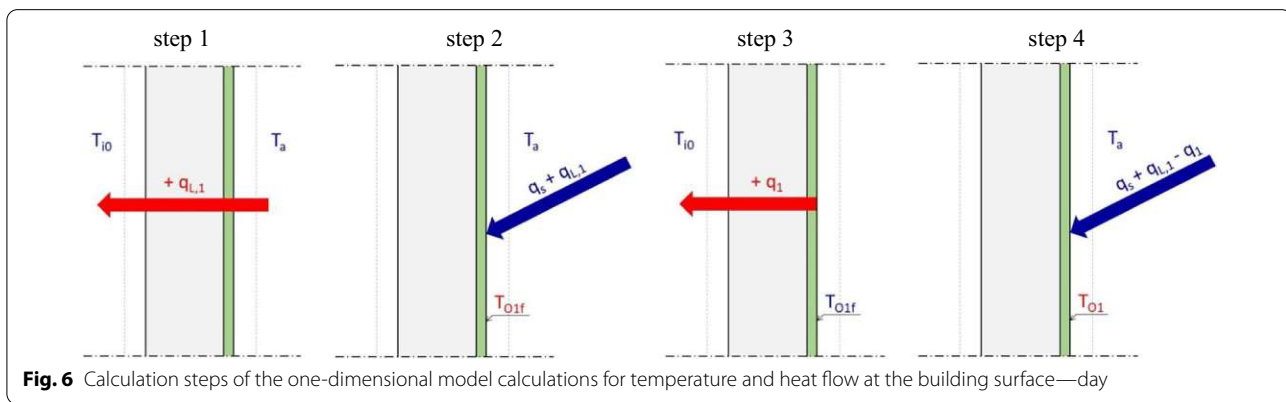
$$T_{i1} = T_{i0} + \Delta T = T_{i0} + \frac{q_1 \cdot t}{\chi}. \quad (10)$$

T_{i1} fictitious homogeneous internal temperature after the first time step in K. q_1 heat flow from the outer surface to the inner of the monolith in W/m². t duration of the time step in s.

- heat flow and actual surface temperature T_{O1} at the outer component surface:

$$T_{O1} = T_a + (-1) \cdot (-q_{solar} - q_{L,1} + q_1) \cdot R_{se}. \quad (11)$$

T_{O1} actual surface temperature at the outer component surface in K.



Night

A calculation model is implemented which can assess the night-time cooling of buildings. However, in urban areas the night-time heat radiation at ground level is usually very low (Fischer et al. 2008). The dense construction reduces the view to the sky and the façades partially irradiate each other.

The iterative calculation of the surface temperature and the heat flux density between the surface and the surrounding air is carried out analogous to the calculation during the day using the following calculation steps (see Eqs. (12) to (15) and Fig. 7):

- heat conduction—heat flow $q_{L,1}$ due to temperature difference, resulting in a decrease of the fictitious homogeneous internal temperature of the monolith:

$$q_{L,1} = \frac{1}{R_T} \cdot (T_a - T_{i0}). \quad (12)$$

- heat radiation and convection—heat flow q_{a1} between the heated surface T_{O1f} and the outside temperature T_a :

$$q_{a1} = \frac{1}{R_{se}} \cdot (T_a - T_{O1f}) = \frac{1}{R_{se}} \cdot (T_a - T_O - q_{L,1} \cdot R_{se}) \quad (13)$$

q_{a1} heat flow between the heated outer surface and the outside air in W/m^2 . T_O initial component surface temperature according to Table 1 in K.

- updated heat conduction—fictitious homogeneous internal temperature T_{i1} :

$$T_{i1} = T_{i0} + \Delta T = T_{i0} + \frac{q_1 \cdot t}{\chi}. \quad (14)$$

- heat flow and actual surface temperature T_{O1} at the outer component surface:

$$T_{O1} = T_a + (-1) \cdot (q_{a1} + q_1) \cdot R_{se}. \quad (15)$$

General boundary conditions

For the one-dimensional model calculations, assumptions are made about the outside temperature, the fictitious inside temperature and the surface temperature at night (see Table 1). The heat transfer resistances are determined depending on the direction of heat flow (see Table 2). The solar heat flux density is assumed to be 500 W/m^2 . With flat roofs, the external heat transfer resistance is assumed to be significantly higher than the standard value because the gravel protects the roof structure from wind. For the calculation of the surface temperatures and heat flows of the ground types, there is no heat transfer resistance inside because the ground has an infinite depth and is not surrounded by a medium. Therefore, only the external heat transfer resistance is considered in the thermal calculations.

Calculation parameters

In order to be able to assess which building components can be neglected due to the defined error tolerance of 5% for the respective building types, model calculations are carried out on a three-storey apartment building with a gross floor area of 288 m^2 (floor plan see Fig. 8). The façade is considered to be uniformly painted white with an albedo of 0.7. The average room height of the Gründerzeit building is assumed to be 3.6 m. For the

Table 1 Initial temperatures used within the one-dimensional model calculations

Initial temperatures	Day (°C)	Night (°C)
Outside air temperature	30	24
Fictitious indoor temperature buildings	20	29
Fictitious indoor temperature ground	11	11
Component surface temperature	–	25

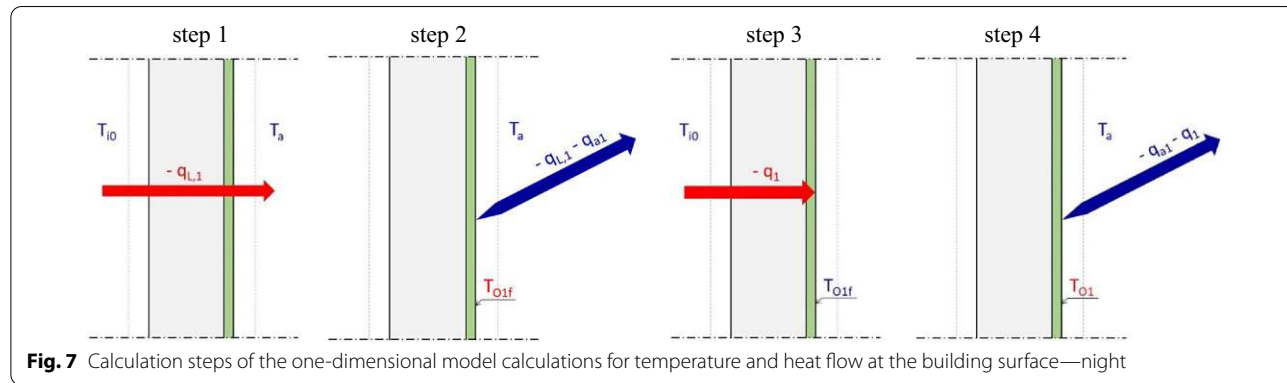


Table 2 External and internal heat transfer resistances of the building components and ground surfaces used within the one-dimensional model calculations (Maiullari et al. 2018)

Component	Day		Night	
	R_{se} [W/(m ² K)]	R_{si} [W/(m ² K)]	R_{se} [W/(m ² K)]	R_{si} [W/(m ² K)]
External wall	0.04	0.13	0.04	0.13
Pitched roof	0.04	0.17	0.04	0.10
Flat roof	0.13	0.17	0.13	0.10
Ground surface	0.04	0.00	0.04	0.00

buildings of the 1970s and the new buildings, it is set at 2.6 m.

In the Gründerzeit (from about 1850 to 1914), stairs were made of natural stone, especially limestone or quartz sandstone (*Kaiserstein* or *Rekawinkler* stone) (Ahne 2014). Therefore, for the building type Gründerzeit building a *Rekawinkler* stone is used as staircase material. In the buildings of the 1970s and the new buildings, the calculations are based on stairs in reinforced concrete construction.

The Gründerzeit building and the buildings of the 1970s are calculated with an uninsulated pitched roof with clay roof tiles. The albedo of the red roof skin is 0.225. For the new buildings a flat roof with a gravel covering is considered. The albedo of the flat roof is 0.13 (see Table 3). The internal loads and the heat-storing mass of the facility are neglected.

The assumptions regarding the albedo of the five ground surfaces are given in Table 4.

Simplifications

Based on the calculations carried out on the example building described above, the following components are found to be negligible within the defined error tolerance of 5%:

- neglecting building components due to their mass percentage < 5%

For all types of buildings, the stairs can be neglected when calculating the surface temperature and the heat flow, due to their low mass percentage of the total mass, which is less than 5%.

- neglecting building components when calculating the heat capacity

In new buildings made of reinforced concrete or vertically perforated bricks, the interior components contribute only insignificantly to heat storage. The roof and the outer wall have good thermal insulation properties

and minimize the entry of heat into the interior. Table 5 shows the types of buildings for which the contribution of the interior components to heat storage can be neglected.

Sensitivity analysis

The three parameters—albedo, area-related effective heat capacity and thermal resistance—have a significant influence on the surface and interior temperature of building and ground types. In order to be able to determine this influence, the parameters are varied within the one-dimensional simulations, which are run for two time steps in Microsoft Excel. For each parameter and building or ground type three values are used for the sensitivity analysis: the actual value, a reduced value (50%) and an increased value (150%). Subsequently, trends of the fictitious indoor or surface temperature depending on the three parameters are generated. This can be used to determine how sensitive a type is to a parameter.

In terms of the fictitious indoor temperature, building type G4 (new concrete building) is the least sensitive to a change in all three parameters. Building type G3 (1970s brick building) is the most sensitive to a change in heat capacity of the exterior wall, whereas building type G2 (1970s concrete building) is the most sensitive to a change in albedo and thermal resistance. In the case of ground surfaces, type B3 (paved road) is the least sensitive. Contrarily, ground type B5 (meadow) is the most sensitive to a change in thermal resistance and ground type B1 (asphalt road) is the most sensitive to a change in albedo as well as heat capacity.

In the case of the exterior roof components, a relationship can be established between the absolute value and the sensitivity: the greater the heat capacity, the lower is the sensitivity to a change. This statement is also valid for the thermal resistance of the roof components. For the exterior wall constructions, though, there is no correlation noticeable. With increasing heat capacity, the sensitivity of the fictitious interior temperature to a change in the three parameters decreases. In general, the sensitivity of the fictitious internal temperature of the building and ground monoliths is greatest to a change in thermal



Fig. 8 Floor plan of all floors of the three-storey apartment building used within the model calculations to assess which building components of the respective building types can be neglected (Natanian et al. 2019)

Table 3 Calculation parameters of the five building types used within the one-dimensional model calculations

Building type	Construction method	Room height (m)	Staircase material	Roof	Albedo	
					Roof	Façade
Type G1	Gründerzeit building	3.6	Stone	Pitched roof	0.225	0.7
Type G2	Concrete building 1970s	2.6	Concrete	Pitched roof	0.225	0.7
Type G3	Brick building 1970s	2.6	Concrete	Pitched roof	0.225	0.7
Type G4	New concrete building	2.6	Concrete	Flat roof	0.13	0.7
Type G5	New brick building	2.6	Concrete	Flat roof	0.13	0.7

Table 4 Assumptions of the albedo of the five ground surfaces used within the one-dimensional model calculations

Ground type	Construction method	Albedo
Type B1	Asphalt road	0.125
Type B2	Concrete road	0.225
Type B3	Paved road	0.275
Type B4	Gravel path	0.1
Type B5	Meadow	0.2

Table 5 Relevance of the interior components with regard to heat storage according to the results of the one-dimensional model calculations

Building type	Construction method	Interior components relevant?
Type G1	Gründerzeit building	Yes
Type G2	Concrete building 1970s	Yes
Type G3	Brick building 1970s	Yes
Type G4	New concrete building	No
Type G5	New brick building	No

resistance, then to a change in albedo and least to a change in heat capacity.

In order to validate the uhiSolver software after implementation of the gained knowledge on the basis of a real object, in part two of this research work (see Sect. “Validation case Kandlgasse”), the simulation results of a residential block in Vienna are compared with measurement data collected on site.

Validation case Kandlgasse

The aim of the implementation of the simplified material data for the five most common types of building volumes and ground surfaces in the simulation software uhiSolver is to verify the forecast quality of the applied model, i.e., the sensitivity of the simulated air temperature with respect to the averaging of heat capacity, heat conduction

and specific density (c_p , λ , ρ). The physical boundary conditions (initial temperatures and heat transfer resistances) as well as the surface properties (albedo) listed in the first part of this research work (see Sect. “Generation of simplified material data”) are also incorporated into the model parameters.

Simulation setting

Within the framework of the research project “Grün-PlusSchule” (Korjenic 2018), funded by the FTI initiative Stadt der Zukunft 2nd call for proposals, a measurement campaign was carried out between May 2015 and May 2018 at the school GRG 7 Kandlgasse in Vienna, which was intended to investigate the effect of façade greening on outside and inside temperatures as well as heat flows within the masonry. As shown in Fig. 9, different greening measures were applied within the inner courtyard and on top of the roof of the school’s gymnasium. The measurement data collected on site were air temperature and relative humidity behind (ventilation gap) and in front of the façade greening as well as on the greened roof. The instruments used to measure air temperatures were Lin Piccos A05. They were fitted with a radiation shield. Measurements were taken at 5- to 10-min intervals over the entire project period. The data collected in summer 2017 are used to validate uhiSolver and are compared with the simulation results.

The date of the simulation is August 1, 2017, a cloudless hot day with inner-city temperatures of 35 °C, which were also measured in Kandlgasse in the afternoon.

Numerical details

Temporal coupling between heat conduction in building envelopes and CFD is performed as full two-way coupling with methods and algorithms also used in chtMultiRegionFoam, a conjugate heat transfer solver included in OpenFOAM. A modified solar calculator library is implemented in OpenFOAM. Heat conduction iteration and coupling is 1:1 in the solver; heat conduction is solved every time step. Radiation (due to high computational demand) is solved every n fluid iterations. Sun position is updated every 10 min of the

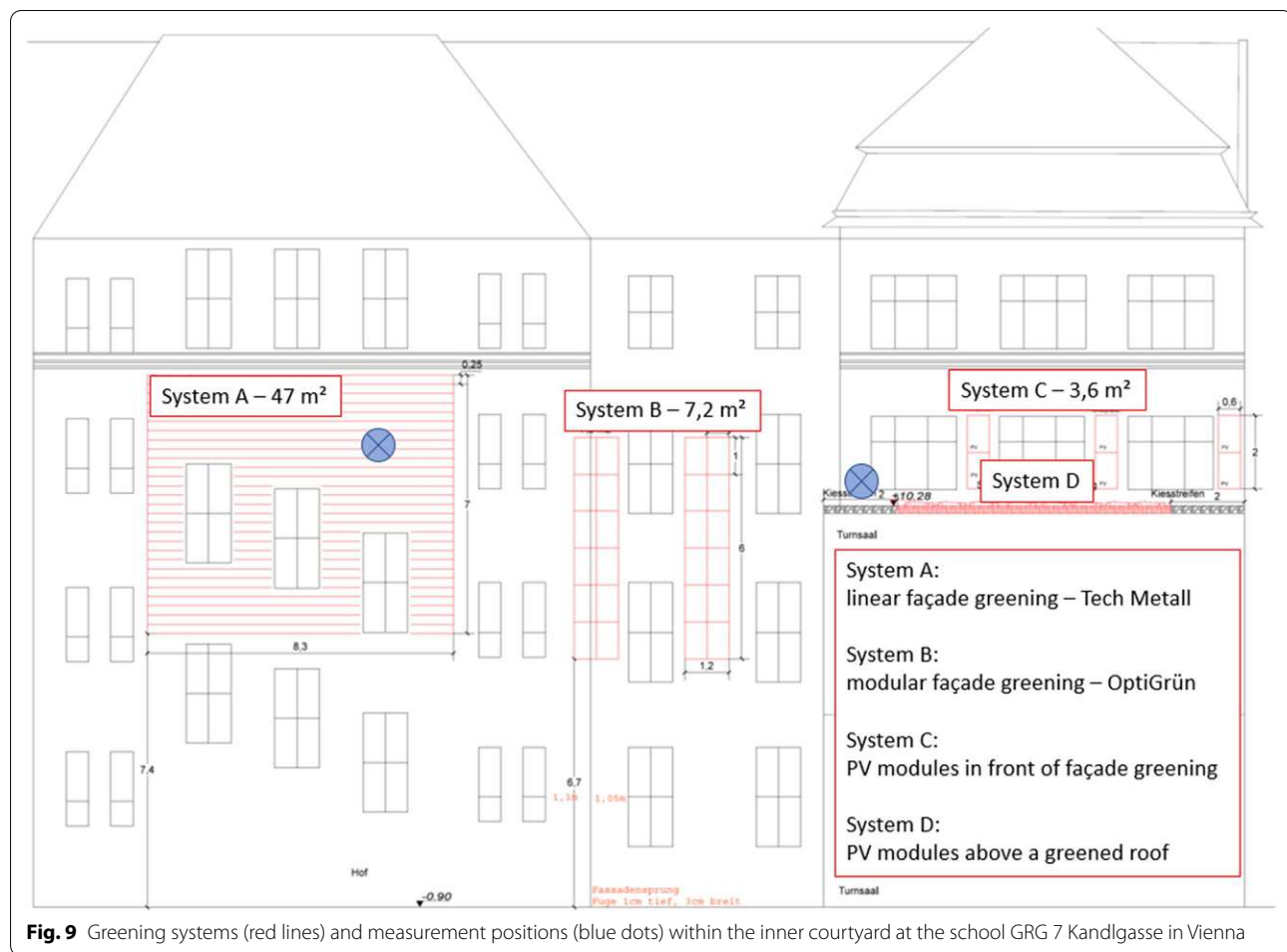


Fig. 9 Greening systems (red lines) and measurement positions (blue dots) within the inner courtyard at the school GRG 7 Kandlgasse in Vienna

simulated time. Radiation model is multi-band and active throughout the simulation, under “day” (sun elevation angle $> 0^\circ$) and “night” (sun elevation angle $< 0^\circ$, solar radiation off) conditions.

In addition to the interaction of radiation and air with the buildings, existing plants (green walls, trees) are fully included in the simulation with all their thermodynamic effects: reflection, shadows and evapotranspiration. In the current version of uhiSolver all vegetation zones are treated the same:

- Evapotranspiration rate is modulated by local radiation density and dry bulb temperature and limited by local relative humidity (driving force) and local wind-speed (transport limitation).
- Appropriate sink terms are used for radiation (optical absorption and emission coefficients) and momentum (via porosity terms).
- Any substrate material not in direct contact with a building is not considered in the current version.

Within the vegetation model in uhiSolver transpiration of plants is taken into account as follows:

- Local water vapor pressure and water vapor saturation pressure is calculated using Antoine equation.
- Local dew point and saturation loading are derived from Antoine equation.
- Zero evapotranspiration rate is reached if local conditions are saturated (100% RH).
- Max evapotranspiration rate is reached if local RH is very low and local evapotranspiration modulator (due to temperature and radiation) is very high.
- Specific leaf density goes into Darcy–Forchheimer coefficients of porous zone of finite volume cells designating vegetation and also into absorption/emission coefficients for solar radiation damping (shading) of said volume zones.
- Heat for evapotranspiration (modulated and limited by above parameters) is taken directly out of

fluid finite volume cell (taking into account thermodynamic gas mixture properties).

- Local state is updated immediately; temperature, saturation, loading, density and solver advances to next module and solves for dynamic pressure and velocity in next time-step.

The used simulation models, discretization algorithms and matrix solver settings for the fluid phase (air) are:

- Compressible, buoyant, unsteady simulation with forcing of log profile in-flow of wind-speed, time-varying and height constant humidity loading, time-varying and height constant temperature and time-varying incoming solar radiation vector and intensity
- Turbulence model is k-epsilon based with modified model constants suitable to achieve horizontal wind profile stability for applications of atmospheric boundary layer flows
- Pressure–velocity coupling using the PIMPLE algorithm for stabilization of local conditions, which can cause the CFL number to be greater than one temporarily
- Adaptive time stepping to keep maximum CFL number constant in fluid domain
- Temporal (backwards differencing) and spatial (upwind differencing of fluxes) discretization having 2nd order accuracy
- Central differencing (with corrections) is used for gradient calculations and Laplacian based schemes
- Solution of density field using Pre-conditioned Conjugate Gradient solver with solution tolerance of $1e-7$
- Solution of discretized radiation directions (via fvDOM model) using Generalized Algebraic Multigrid solver with symmetric Gauss–Seidel smoother with solution tolerance $1e-4$
- Solution of other variables using Pre-conditioned Bi-conjugate gradient solver with stabilization and solution tolerance $1e-7$
- Pressure–velocity coupling is active for all time steps and no frozen flux approach is employed to keep solution coupling tight.

The used simulation models, discretization algorithms and matrix solver settings for solid phases (building volumes and ground) are:

- Time discretization: forward Euler
- Interpolation: central differencing, Laplacian schemes: central differencing using correction.

For further information, some basic equations and their implementation in uhiSolver are included in the supplementary material (Additional file 1: Appendix C).

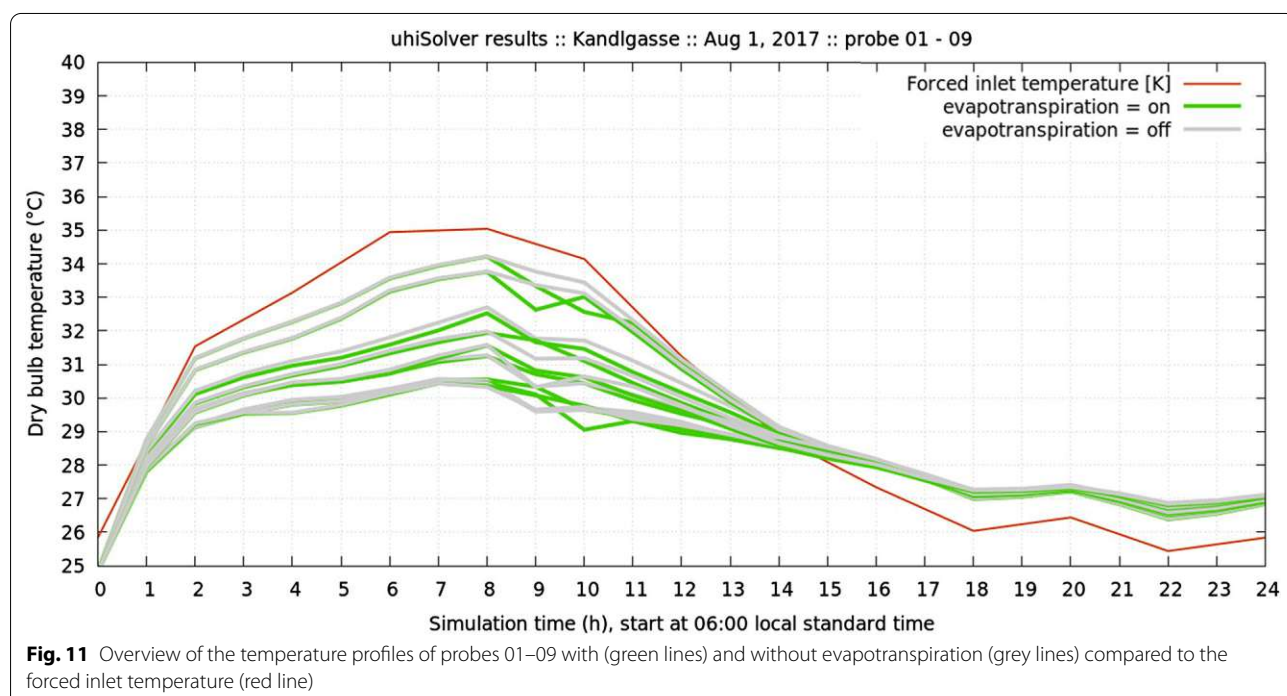
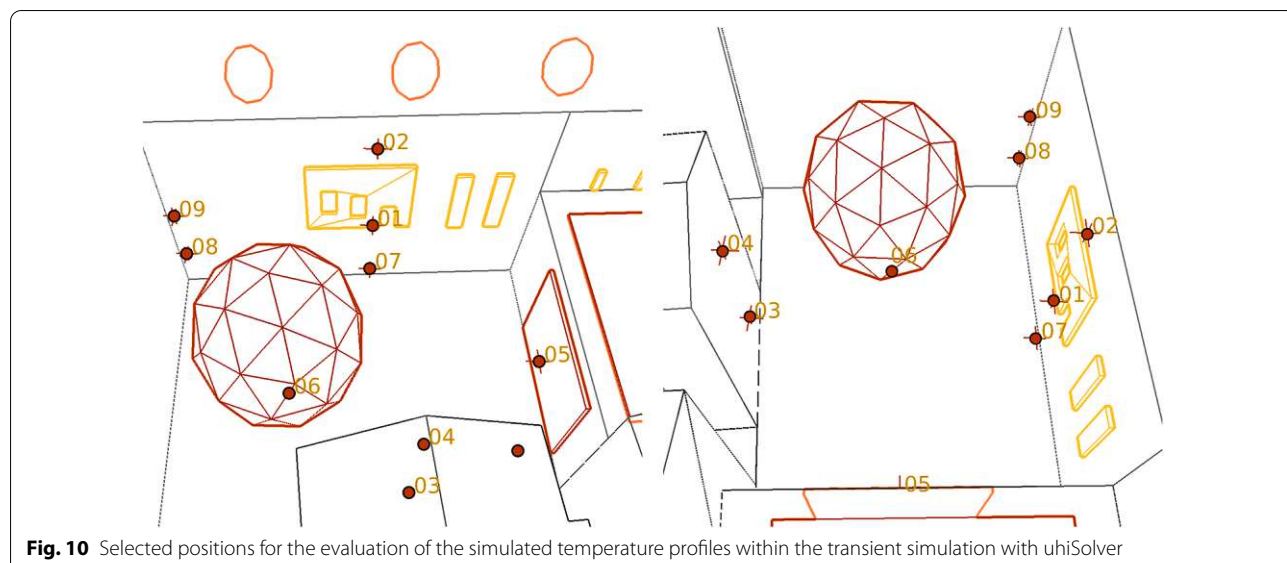
The simulation approach of uhiSolver shall be scaled from single city-block (as shown in this publication) to neighborhood level (10 blocks, ongoing research). Dealing with more blocks necessitates a simplified geometry and boundary condition work-flow and automation procedures to enable effective microclimate simulations and affordable parameter studies as the labor costs for manual program interactions significantly outweigh computational costs. The presented results are the first steps in this direction.

Simulation results

The results of the uhiSolver simulation for the selected day are shown as temperature profiles over the first 24 h of the simulation for nine different positions within the inner courtyard. Measurement data are available for only one position and are compared with the simulation results (detailed information on the experimental and simulation data is provided in the Additional file 1: Appendix D. Subsequently, 2D and 3D renderings of the apparent temperature, air temperature, air flow velocity, relative humidity, radiation density and incident surface radiation of the courtyard and its surroundings are presented for the hottest time of the day (14:00 CEST).

The selected positions (probe 01 to probe 09) are given in Fig. 10. The temperature profiles (radiation protected, i.e., shaded temperature) of each position are superimposed in Fig. 11, showing the temperatures with and without evapotranspiration compared to the forced inlet temperature. The impact of evapotranspiration on the simulated temperatures is almost negligible, as can be seen in Fig. 12 (giving the simulation results for probe 01 behind the south oriented façade greening), and decreases rapidly with increasing distance from the façade greenery. The temporarily slightly increased temperatures in the simulation with evapotranspiration is explained by minimally changed flow conditions due to buoyancy and density differences because of evaporation and mixing of air from warmer layers.

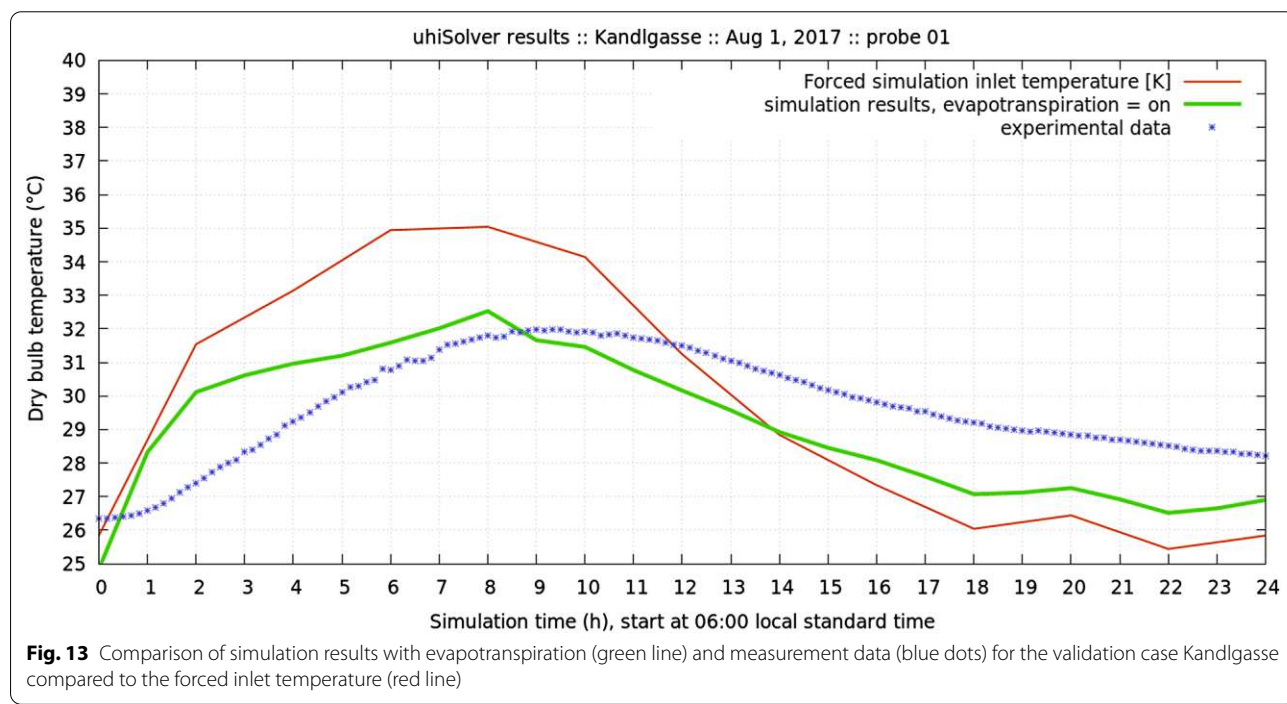
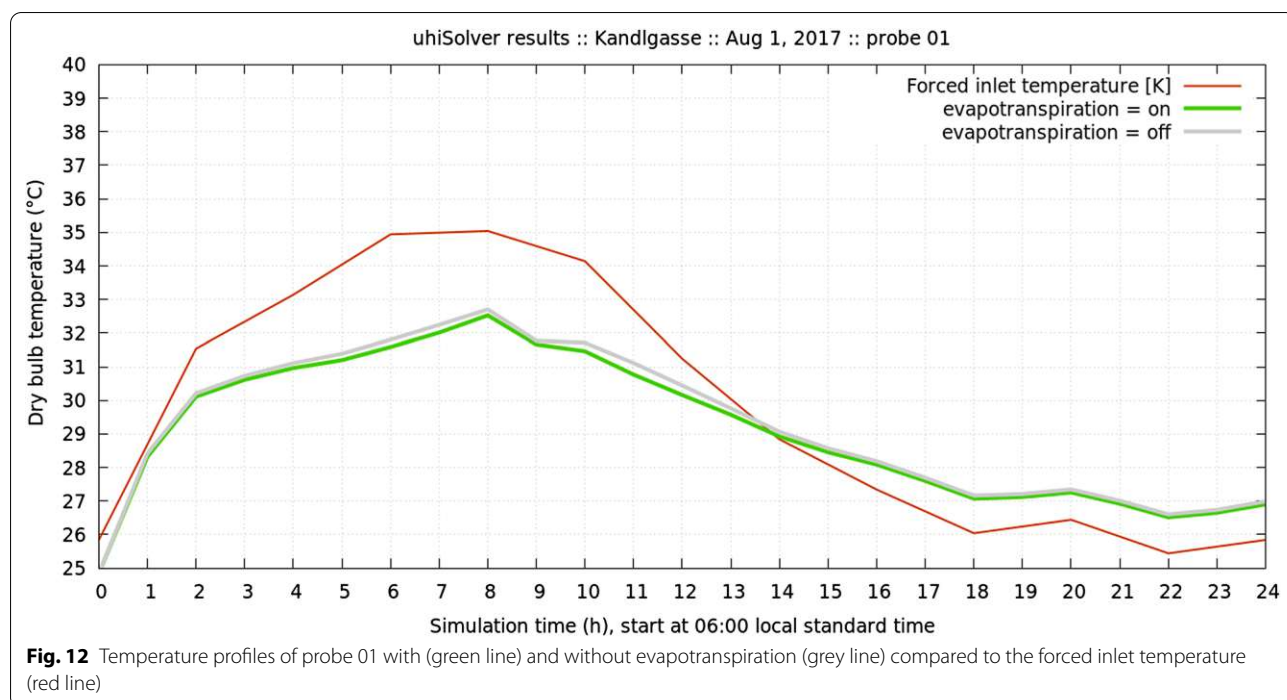
A comparison of the measured data of air and surface temperatures with the simulation results shows a good accordance. With respect to the air temperature in the area of the façade greening, the deviation between measured data and simulation results is small, especially in the afternoon and evening hours. The absolute error between measurement data and simulation results is within ± 2 Kelvin for the validation case (see Figs. 13 and 14). The largest deviations occur in the morning hours between 7 and 9 o'clock as well as after 6 o'clock in the evening. The reason for this is homogenous initialization



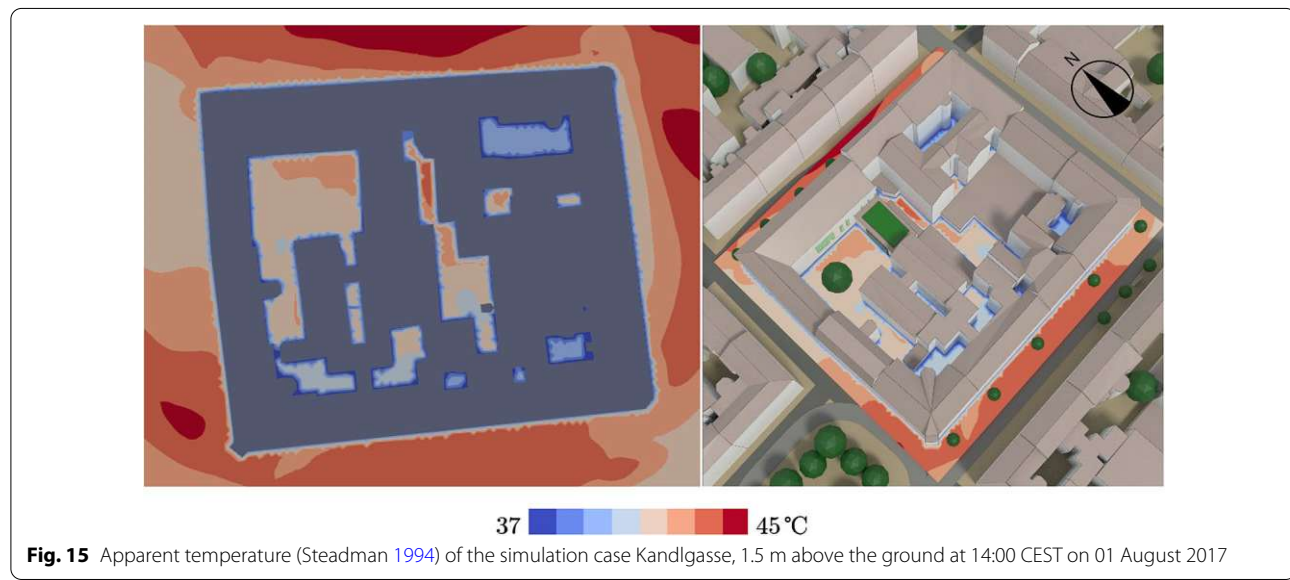
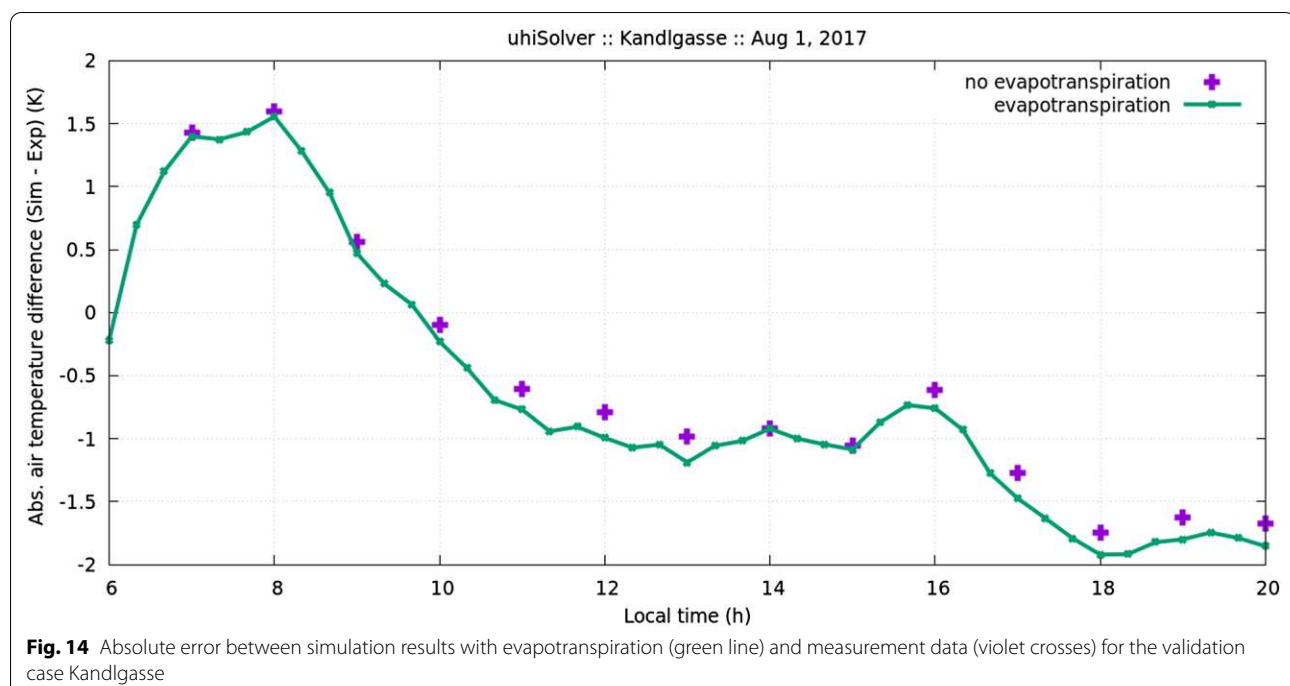
of building temperatures and over-simplification of evapotranspiration kinetics, with evapotranspiration rates (mm/day) being calculated based on measurement data from 2017 available for the monthly average water use of the façade greening system “Techmetall”. This is a field of active code development and research and future versions of uhiSolver will improve accuracy in that regard.

The evaluation of the simulation results clearly shows that the apparent temperature (Steadman 1994)

in the greened inner courtyard is comparable to that of the adjacent streets and in some cases even higher (see Fig. 15). However, the air temperature, measured in the shadow and without the influence of radiation, is 2 °C below that of the surrounding area (see Fig. 16), which is due to the cooling capacity of the plants and the lower albedo. The reasons for this are:



- lower air flow velocities in the inner courtyard (hardly any wind and therefore hardly any moisture removal, see Fig. 17),
- higher relative humidity in the inner courtyard compared to the surrounding streets due to the evapotranspiration of the plants (see Fig. 18) and

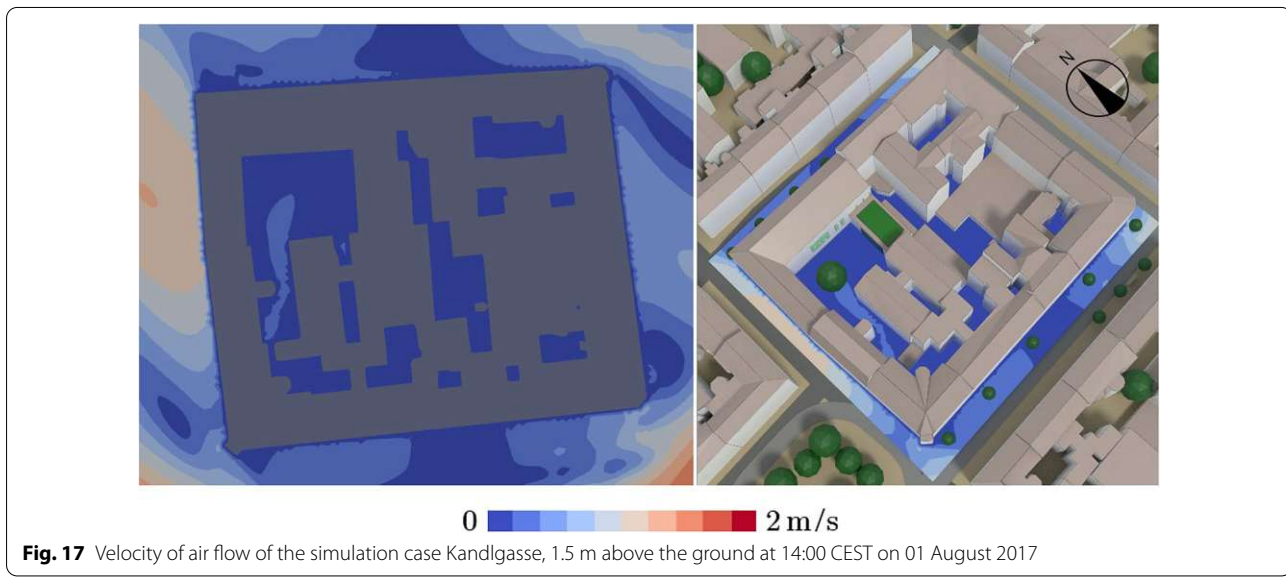
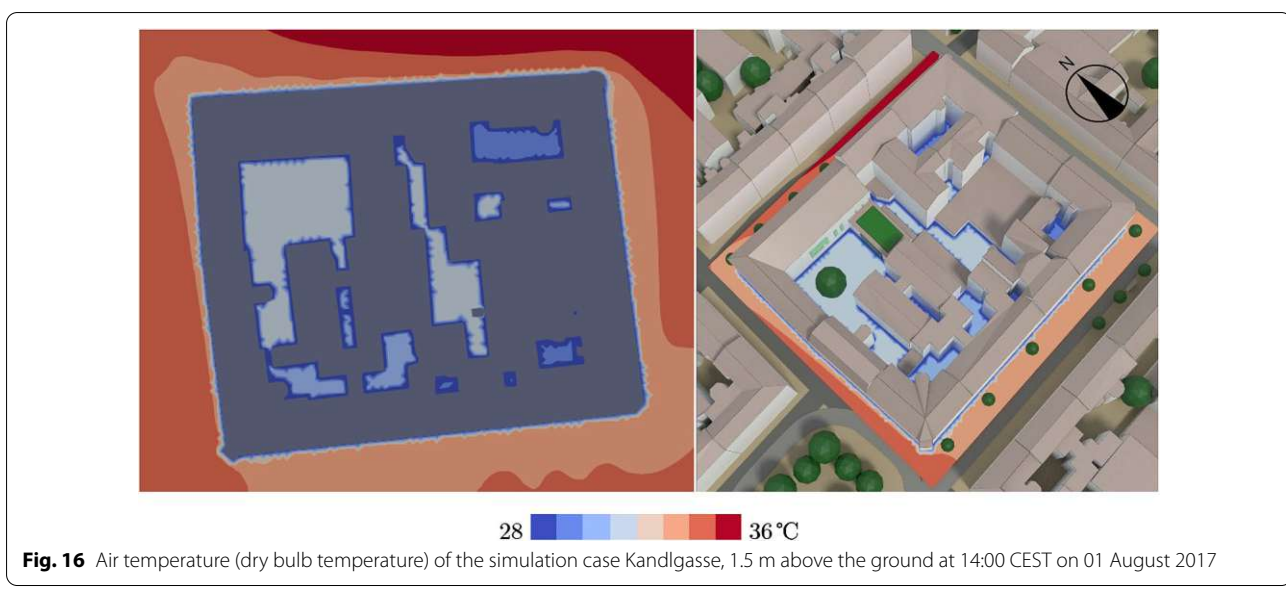


- 'spandrels' in the inner courtyard with direct radiation and additionally reflected secondary radiation of the walls (see Fig. 19).

Representative instantaneous fields were chosen at the apex of urban heat after midday (at 14:00 CEST). For better understanding, the above mentioned

illustrations (Figs. 15, 16, 17, 18, 19) are shown as 2D section and 3D rendering at the same time.

The incident radiation (W/m^2) on the surfaces is shown as a blackbody color scheme in Fig. 20 to illustrate the hot 'spandrels' with IR reflections. It is noticeable that the highest radiation intensities occur in the corners of the inner courtyard. These are also exactly



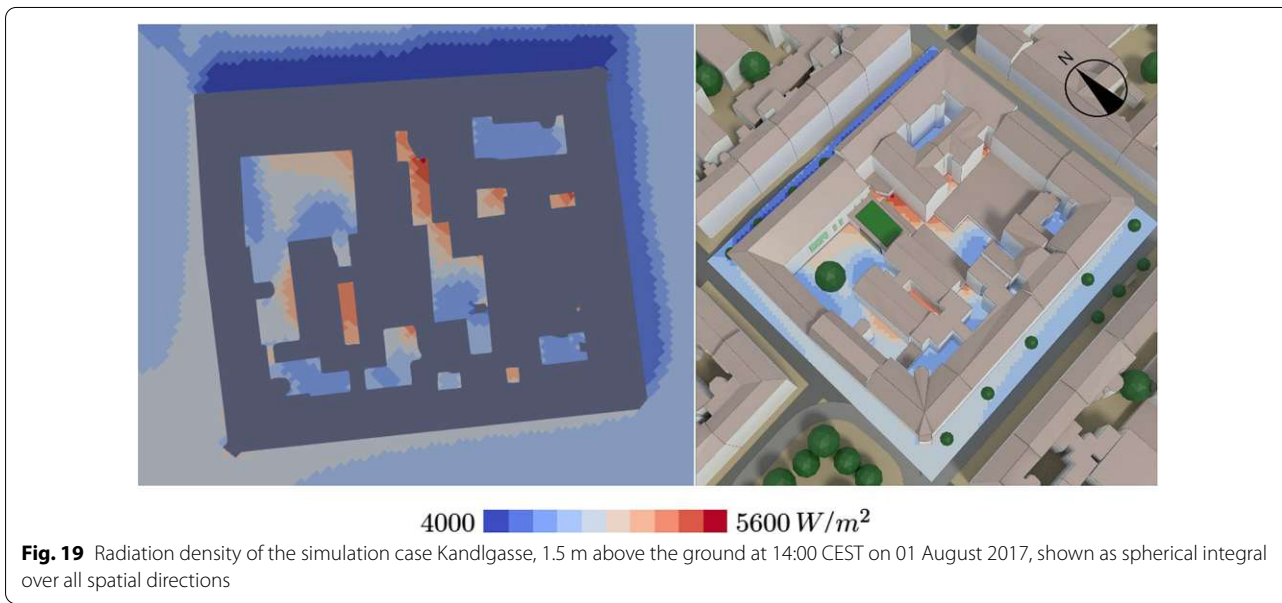
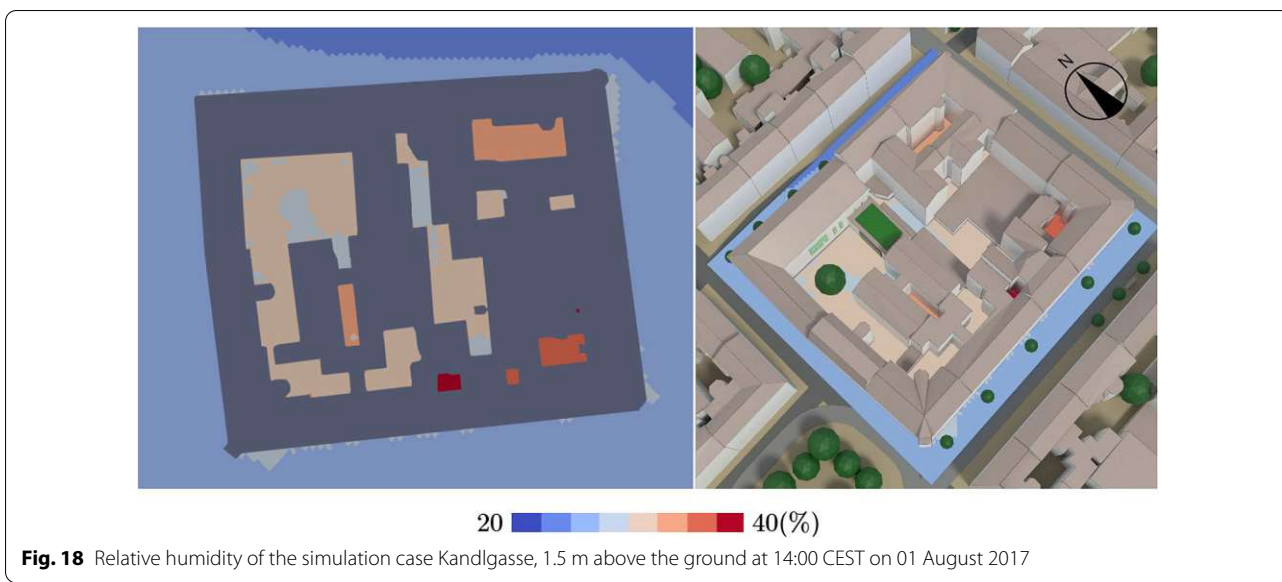
those areas where the maximum values of the apparent temperature are to be expected.

Discussion

For a better understanding of the validity of the above presented simulation results, they are compared to similar studies. In a study of Antoniou et al. (2019) CFD simulations of urban microclimate are performed for a dense highly heterogeneous district in Nicosia, Cyprus and validated using a high-resolution dataset of on-site measurements of air temperature, wind speed and surface temperature conducted for the same district area. The CFD simulations are performed based on the 3D

Unsteady Reynolds-Averaged Navier–Stokes (URANS) equations and the simulated period covers four consecutive days in July 2010. It is shown that the CFD simulations can predict air temperatures with an average absolute difference of 1.35 °C, wind speed with an average absolute difference of 0.57 m/s and surface temperatures with an average absolute difference of 2.31 °C.

A case study of Maiullari et al. (2018) uses a coupling approach that links the simulation tools ENVI-met and City Energy Analyst. The comparison of the air temperature from the weather station and average air temperature from ENVI-met around the buildings of an urban re-development project in the city of Zurich, Switzerland,



shows a maximum deviation of 2.5 °C mainly during the night for a cool day and of 3 °C at 11 o'clock in the morning for a hot day.

Another study of Natanian et al. (2019) couples ENVI-met and EnergyPlus to bring together energy and micro-climatic modeling for a synergistic assessment at the block scale in the climatic context of Tel Aviv. A comparison of the daily resultant air temperature recorded for three different weather files (EnergyPlus, Urban Weather Generator (UWG) and ENVI-met) for the 26th of July recorded for the highest density scenario for three different typologies (courtyard, scatter and high-rise) shows a

night-time air temperature increase of up to 1.5 °C within the UWG file compared to the rural EnergyPlus file. The ENVI-met file recorded a higher night-time temperature increase of up to 3 °C but also a day-time temperature drop of up to 1.5 °C.

In a work of Diz-Mellado et al. (2021) the applicability of a supervised Machine Learning (ML) model as a suitable tool for predicting microclimatic performance inside courtyards has been evaluated. For this purpose, among the ML models developed as supervised learning, Support Vector Machines were selected. The final results for two selected validation cases located in the South of

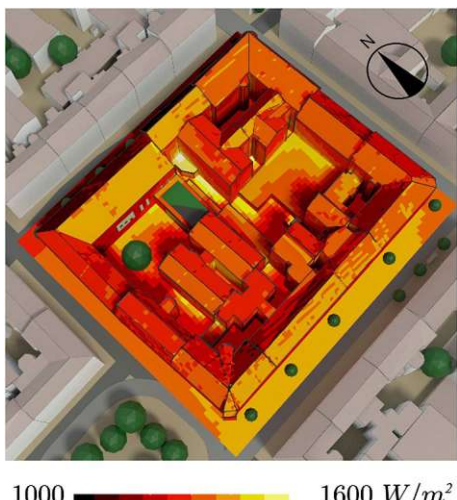


Fig. 20 Incident surface radiation (W/m^2) of the simulation case Kandlgasse at 14:00 CEST on 01 August 2017

Spain showed that, when the day-time slot with the highest urban overheating is considered, the relative error is almost below 0.05% and the Root Mean Square Error (RMSE) is around 1 °C.

Compared to the studies mentioned above, good results (equal to or better than established methods) are obtained with an absolute error between measurement and simulation of ± 2 °C for the validation case Kandlgasse presented in this work, despite the simplifications proposed. Another validation case in the area of Gablenzgasse in Vienna is currently in progress—first simulation results are included in the Additional file 1: Appendix E.

While in the validation case Kandlgasse the sensors were placed relatively close to each other (a few meters) and their transient response was monitored, the validation case Gablenzgasse used distributed measurement locations (spaced tens to hundreds of meters apart) at different fixed points in time. Employing a statistical analysis of the two validation cases, the transient response quality (how well does the simulation result follow measured values) and the spatial response quality (how well does the simulation result fit at different locations) of uhiSolver can be separated from each other. Statistical results and raw data of both validation cases are included in the Additional file 1: Appendix D.

Statistical analysis of correlation coefficients and standard deviations of temperatures shows:

- The transient validation case Kandlgasse is highly correlated to measurement data. Within a 24-h period the standard deviation of temperature differences (simulated to measured) is 0.99 °C.

- The spatially distributed validation case Gablenzgasse shows low deviations of simulated temperatures compared to measured temperatures. The standard deviation of temperature differences (simulated to measured) is 0.93 °C.
- Spatial and temporal standard deviations of temperature differences are both below 1.00 °C.
- uhiSolver shows relatively high spatial and temporal accuracy for temperature predictions. Absolute accuracy (defined via standard deviation) is within 1.00 °C for both validation cases. Relative thermal accuracy is in the range of 10% for hot, cloudless days when compared to a daily thermal variation of 10 °C. 10% accuracy is often considered to be sufficient when used as an engineering tool in the design phase.

More detailed field measurements will be conducted as part of another research program to provide sufficient data for the next validation study. However, further validation of the uhiSolver software also by comparing the simulation results with those of other microclimate simulation tools is needed to substantiate the accuracy of this model using simplified material data for building components and ground surfaces.

Conclusions

The five most relevant building types and ground surfaces in Vienna are investigated. By means of error weighting and sensitivity analysis, it is determined which parameters are essential in each case and which can be neglected. Finally, the defined building types and ground surfaces are reduced in their inhomogeneous material properties to such an extent that they can be represented as a homogeneous monolith with a known margin of error in the computer model.

Considering the defined error tolerance of 5%, it does appear that the stairs can be neglected in all building types due to their low mass share in the total mass. The doors can also be neglected in the mass determination of the interior walls. However, the influence of window surfaces on the surface and interior temperature is significant, since the windows, taking into account shading devices, lead to a reduction in the overall albedo compared to a purely white façade. This results in a higher heat absorption and thus a higher total heat input.

Taking the defined boundary conditions into account, one-dimensional model calculations are carried out for only two time steps in order to derive a tendency for the different parameters and relationships (this forms the algorithmic basis for the transient simulations presented in part two). It is shown that the surface temperatures are related to numerous factors, since the mutual dependence (irradiation and radiation as well as heat

conduction and storage) is complex. Therefore, more accurate forecasts can only be made with dynamic calculations (as in uhiSolver), taking into account a complete physical coupling of all effects: heat conduction, radiation, solar path, airflow and evaporation.

The Dynamic 3D simulations carried out in part two of this study confirm that the simplifying assumption of homogeneous material data for building bodies provides very good results for the investigated validation case of the school GRG 7 Kandlgasse in Vienna.

The simulations carried out also show that the apparent temperature in the greened inner courtyard of the school is sometimes perceived higher than in the adjacent streets, despite the lower air temperature. The reasons for this are the higher radiation density due to the mutual irradiation of the courtyard façades, the lower air velocities and the higher air humidity compared to conditions outside the courtyard.

In the coming years, the demand for a tool that can significantly reduce the extent of the influence of urban structure, the building materials used and the surfaces on urban heat islands in the planning phase will steadily increase. The reasons for this are increasing urbanization and global warming. The simulation software uhiSolver is such a planning tool and is able to help understand the interaction between urban microclimates and the buildings.

Abbreviations

AT: Apparent temperature; CEST: Central European Summer Time; CFD: Computational fluid dynamics; CFL number: Courant–Friedrichs–Lowy number; FFG: Austrian Research Promotion Agency; fvDOM: Finite volume discrete ordinates method; GRG: Secondary school type in Austria; HTM: Human thermal model; IR: Infrared; LOD: Level of detail; max: Maximum; PET: Physiologically equivalent temperature; PMV: Predicted mean vote; PPD: Predicted percentage of dissatisfied; RH: Relative humidity; UHI: Urban Heat Islands; UTCI: Universal Thermal Climate Index; UWG: Urban weather generator; WBGT: Wet bulb globe temperature.

Supplementary Information

The online version contains supplementary material available at <https://doi.org/10.1186/s13717-021-00336-y>.

Additional file 1. Appendix.

Acknowledgements

This research was supported by the Austrian Research Promotion Agency (FFG) within the framework of the General Programme funding line as well as by the Federal Ministry for Climate Action, Environment, Energy, Mobility, Innovation and Technology (BMK) within the Cities of the Future funding line.

Authors' contributions

FT: conceptualization, writing—original draft preparation, project administration. CMB: methodology, investigation, resources, data curation, visualization. AH and ML: software, validation, visualization, funding acquisition. AK: formal analysis, writing—review and editing, supervision. All authors read and approved the final manuscript.

Funding

This research was funded by Österreichische Forschungsförderungsgesellschaft FFG—feasibility study, Grant number 873045.

Availability of data and materials

The data that support the findings of this study are available from Rheologic GmbH but restrictions apply to the availability of these data, which were used under license for the current study, and so are not publicly available. Data are however available from the authors upon reasonable request and with permission of Rheologic GmbH.

Declarations

Ethics approval and consent to participate

Not applicable.

Consent for publication

Not applicable.

Competing interests

The authors declare that they have no competing interests.

Author details

¹Vienna University of Technology, Vienna, Austria. ²Rheologic GmbH, Vienna, Austria.

Received: 10 March 2021 Accepted: 3 October 2021

Published online: 29 October 2021

References

- Ahne V (2014) Alte Steinstiegen auf dem Prüfstand. Die Presse, Wien Ansys. <https://www.ansys.com/>
- Antoniou N, Montazeri H, Neophytou M, Blocken B (2019) CFD simulation of urban microclimate: validation using high-resolution field measurements. Sci Total Environ 695:133743. <https://doi.org/10.1016/j.scitotenv.2019.133743>
- Ausführungsplan (2015) Wien: atelier kaindl + kuntrner gmbh
- Austrian Standards Institute (2008) "ÖNORM EN ISO 13786: thermal performance of building components—dynamic thermal characteristics—calculation methods
- B. of M. Commonwealth of Australia (2010) Thermal Comfort observations. http://www.bom.gov.au/info/thermal_stress/ (accessed Sep. 03, 2020)
- Baumgartner CM (2019) Influence of different construction methods and soil types on the Urban Heat Island-Effect. Vienna University of Technology
- Cid K, Vianna S (2016) A comparative study between thermal radiation models P-1 and discrete ordinates using Cfd software openfoam. In: Congresso Brasileiro de Fluidodinâmica Computacional, I: 1–5. <https://doi.org/10.17648/cbcfd-44247>
- Clauer C (2014) Einführung in die Geophysik—Globale physikalische Felder und Prozesse in der Erde. Springer Spektrum, Berlin
- Coelho PJ, Gonçalves JM, Carvalho MG, Trivic DN (1998) Modelling of radiative heat transfer in enclosures with obstacles. Int J Heat Mass Transf 41(4–5):745–756. [https://doi.org/10.1016/S0017-9310\(97\)00158-0](https://doi.org/10.1016/S0017-9310(97)00158-0)
- Diz-Mellado E, Rubino S, Fern S, Macarena G (2021) Applied machine learning algorithms for courtyards thermal patterns accurate prediction. Mathematics 9(10):1142. <https://doi.org/10.3390/math9101142>
- ENVI_MET Decoding urban nature. <https://www.envi-met.com/de/>
- ENVI-met Model Architecture (2019). <http://envi-met.info/> (accessed Sep. 23, 2020)
- FFG IS5k, Final report, Nr. 849231, project 'vmSol', Rheologic GmbH and TU Vienna, 20.10.2015, internal communication
- Fischer M, Heinz-Martin F, Hanns H, Peter H, Martin J, Richard R, Ekkehard S (2008) Lehrbuch der Bauphysik, 6th edn. Vieweg Teubner Verlag GWV Fachverlage GmbH, Wiesbaden
- Gameiro da Silva MC (2013) Spreadsheets for the calculation of thermal comfort indices. Scribd. <https://doi.org/10.1073/pnas.1017993108>
- GREENPASS Software. <https://greenpass.io/software/>

- Hollands J, Tudiwer D, Korjenic A, Bretschneider BB (2018) Greening Aspang—Messtechnische Untersuchungen zur ganzheitlichen Betrachtung mikroklimatischer Wechselwirkungen in einem Straßenzug einer urbanen Hitzinsel. *Bauphysik* 40(3):105–119. <https://doi.org/10.1002/bapi.201810014>
- Holopainen R (2012) A human thermal model for improved thermal comfort. Doctor of Science in Technology Thesis, Aalto University, VTT
- Honjo T (2009) Thermal comfort in outdoor environment. *Glob Environ Res* 13:43–47
- Huttner S, Bruse M (2009) Numerical modeling of the urban climate—a preview on ENVI-MET 4.0. Seventh Int Conf Urban Clim 4
- Ismail KAR, Salinas CT (2004) Accurate computing of radiative source term using discrete ordinates methods for to use in CFD codes. Conference: Fourth European Thermal Sciences 1:110–119
- Jendritzky G, Maarouf A, Staiger H (2001) Looking for a universal thermal climate index UTCI for outdoor applications. Paper presented at the Windsor-Conference on Thermal Standards
- Knaus H, Schneider R, Han X, Strohle J, Schnell U, Hein KRG (1999) Comparison of different radiative heat transfer models and their applicability to coal-fired utility boiler simulations. 4th International Conference on Technologies and Combustion for a Clean Environment. <http://elib.uni-stuttgart.de/opus/volltexte/1999/277/>
- Korjenic A, et al (2018) GrünPlusSchule@Ballungszentrum Hocheffiziente Fassaden- und Dachbegrünung mit Photovoltaik Kombination; optimale Lösung für die Energieeffizienz in gesamtökologischer Betrachtung. Endbericht, Stadt der Zukunft, FFG/BMVIT, Wien
- Korjenic A, et al (2020) GRÜNEZUKUNFTSCHULEN - Grüne Schuloasen im Neubau. Fokus Planungsprozess und Bestandsgebäude. Endbericht; FFG; Wien
- Ladybug. <https://www.ladybug.tools/ladybug.html>
- Maiullari D, Mosteiro-Romero M, Pijpers-Van Esch M (2018) Urban microclimate and energy performance: an integrated simulation method. 34th International Conference on Passive and Low Energy Architecture (PLEA) - Smart Healthy Within the Two-Degree Limit 1:384–389
- Mitterböck M, Korjenic A (2017) Analysis for improving the passive cooling of building's surroundings through the creation of green spaces in the urban built-up area. *Energy Build* 148:166–181
- Mould ST (2019) The solarLoad Radiation Model. dtx-colab.pt
- Mu D, Gao N, Zhu T (2018) CFD investigation on the effects of wind and thermal wall-flow on pollutant transmission in a high-rise building. *Build Environ* 137:185–197
- Mursch-Radlgruber E, Trimmel H, Gerersdorfer T (2009) Räumliche Differenzierung der mikroklimatischen Eigenschaften von Wiener Stadtstrukturen und Anpassungsmaßnahmen. Ergebnisse kleinklimatischer Messungen. Teil 2 der Studie Räumlich und zeitlich hoch aufgelöste Temperaturszenarien für Wien und ausgewählte. Wiener Umweltschutzbteilung (MA 22), EU-Strategie und Wirtschaftsentwicklung (MA 27)
- Natanian J, Maiullari D, Yezioro A, Auer T (2019) Synergetic urban microclimate and energy simulation parametric workflow. *J Phys Conf Ser* 1343:012006. <https://doi.org/10.1088/1742-6596/1343/1/012006>
- Pecka A (2014) Finite Volume Method for Radiative Heat Transfer Problems. University of West Bohemia
- Sá da Costa PP (2016) Validation of a mathematical model for the simulation of loss of coolant accidents in nuclear power plants. Técnico Lisboa
- Schmid E, Pröll T (2020) Umwelt- und Bioressourcenmanagement für eine nachhaltige Zukunftsgestaltung. Springer Spektrum, Berlin
- Steadman RG (1994) Norms of apparent temperature in Australia. *Aust Met Mag* 43:1–16
- Technische Universität Wien and Universität für Bodenkultur Wien (2018) Forschungsbericht Vegetationstechnisches und bauphysikalisch Monitoring des 'Vertikalen Gartens' der MA31 in der Grabnergasse 4-6, 1060 Wien, Wien
- Terjung WH, O'Rourke PA (1980) Simulating the causal elements of urban heat islands. *Boundary-Layer Meteorol* 19(1):93–118. <https://doi.org/10.1007/BF00120313>
- Toparlar Y, Blocken B, Vos P, van Heijst GJF, Janssen WD, van Hooff T, Montazeri H, Timmermans HJP (2015) CFD simulation and validation of urban microclimate: a case study for Bergpolder Zuid, Rotterdam. *Build Environ* 83:79–90. <https://doi.org/10.1016/j.buildenv.2014.08.004>
- Toparlar Y, Blocken B, Maiheu B, van Heijst GJF (2017) A review on the CFD analysis of urban microclimate. *Renew Sustain Energy Rev* 80:1613–1640. <https://doi.org/10.1016/j.rser.2017.05.248>
- United Nations Department of Economic and Social Affairs (2019) World Urbanization Prospects 2018: Highlights. <https://population.un.org/wup/>
- Urban Weather Generator 4.1 urban heat island effect modeling software. <http://urbanmicroclimate.scripts.mit.edu/uwg.php>
- Zentralanstalt für Meteorologie und Geodynamik (2002) Klimadaten von Österreich 1971–2000. http://www.zamg.ac.at/fix/klima/oe71-00/klima2000/klimadaten_oesterreich_1971_frame1.htm (accessed Aug. 07, 2020)

Publisher's Note

Springer Nature remains neutral with regard to jurisdictional claims in published maps and institutional affiliations.

Submit your manuscript to a SpringerOpen® journal and benefit from:

- Convenient online submission
- Rigorous peer review
- Open access: articles freely available online
- High visibility within the field
- Retaining the copyright to your article

Submit your next manuscript at ► springeropen.com

8.2 Zweite Publikation

Status	Veröffentlicht am 12. Oktober 2022
Original Titel (Englisch)	The Impact of Small-Scale Greening on the Local Microclimate—A Case Study at Two School Buildings in Vienna
Titel (Deutsch)	Die Auswirkung von Begrünungsmaßnahmen kleinen Maßstabs auf das lokale Mikroklima - eine Fallstudie an zwei Schulgebäuden in Wien
Autor:innen	Florian Teichmann, Andras Horvath, Markus Luisser, Azra Korjenic
ISBN/ISSN	ISSN: 2071-1050 DOI: 10.3390/su142013089
Sprache	Englisch
Schlagwörter	building greenery; living walls; urban heat island (UHI) mitigation; urban microclimate; CFD simulation; apparent temperature
Quelle	<i>Sustainability</i> , Vol. 14, Issue 20, Artikel 13089 (2022), Collection: Urban Green Infrastructure for Climate-Proof and Healthy Cities, MDPI [Peer Reviewed Journal]



Article

The Impact of Small-Scale Greening on the Local Microclimate—A Case Study at Two School Buildings in Vienna

Florian Teichmann ^{1,*}, Andras Horvath ^{2,*}, Markus Luisser ² and Azra Korjenic ¹¹ Institute of Material Technology, Building Physics and Building Ecology, TU Wien, 1040 Vienna, Austria² Rheologic GmbH, 1060 Vienna, Austria

* Correspondence: florian.teichmann@tuwien.ac.at (F.T.); andras.horvath@rheologic.at (A.H.)

Abstract: Strategies to mitigate urban heat islands are a recent issue in the Austrian capital, Vienna. In this study, the uhiSolver-v2106-0.21 software was used to evaluate the summer cooling effects and humidity production of small-scale facade greening and a green pergola located in two schools within the city. Based on on-site measurement data, the study revealed that small-scale greening measures are not able to substantially reduce ambient air temperature. On a hot summer day, at 3 p.m. local time (CEST), the maximum decrease amounted to 0.3 °C at 0.1 m from the facade greening as well as inside the green pergola. As for the apparent (perceived) temperature, a reduction of up to 4 °C was observed under the green pergola compared to the unshaded roof terrace. Hence, the simulation results show that, within urban areas, a significant improvement of thermal comfort in summer can only be achieved through large-scale greenery that provides shade for pedestrians.

Keywords: building greenery; living walls; urban heat island (UHI) mitigation; urban microclimate; CFD simulation; apparent temperature



Citation: Teichmann, F.; Horvath, A.; Luisser, M.; Korjenic, A. The Impact of Small-Scale Greening on the Local Microclimate—A Case Study at Two School Buildings in Vienna.

Sustainability **2022**, *14*, 13089.
<https://doi.org/10.3390/su142013089>

Academic Editors: Umberto Berardi and Fausto Cavallaro

Received: 1 July 2022

Accepted: 7 October 2022

Published: 12 October 2022

Publisher's Note: MDPI stays neutral with regard to jurisdictional claims in published maps and institutional affiliations.



Copyright: © 2022 by the authors. Licensee MDPI, Basel, Switzerland. This article is an open access article distributed under the terms and conditions of the Creative Commons Attribution (CC BY) license (<https://creativecommons.org/licenses/by/4.0/>).

1. Introduction

Climate change, increasing urbanization, and re-densification in inner-city areas require new ways and solutions to increase the quality of life and living comfort in urban structures. Urban areas and agglomerations cause temperature increases due to the high percentage of sealed surfaces and the evaporation being reduced, while at the same time solar radiation is stored on building and street surfaces [1]. This leads to the formation of urban heat islands (UHI), where temperatures can sometimes be considerably higher than in surrounding areas. Summer heat leads to reduced quality of life and well-being of the population and can even lead to health consequences, especially for vulnerable population groups, such as old or sick people, as well as children. In the future—due to further increases in average temperatures and increased occurrence of extreme events, such as heat, floods, and drought—the urban system will need to gain resilience to ensure the quality of life of its inhabitants [2]. Against the background of climate change, the urban (micro-)climate is to be regarded as particularly sensitive and susceptible to disturbances. Due to the special spatial situation in cities with many sealed surfaces, a high density of building masses, and a strong heat production as a result of concentrated anthropogenic uses, it is necessary to pay special attention to measures that counteract UHI and other negative effects.

Proposed UHI mitigation strategies are cool pavements or roofs (with light-colored or permeable surfacing) and the increased use of vegetation [3]. While greening in the form of new urban parks is increasingly unlikely in a densely built city, buildings often provide large vacant areas which are extremely valuable for vertical and horizontal greening, with the area available for green walls being about twice that for green roofs [4]. The benefits of vertical greenery systems are covered extensively in the literature [5–11] and include mitigating the UHI effect [12], increasing outdoor thermal comfort [13], reducing noise [14],

eliminating pollutants [15], reducing building energy demand [16,17], increasing urban biodiversity [18], and other social and economic aspects [19].

1.1. Previous Research Projects on the Influence of Building Greenery Systems

The influence of vertical greenery systems on the microclimate within the inner courtyard of the BRG7 school in Kandlgasse, Vienna, was already investigated in the research project GrünPlusSchule (GreenPlusSchool). The cooling capacity of a living wall due to evapotranspiration, as well as the effect on the surface temperature of the outer facade due to shading by the vertical greenery system, were determined [20]. A computational fluid dynamics (CFD) simulation with the uhiSolver software was used to show the influence of the greening measures. These included two small-scale living walls, direct and indirect green facades, as well as a tree and some shrubs. The simulation results indicated that the influence on the air temperature in the inner courtyard of the school could be neglected [21]. Furthermore, it was found that due to the locally higher irradiance caused by reflections on the building facades, the lower air velocities, and the consequently higher air humidity, the apparent (perceived) temperature in the inner courtyard was in some locations higher than in the adjacent street canyons, despite the lower air temperature.

A recent study by Daemei et al. from 2021 investigated the thermal performance of a green facade compared to a bare wall on the north facade of a two-storey residential building in the humid climate of Rasht during summertime [22]. Using the ENVI-met software to evaluate the effect of the green facade on the surrounding air, it is stated that the temperature in front of the green facade is only insignificantly lower than in front of the bare wall. The peak temperate reduction within the ENVI-met simulation was 0.36 °C at 12 p.m.

Fahed et al. also used the ENVI-met software to conduct simulation studies on different urban heat island mitigation scenarios for the city of Beirut in Lebanon [23]. A reduction in air temperature during the day of up to 2 °C was observed when adding 7% of urban vegetation. An even greater reduction in local air temperature with a maximum of 7 °C was obtained at 1:00 p.m. and 1:00 a.m. by the blue scenario based on the implementation of fountains and water sprays. The third scenario, using high albedo materials, led to an increase in the mean radiant temperature, contributing to an additional thermal discomfort for pedestrians. Therefore, a combination of white models with other models is recommended to improve the pedestrian comfort.

Using computational fluid dynamics (CFD) simulations, a maximum temperature reduction of 2 °C within a street canyon in the city center of Arnhem, the Netherlands, was obtained by Gromke et al. when applying vegetation as avenue-trees, green facades, and roof greening at the same time [24]. Green facades only partially contributed to the cooling effect, with a maximum reduction of about 0.3 °C, whereas roof greening did not influence the air temperature inside the canyon at all. Therefore, the most significant reduction in temperature by a single greening measure was achieved with the avenue trees, reducing air temperature by a maximum of 1.6 °C at pedestrian level. In general, the cooling effect was limited to a distance of a few meters from the greening measures.

Another case study by Morakinyo et al. analyzed the thermal benefits of vertical greenery systems, such as living walls, in the high-density city of Hong Kong. Using the ENVI-met software combined with a parametric study, it was shown that 30 to 50% of all facades would need to be greened to potentially reduce air temperature by about 1 °C [25]. To maximize thermal comfort at the pedestrian level, vertical greenery systems should be placed at the base of buildings rather than at tower heights.

Similar results have been obtained by Peng et al. using the ENVI-met software to evaluate the cooling effects of block-scale facade greening with living walls in summer for the city of Nanjing in China [26]. For 30 scenarios with 6 idealized urban block forms and 5 different facade greening ratios, a maximum cooling intensity of 0.96 °C was determined for the high-rise, high-density scenario with a building height of 48 m, a building density of 34.6%, and 100% of the facades covered with living walls.

In the city of Colombo, Sri Lanka, the performance of vertical greenery systems in tropical conditions was evaluated by Galagoda et al. The study included three different types of green infrastructures, namely living walls, indirect green facades, and direct green facades [27]. Compared to a bare wall, the external surface temperature behind the vertical greenery systems was reduced by 8.72 K, 8.69 K, and 5.87 K for living walls, indirect green facades, and direct green facades, respectively. The air temperature, at a distance of 1 m from the vertical greenery systems, was reduced by 0.36 K, 0.61 K, and 0.01 K, respectively.

1.2. Assessing the Impact of Building Greenery Systems on the Local Microclimate

In the research project GRÜNEzukunftSCHULEN (GREENfutureSCHOOLS), two schools in Vienna (BRG16 Schuhmeierplatz and BRG15 Diefenbachgasse) were equipped with living wall systems in interior spaces and on north-facing exterior facades [28]. The living walls were accompanied by hygrothermal, microclimatic, and social measurements. The aim was to provide schools with green infrastructure and integrate it into the teaching and education of pupils. As part of the ongoing research project GRÜNEzukunftSCHULEN² (GREENfutureSCHOOLS²) the influence of the installed green infrastructure on the immediate microclimate in the outdoor areas is being investigated. The aim is to evaluate whether and how the greenery systems affect the sojourn quality in school open spaces. Unlike previous studies that took point measurements of outdoor temperature and air humidity, this project deploys a network of sensors set up on-site to draw conclusions about the spatial impact of greenery systems (two living wall systems and a green pergola).

The measurement data obtained is subsequently compared to a dynamic microclimate simulation using the uhiSolver software, version v2106-0.21 of Rheologic GmbH, Vienna. Compared to the ENVI-met software, which represents a microclimate simulation on a large scale with a horizontal resolution of a few meters [29], uhiSolver simulates the building and its immediate surroundings with a scale down to about 0.3 m. Compared to the ENVI-met simulations, the resolution is several times higher in certain areas. Furthermore, the cell geometry is not limited to right angles, so that deviating surfaces (e.g., roof slopes) and curves (columns, curved structures, etc.) can be mapped much more accurately. This is a particular advantage of the uhiSolver method when it comes to the correct mapping of near-wall flows in microclimate simulations. Hence, it is possible to realistically represent the complex relationships between solar radiation, air currents, the cooling capacity of plants through evaporation, and the heat storage of the surrounding surfaces. This provides the basis for a deeper understanding of the effect of greenery systems on the immediate microclimate close to the building. A detailed description of the functioning and model structure of uhiSolver can be obtained from the article “Simulation of urban microclimate with uhiSolver: software validation using simplified material data” [21]. Two additional validation cases of the Gablenzgasse (summer 2021) and the Naschmarkt area (summer 2022) in Vienna are provided in Appendix C, respectively. The present version of uhiSolver has an absolute deviation in terms of temperature and absolute humidity of 0.09 °C and 0.0042 g_{water}/g_{air} and a standard deviation of ±1.13 °C (3.57%) and ±0.0019 g_{water}/g_{air}, respectively.

The microclimate simulations within the present study, examining small-scale greening measures at the schools BRG16 Schuhmeierplatz and BRG15 Diefenbachgasse in Vienna, are also using the simplified material data described in the aforementioned article. The research goal is to compare experimental data and CFD simulations of local outdoor effects on thermodynamic states (air temperature and absolute humidity), incident radiation, and apparent temperature (AT) of small-scale living walls and a green pergola with climbing vines.

2. Materials and Methods

Within this study, two living walls are investigated, one installed by Optigrün at Diefenbachgasse School, the other one built by Techmetall at Schuhmeierplatz School. The research also includes a green pergola at Schuhmeierplatz School as an example for a

low-tech greenery system. The measurements cover the analysis of air temperature and humidity, as well as wind speed, and are taken at different distances from the greenery systems. The measurement setup is described in Section 2.1. for Diefenbachgasse School and in Section 2.2. for Schuhmeierplatz School. The measurement data obtained directly from the experiments do not serve as a basis for the dynamic microclimate simulations with the uhiSolver software. Instead, external forcing (temperature, humidity, wind-speed) is applied using weather data from publicly available data of a weather station in Vienna's third district. The advantages of simultaneously collecting on-site measurement data and processing an independent microclimate simulation are that the measured data can be used to validate the new software, and that the simulation enables a differentiated processing and evaluation of the effects of the greenery systems on the microclimate (air temperature, relative humidity, radiation density, air currents, perceived temperature, etc.).

For both schools, the assessment is made for an exemplary model day with a clear sky and high outdoor air temperatures. The microclimate simulations presented are limited to the timeframe between 06:20 a.m. to 4:00 p.m. local time (CEST). The visualizations of the influence of the greening measures on the air humidity, air temperature, and apparent (perceived) temperature are conducted at 3:00 p.m. local time (CEST), the hottest time of day, to show the maximum influence. Therefore, nighttime transpiration is not evaluated as, according to Dayer et al., its contribution to the water stress of plants is negligible [30], and no significant impacts of plant's transpiration on air humidity and air temperature are expected for this time of day. However, evaporation of water from the substrates continues throughout the night, depending on local wind conditions, soil saturation, etc.

2.1. School BRG15 Diefenbachgasse

At the school BRG15 Diefenbachgasse, the living wall on the roof terrace, third floor, is the subject of the investigation. The living wall has a height of 2.4 m, a width of 4.9 m, and is mounted on the exterior wall with an air gap of 5 cm. It is equipped with a water tank and a circulation pump. Irrigation is performed twice a day, with a water consumption of 1.22 L/m²d. The plants used are *Geranium macrorrhizum*, *helianthemum* species, phlox species, and heuchera species. A schematic vertical section of the living wall is given in Figure 1. The weather station was attached to a 2 m high stand in the center of the terrace. Six temperature and humidity sensors were connected with cords, extending between the stand and the living wall at a height of 1.6 m. A seventh sensor was placed in the center of the living wall about 0.3 m in front of the planting. All seven sensors were equipped with a radiation shield. In addition, one surface temperature sensor was mounted on the exterior wall directly above the living wall and one was mounted on the concrete slabs on the ground in front of the living wall. The thermocouples used in this study were Rotronic HC2As (material polycarbonate) with an accuracy of $\pm 0.8\%$ RH and $\pm 0.1\text{ K}$ at 10 to 30 °C, recording data every 5 min. The weather station used was a Davis Instruments Vantage Pro2™ (not ventilated), recording the following data every 15 min (the respective accuracies are set in brackets): relative humidity ($\pm 2\%$), rainfall ($\pm 3\%$), rain rate ($\pm 5\%$), solar radiation ($\pm 5\%$), temperature ($\pm 0.3\text{ }^{\circ}\text{C}$), wind direction ($\pm 3^{\circ}$), and wind speed ($\pm 0.9\text{ m/s}$ or $\pm 5\%$). The data logger used was a Driesen + Kern DataCollectorXP-R, with the measurement data being exported once a week. The positions of the sensors are illustrated schematically in Figure 2; the way they were mounted on-site is shown in Figure 3.

From the measurement data collected in summer 2021 at the weather station on the roof terrace of Diefenbachgasse School, a representative model day is selected for the subsequent microclimate simulation, which should represent a summer day with clear skies, peak outdoor air temperatures, and high solar irradiation. The selected day is July 28, which has a slightly lower solar irradiance (see Figure 4), but the highest outdoor air temperature of the entire series of measurements (see Figure 5). The local climate during the study period at the Diefenbachgasse School weather station is displayed in Table 1, which shows average, maximum, and minimum values of air temperature, absolute air humidity, wind velocity, and wind direction.

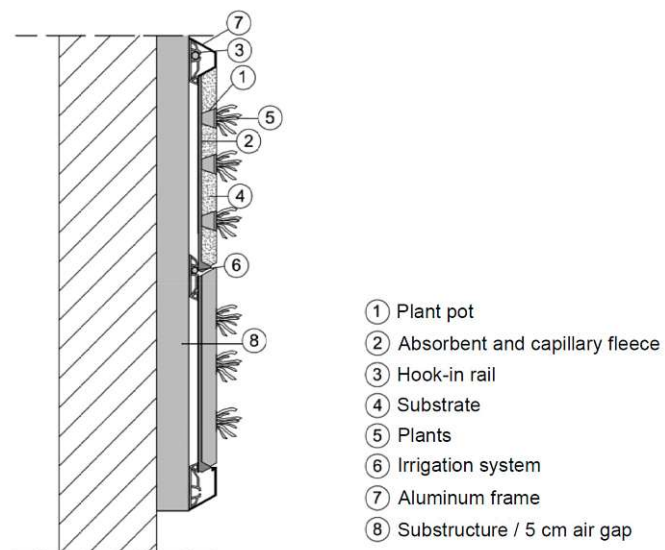


Figure 1. Schematic vertical section [31] of the living wall (cassette system) at Diefenbachgasse School, with the main elements given.

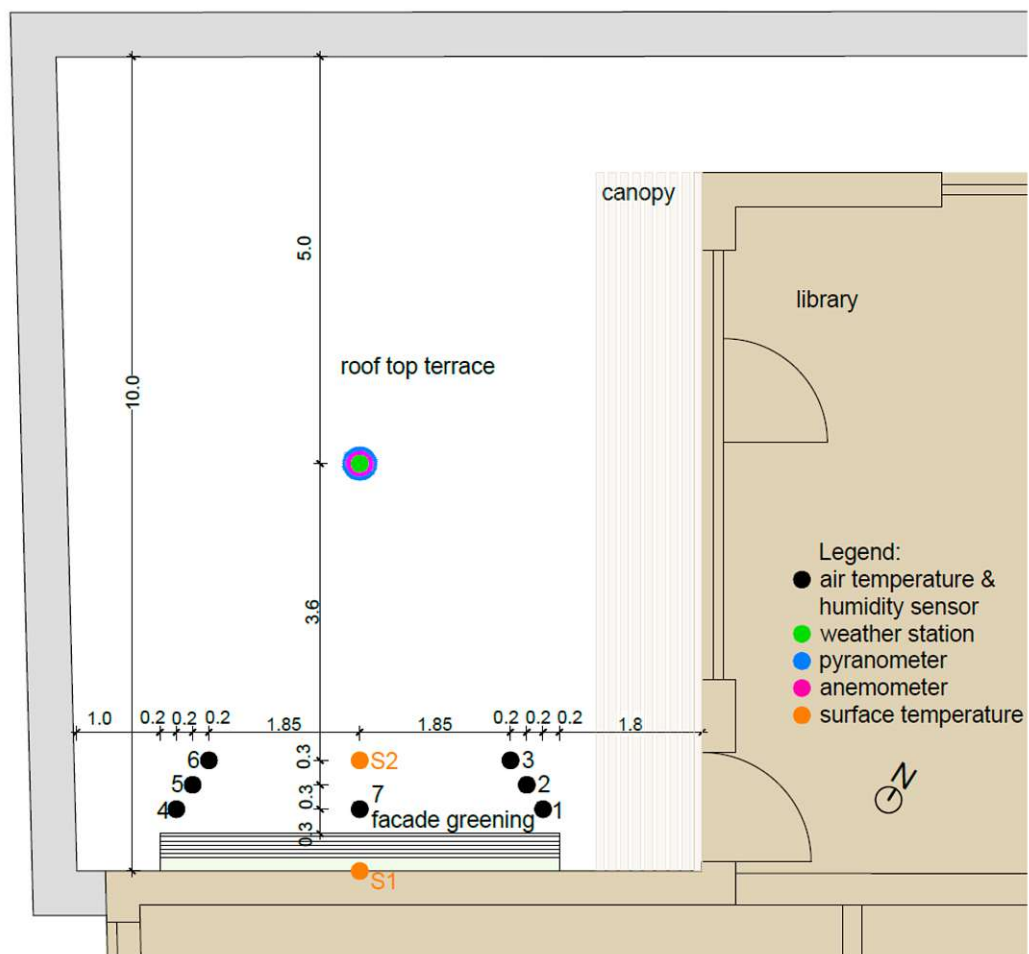


Figure 2. Schematic representation of the positions of the installed sensors at Diefenbachgasse School with the air temperature and humidity sensors 1 to 7 and the surface temperature sensors S1 and S2.



Figure 3. Images of the installation of the sensors at Diefenbachgasse School: (a) position of the weather station; (b) position of the temperature and humidity as well as surface temperature sensors.

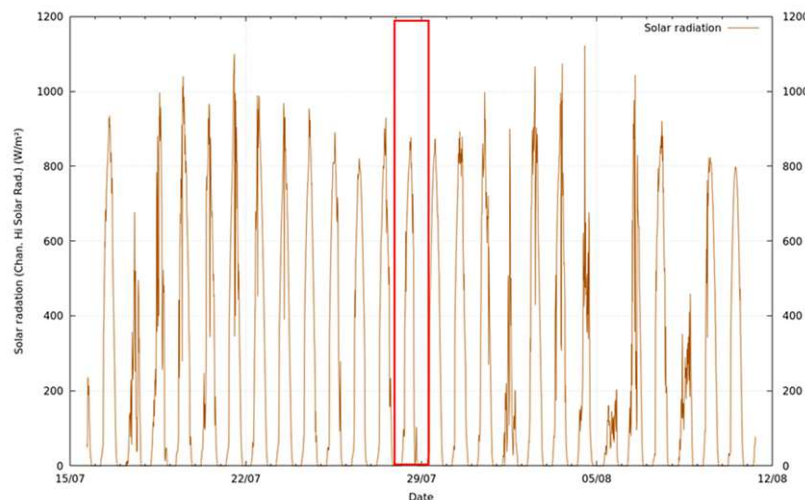


Figure 4. Solar radiation measured by the weather station at Diefenbachgasse School during the entire measurement period in summer 2021, with the selected model day highlighted.

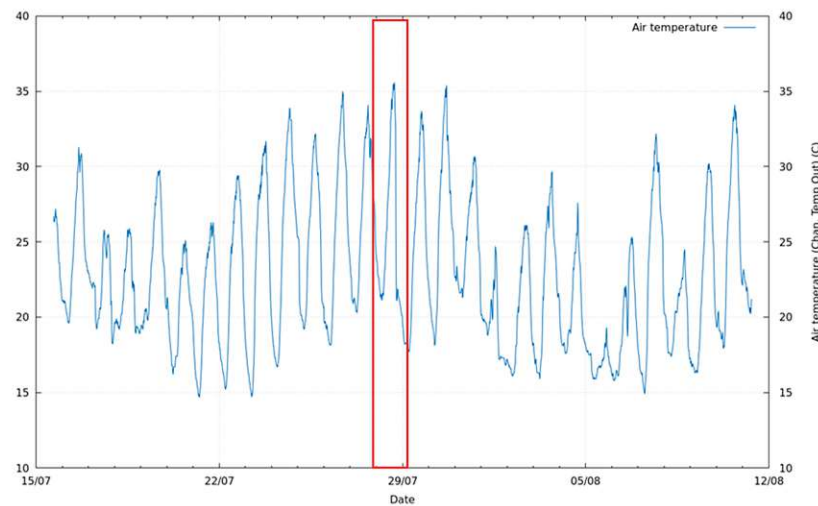


Figure 5. Outdoor air temperature measured by the weather station at Diefenbachgasse School during the entire measurement period in summer 2021, with the selected model day highlighted.

Table 1. Average, maximum, and minimum values of air temperature [T in °C], absolute humidity [X in kg water vapor/kg dry air], wind velocity [U in m/s], wind direction, and total solar irradiance [TSI in W/m²] at the weather station of Diefenbachgasse School on the model day between 6:20 and 16:00 CEST.

	T (°C)	X (kg/kg)	U (m/s)	Wind-Dir. (-)	TSI (W/m ²)
Minimum	21	0.0125	1.6	ESE	25
Average	28	0.0130	3.2	W	436
Maximum	35	0.0135	4.8	WSW	846

2.2. School BRG16 Schuhmeierplatz

At BRG16 Schuhmeierplatz, both the living wall in the inner courtyard and the green pergola on the roof terrace, third floor, were investigated. The L-shaped living wall is mounted on the exterior wall with an air gap of 5 cm. The height varies between 1.75 m and 3 m, and the width varies between 2 m and 8 m. The plants used are *Geranium macrorrhizum*, helianthemum species, and heuchera species. Irrigation is performed twice a day, with a water consumption of 1.22 L/m²d. The green pergola covers an area of 3 m by 7 m and is 2.7 m high. The plants used are *Rubus fruticosus*, *Actinidia arguta*, *fragaria*, *Akebia uinata*, *Thunbergia alata*, *Santolina chamaecyparissus*, *Salvia nemorosa*, *Lavandula angustifolia*, helianthemum, coreopsis, *Tropaeolum majus*, and *Ionicera* species. Irrigation is performed once a day, with a water consumption of 73.5 L/d, and it is carried out via a direct connection to the water pipe and regulated by means of an irrigation computer. A schematic vertical section of the living wall and the green pergola are given in Figure 6. Six temperature and humidity sensors were mounted at different positions in front of the living wall. In addition, three surface temperature sensors were affixed on the exterior wall approximately 2 m above the green façade (see Figure 7). The four temperature and humidity sensors in the pergola were attached to the wooden structure of the pergola in two different positions and at two different heights (see Figure 8). The weather station was again mounted on a 3 m high stand, next to the pergola. In addition, two surface temperature sensors were fixed on the concrete slab of the roof terrace. The thermocouples used at Schuhmeierplatz School were also Rotronic HC2As, recording data every 5 min. The weather station used was a Davis Instruments Vantage Pro2™ Aktiv, recording the same data as at Diefenbach School every 15 min (with the accuracies also being the same). The data logger used was a Keysight DAQ970A, with the measurement data being exported once a week. An overview of the positions of all sensors is provided in Figure 9. All temperature and humidity sensors were equipped with a radiation shield.

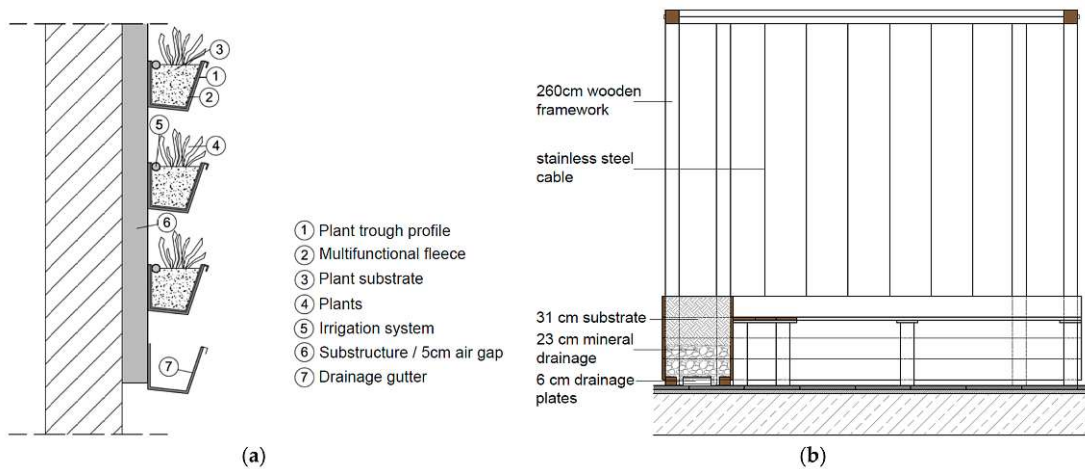


Figure 6. Schematic vertical sections of the greenery systems at Schuhmeierplatz School, with their main elements given: (a) living wall (trough system) [31]; (b) green pergola.



Figure 7. Images of the installed sensors at Schuhmeierplatz School: (a) position of the temperature and humidity sensors in front of the living wall; (b) position of the surface temperature sensors above the living wall, and position of the weather station on the roof terrace.



Figure 8. Images of the installed sensors at the green pergola at Schuhmeierplatz School: (a) position of the temperature and humidity sensors on the left side of the pergola; (b) position of the temperature and humidity sensors on the right side of the pergola.

Due to technical problems with the weather station on the roof terrace of Schuhmeierplatz school, the recorded measurement data are limited to the period of one week in August 2021. As with Diefenbachgasse School, a representative model day with the highest possible outdoor air temperature and consistently high solar radiation was chosen. The selected day is August 14, a day with a peak temperature of 35 °C and a nearly undisturbed solar radiation curve (see Figure 10). The local climate in the examined period at Schuhmeierplatz weather station is displayed in Table 2, showing average, maximum, and minimum values of air temperature, absolute air humidity, wind velocity, and wind direction.

Subsequently, wind simulations and microclimate simulations were carried out for the selected model days of the two schools using the uhiSolver software. For this purpose, weather data from a weather station in the third district of Vienna were used as input data in order to compare the results of the simulation with the measured data collected on-site.

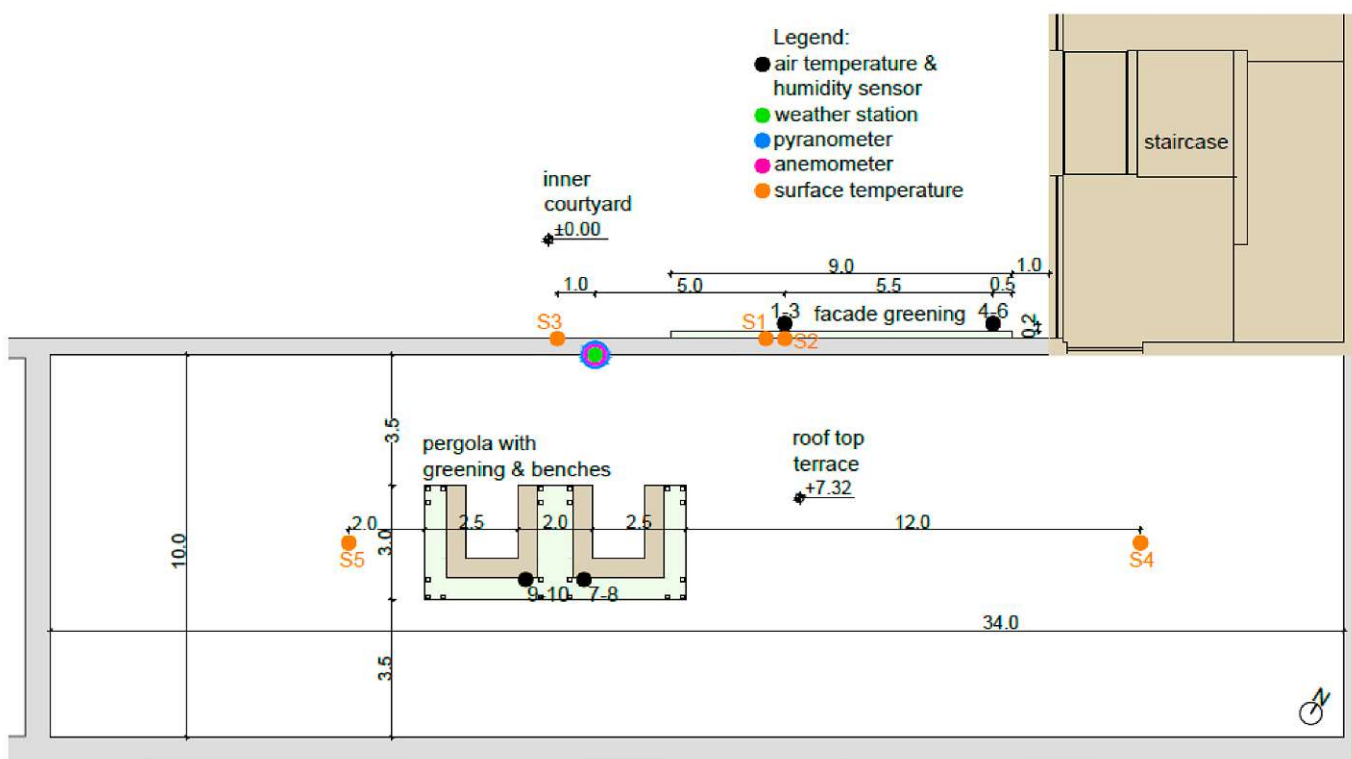


Figure 9. Schematic representation of the positions of the installed sensors at Schuhmeierplatz School with the air temperature and humidity sensors 1 to 10 and the surface temperature sensors S1 to S5.

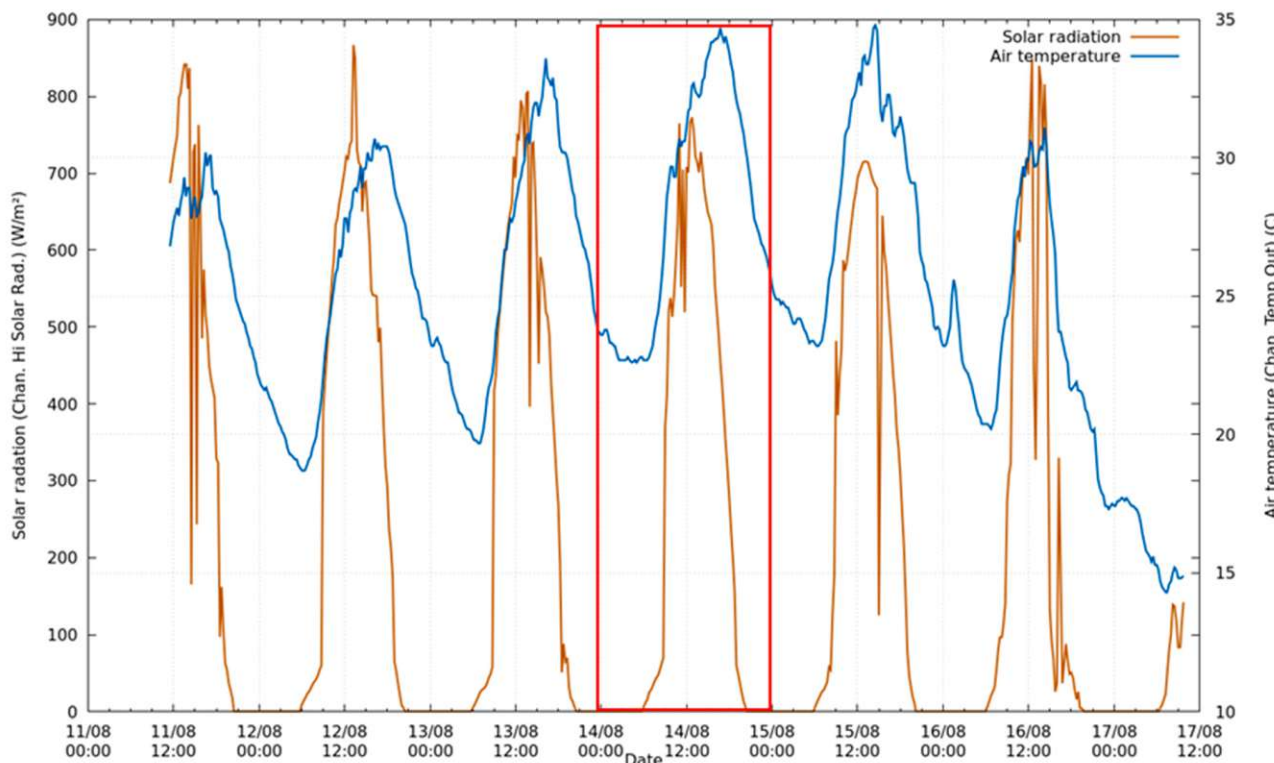


Figure 10. Outdoor air temperature and solar radiation measured by the weather station at Schuhmeierplatz School in August 2021, with the selected model day highlighted.

Table 2. Average, maximum, and minimum values of air temperature [T in °C], absolute humidity [X in kg water vapor/kg dry air], wind velocity [U in m/s], wind direction, and total solar irradiance [TSI in W/m²] at the weather station of Schuhmeierplatz School on the model day between 6:20 and 16:00 CEST.

	T (°C)	X (kg/kg)	U (m/s)	Wind-Dir. (-)	TSI (W/m ²)
Minimum	21.5	0.0120	0	E	0
Average	28.4	0.0128	2.4	ESE	367
Maximum	35.3	0.0135	4.8	WSW	735

3. Results

3.1. School BRG15 Diefenbachgasse

At the beginning, a wind simulation of the area of Diefenbachgasse School was carried out to determine the large-scale wind direction corresponding to the wind conditions on the roof terrace according to the measured data of the weather station. The Y coordinate (yellow arrow) of the coordinate system in Figure 11 points to the north, and the X coordinate (red arrow) to the east. A large-scale wind direction of WSW coincides best with the measured data from the weather station and, thus, was consequently used as a basis for the microclimate simulation. Figure 11b also shows that a wind vortex is formed on the roof terrace. Nevertheless, the wind direction at the weather station corresponds to that in front of the living wall. Thus, the measurement data of the weather station regarding the wind direction can be used for the determination of the wind conditions directly in front of the living wall. As the main large-scale wind direction in Vienna from July to September in the years 2009 to 2019 is west (see Figure 12), the wind conditions of the selected model day with a large-scale wind direction of WSW can be considered representative for the examined period.

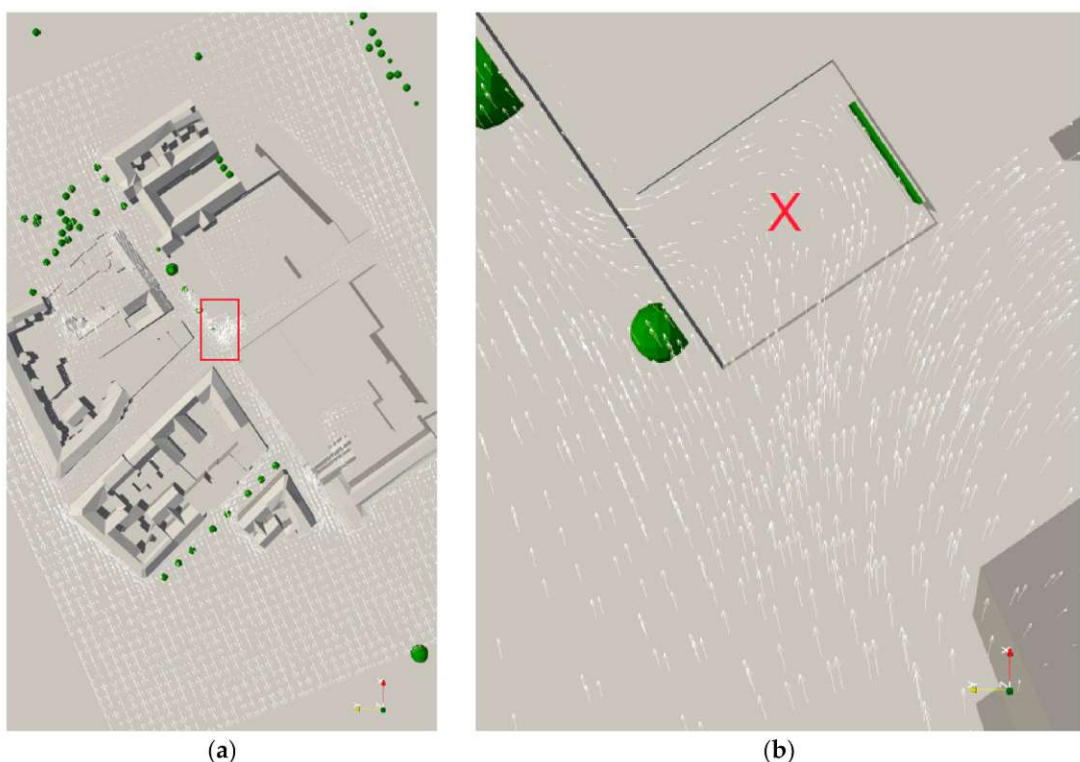


Figure 11. Results of the wind simulation at Diefenbachgasse School: (a) representation of the entire simulation area with the roof terrace highlighted; (b) wind conditions and position of the weather station on the roof terrace.

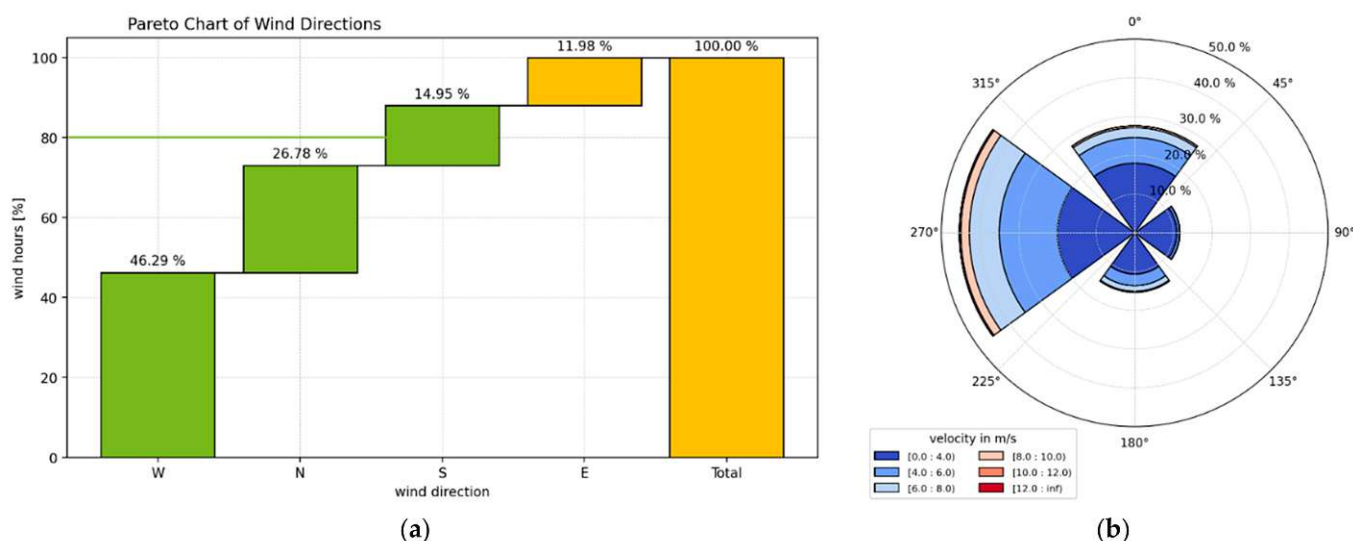


Figure 12. Typical wind conditions in summer (July to September) in Vienna using hourly weather data from 26.8.2009 to 26.8.2019 [32]: (a) pareto chart of wind directions; (b) wind rose diagram of wind velocities in each wind direction.

Based on the results of the wind simulation, the next step was to perform a microclimate simulation for the object area. The simulation results are shown for the hottest time of the day at 3:00 p.m. CEST. The living wall faces north-west and is just about to move out of the shadow of the school building, whereas the roof terrace itself is directly exposed to the sun (see Figure 13).



Figure 13. Shadow cast at Diefenbachgasse School on the model day at 3:00 p.m. CEST, with the roof terrace highlighted.

The results of the microclimate simulation are displayed as colored plots, with each color representing a different value according to the given color table. The evaluations of the humidity load (Figure 14) and the air temperature (Figure 15) on the model day at 3:00 p.m. CEST show that the effect of the living wall on the microclimate is limited to the immediate area in front of the greenery and downwind of the greenery. The moisture produced by the living wall is immediately removed by the wind. The cooling effect due to evapotranspiration of the plants can also be seen directly in front of the facade and

downwind of the living wall. The cool air is then carried away along the facade, with the cooling effect of the greenery gradually blending into that of the shading near the facade as the distance from the greenery increases. The contribution of the living wall to the air temperature reduction on the model day at 3:00 p.m. CEST is limited to 0.3°C at a 0.1 m distance and 0.1°C at a 0.5 m distance from the greening, respectively. At a distance of 1 m from the living wall, no influence on the air temperature can be detected.

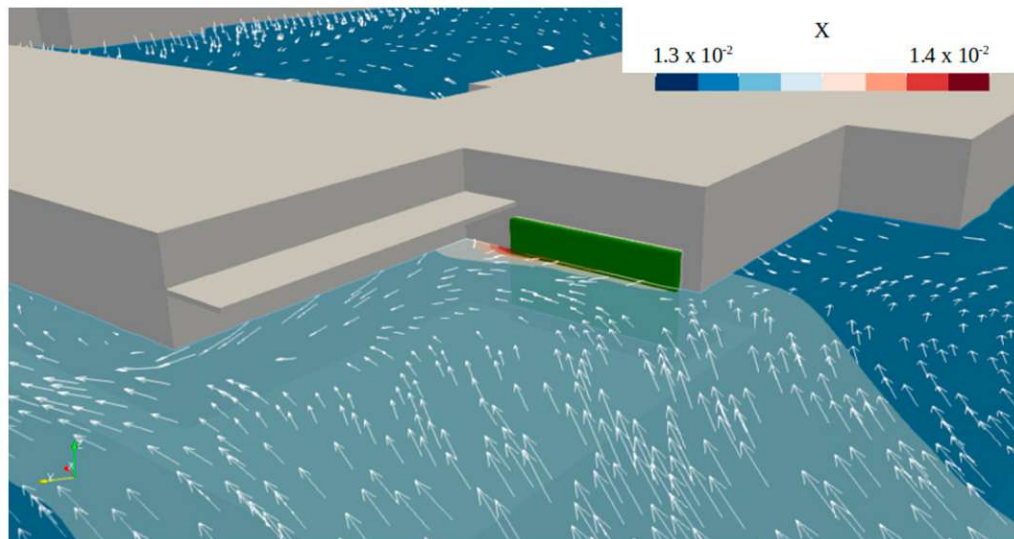


Figure 14. Humidity load (kg/kg) at the level of the Diefenbachgasse School weather station on the model day at 3:00 p.m. CEST.

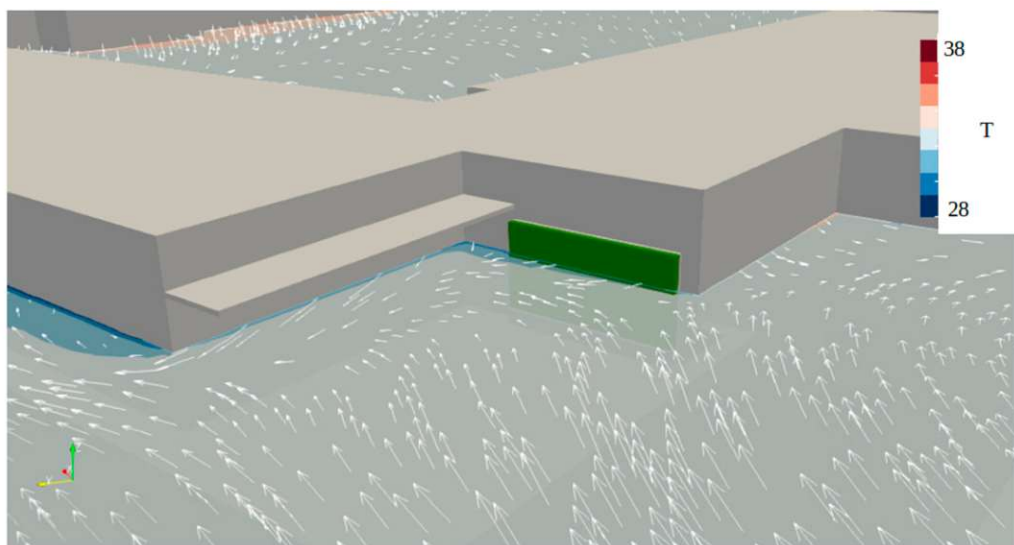


Figure 15. Air temperature ($^{\circ}\text{C}$) at the level of the Diefenbachgasse School weather station on the model day at 3:00 p.m. CEST.

Observing the incident radiation intensity (Figure 16) and the surface temperatures (Figure 17) on the model day at 3:00 p.m. CEST, the following figures clearly show that there is considerable radiation concentration and high surface temperature in some areas. The north-west-oriented living wall can slightly change this unfavorable situation, which is due to the geometry and orientation of the building. It can only be observed that there are no such radiation and surface temperature peaks in the area in front of the living wall.

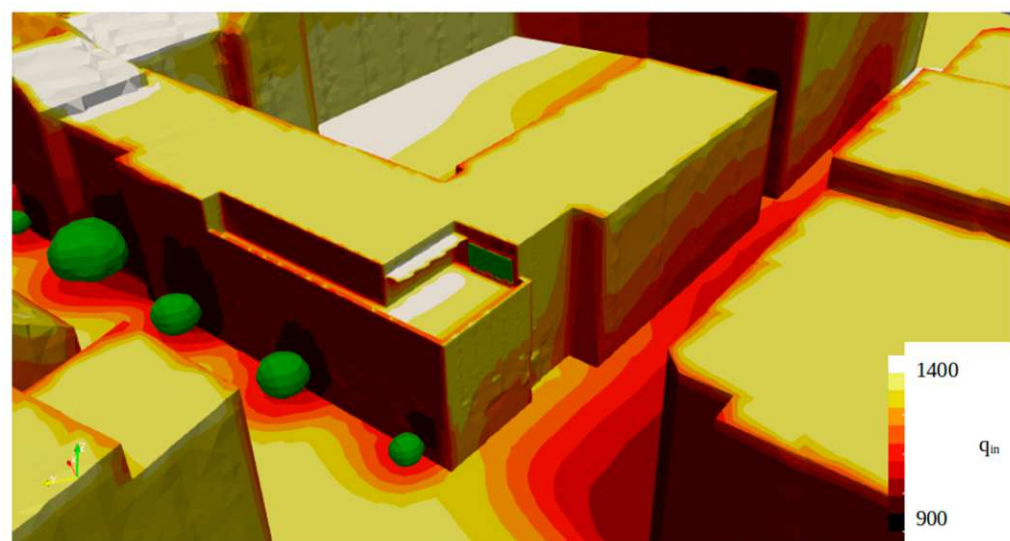


Figure 16. Incident surface radiation intensity (W/m^2) at Diefenbachgasse School on the model day at 3:00 p.m. CEST.

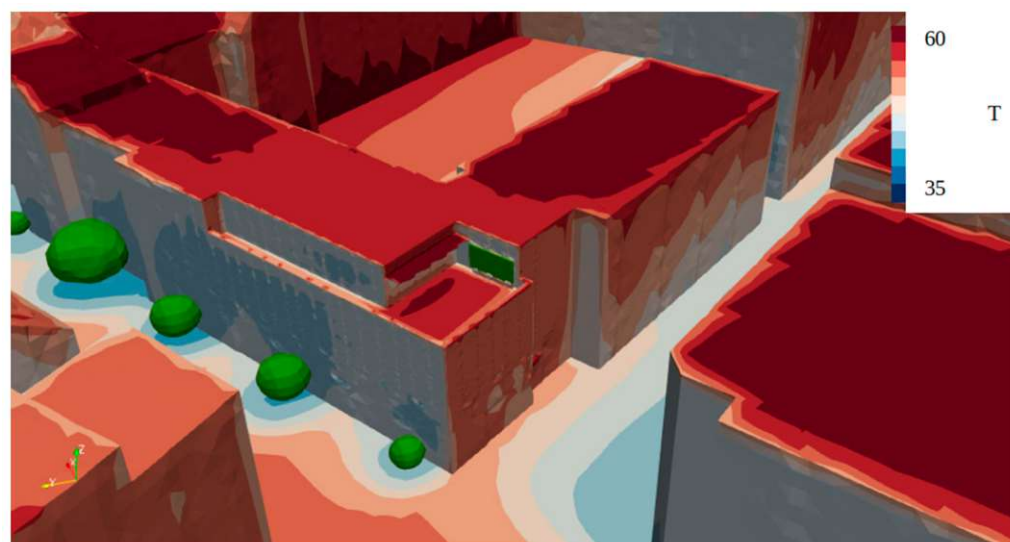


Figure 17. Surface temperatures ($^\circ\text{C}$) at Diefenbachgasse School on the model day at 3:00 p.m. CEST.

The results of the simulation validation by means of the experimental data show an increasing deviation between measured and simulated values in the afternoon hours (see Figure 18) with an average absolute error of $-2.78\text{ }^\circ\text{C}$ and a standard deviation of absolute errors of $1.12\text{ }^\circ\text{C}$ at 3:00 p.m. CEST. This could be due to the use of non-ventilated radiation shields. In the afternoon hours, the air temperature sensors are directly exposed to solar radiation, so the recorded air temperature might be influenced despite the attached radiation shields. Future measurements will use ventilated radiation shields to exclude the influence of solar irradiation on the measurement data. Further information on the validation results is provided in Appendix C.

In the following section, the results of the wind and microclimate simulation of Schuhmeierplatz School are presented.

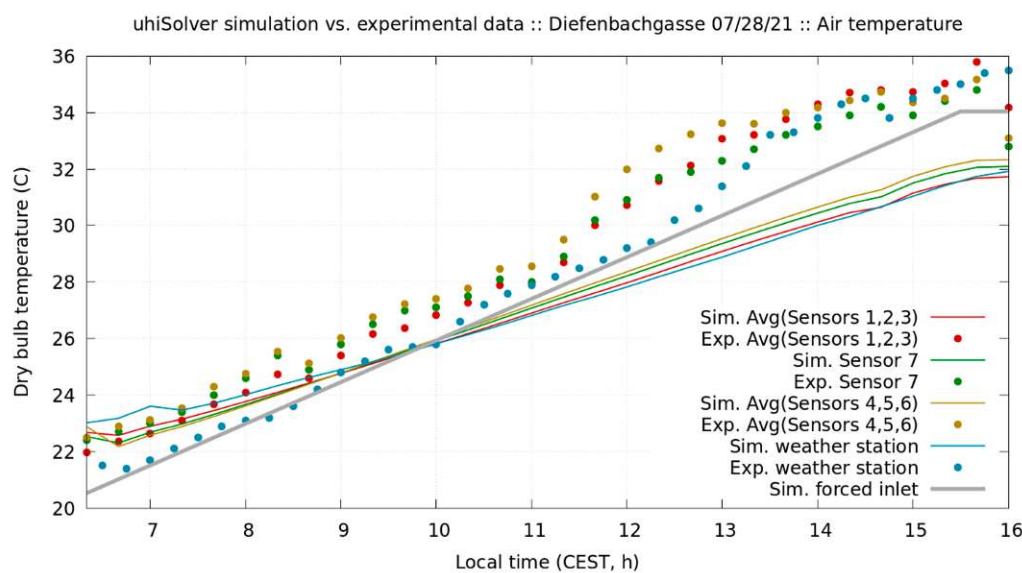


Figure 18. Validation of simulated air temperature with measured data at Diefenbachgasse School on the model day from 06:20 a.m. to 4:00 p.m. CEST.

3.2. School BRG16 Schuhmeierplatz

Several wind simulations were performed at Schuhmeierplatz School in advance to determine the large-scale wind direction in which the resulting wind conditions on the school's roof terrace would match the wind measurement data from the weather station. Of the four wind simulations performed with different large-scale wind directions, the one with westerly wind corresponds most closely to the locally measured wind direction E to ESE at the weather station (see Figure 19). This 180° deviation from the main wind direction is due to the formation of an air vortex at the examined building block. Again, the large-scale wind direction (west) on the selected model day corresponds to the main wind direction of the examined summer period in Vienna (see Figure 12).

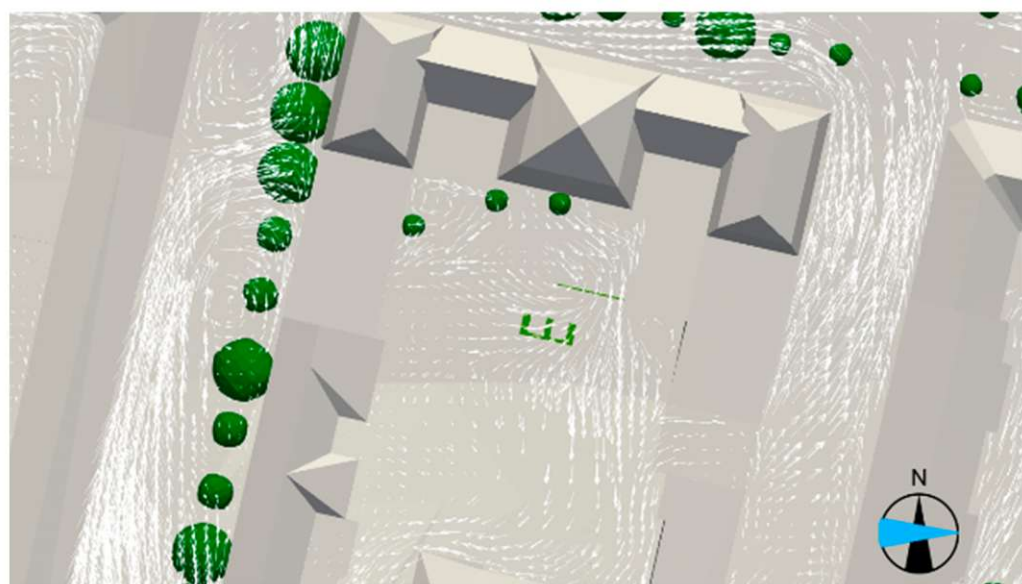


Figure 19. Result of the wind simulation at Schuhmeierplatz School for large-scale westward wind direction, as indicated by the blue arrow.

The simulation results are shown for the hottest time of the day at 3:00 p.m. CEST. The living wall within the inner courtyard faces north and, thus, is in the shadow of the

school building, while the green pergola on the roof terrace is directly exposed to the sun, providing shade only in a very confined area (see Figure 20).



Figure 20. Shadow cast at Schuhmeierplatz School on the model day at 3:00 p.m. CEST, with the position of the greenery systems highlighted.

The microclimate simulation with uhiSolver using the large-scale westward wind direction shows a similar situation in the inner courtyard of Schuhmeierplatz School as on the roof terrace of Diefenbachgasse School, in that the humidity produced by the plants of the living wall is directly carried away by the wind (see Figure 21), resulting in a very limited spatial cooling effect. The increased humidity is, thus, only visible in the immediate vicinity in front of and a few meters downwind of the living wall. With respect to the thermodynamic air temperature in the inner courtyard on the model day at 3:00 p.m. CEST, within the numerical range of variation, no effect of the living wall is detectable in the CFD simulation (see Figure 22). The increased air temperature observed on the short side of the courtyard is due to downward winds along the heated facade.

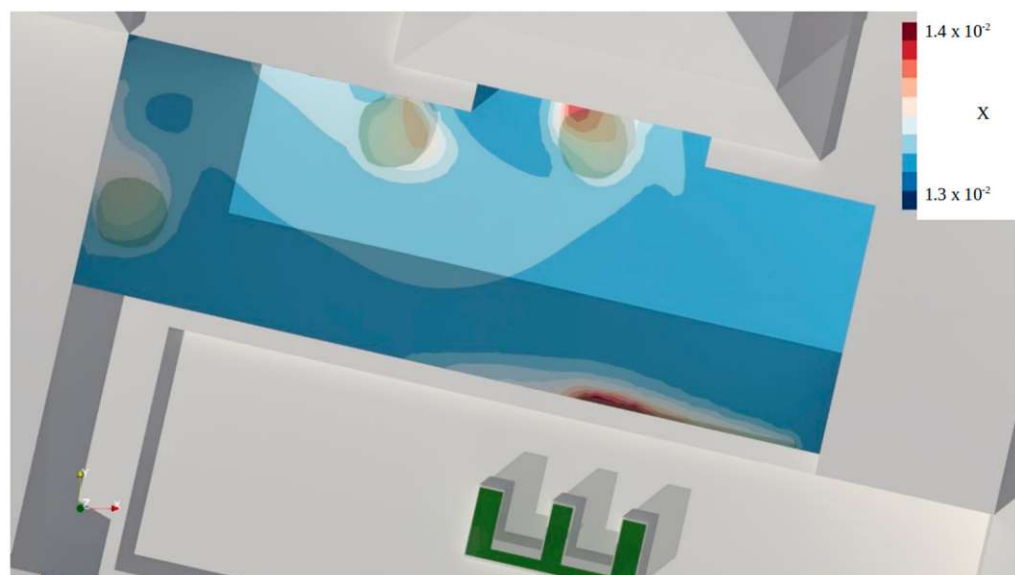


Figure 21. Humidity load (kg/kg) at the level of the Schuhmeierplatz School living wall on the model day at 3:00 p.m. CEST.



Figure 22. Air temperature ($^{\circ}\text{C}$) at the level of the Schuhmeierplatz School living wall on the model day at 3:00 p.m. CEST.

Regarding the green pergola on the roof terrace, similar conclusions can be obtained. Whereas the impact of the plants on the absolute air humidity in the vicinity of the green pergola is significant (Figure 23), the air temperature is in some parts even higher than in the adjacent parts of the roof terrace (Figure 24). This can be attributed to the warming of the leaves themselves and the additional reflections of solar irradiance. The maximum air temperature reduction within the green pergola on the model day at 3:00 p.m. CEST is $0.3\ ^{\circ}\text{C}$, decreasing to $0.1\ ^{\circ}\text{C}$ at about 1 to 3 m distance from the pergola. At a 5 m distance, there is no detectable impact of the green pergola on air temperature.

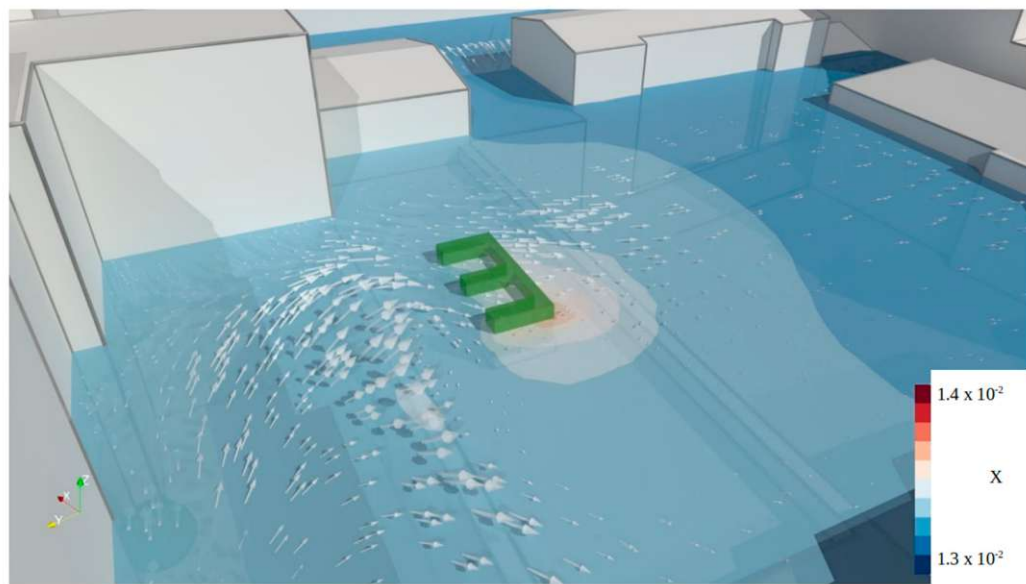


Figure 23. Humidity load (kg/kg) at the level of the Schuhmeierplatz School green pergola, 1.6 m above the ground, on the model day at 3:00 p.m. CEST.

In terms of the apparent (perceived) temperature by Steadman [33], a reduction of about $4\ ^{\circ}\text{C}$ can be noticed within the shade of the green pergola compared to the unshaded parts of the terrace, as shown in Figure 25. However, the cooling effect is primarily

dominated by the shading effect and less by the evapotranspiration performance of the plants.

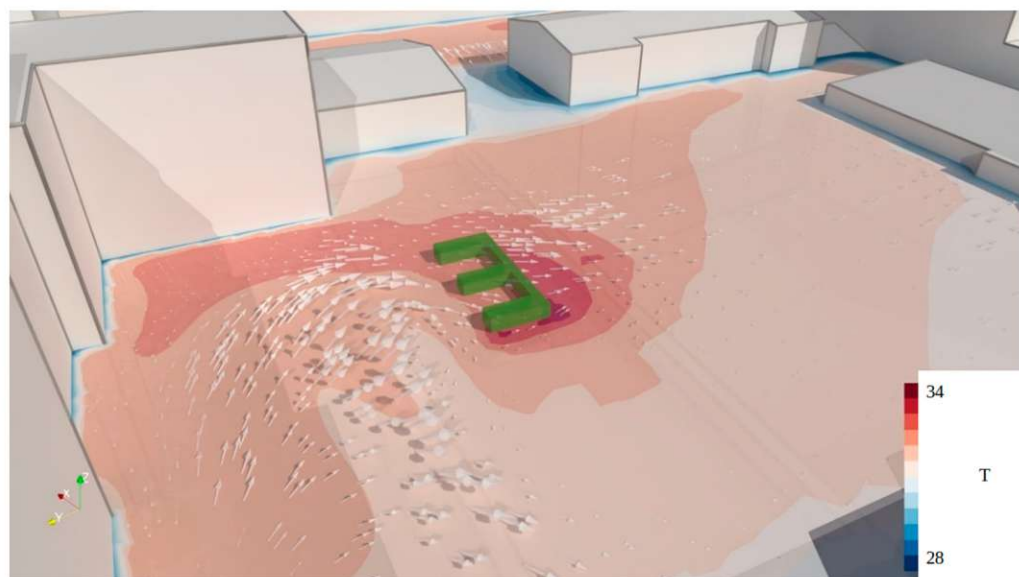


Figure 24. Air temperature ($^{\circ}\text{C}$) at the level of the Schuhmeierplatz School green pergola, 1.6 m above the ground, on the model day at 3:00 p.m. CEST.

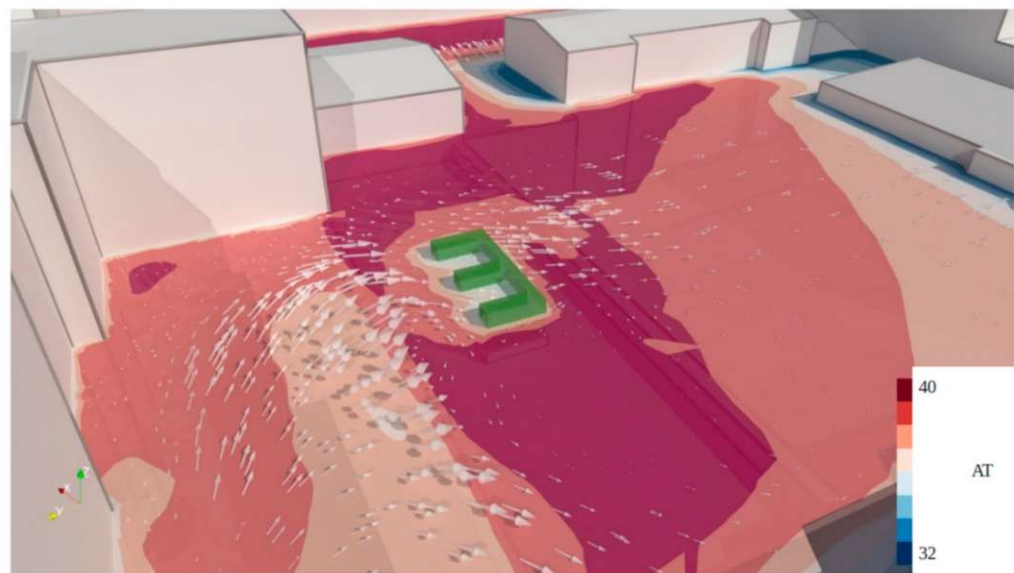


Figure 25. Apparent temperature ($^{\circ}\text{C}$) at pedestrian level on the roof terrace of Schuhmeierplatz School on the model day at 3:00 p.m. CEST.

As indicated in the plots of apparent temperature (Figure 26), surface temperatures (Figure 27), and incident radiation intensity (Figure 28) on the model day at 3:00 p.m. CEST, the more exposed roof surfaces and roof terraces are heated significantly more than shaded areas, such as the school's courtyard or the school forecourt. High incident radiation intensities and, consequently, high surface temperatures can also be seen on the roof terrace with the green pergola. Due to its small size, the reduction in the apparent temperature is limited to the space underneath. From a large-scale perspective, the influence of the green pergola seems to be negligible.



Figure 26. Apparent temperature ($^{\circ}\text{C}$) around Schuhmeierplatz School on the model day at 3:00 p.m. CEST.

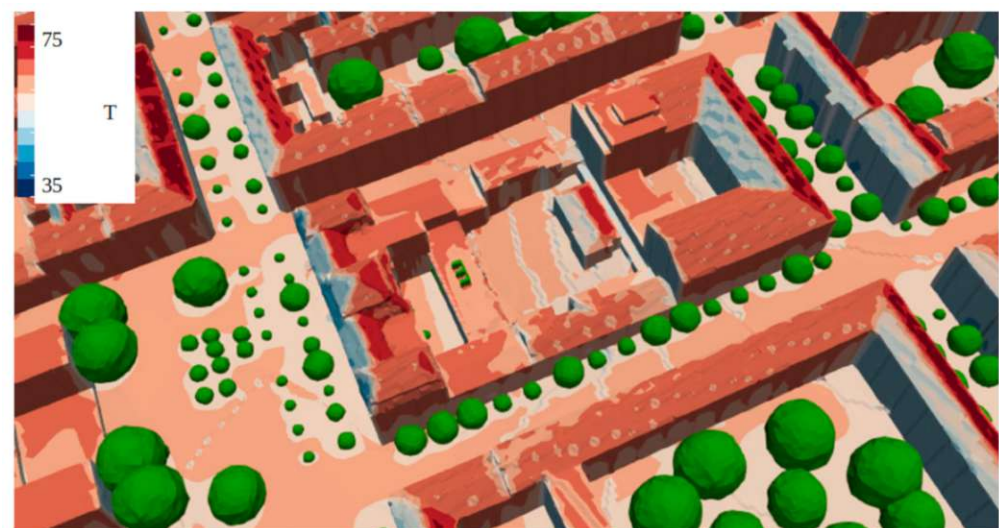


Figure 27. Surface temperatures ($^{\circ}\text{C}$) around Schuhmeierplatz School on the model day at 3:00 p.m. CEST.

At Schuhmeierplatz School, the results of the simulation validation by means of the experimental data show a very good concordance (see Figure 29), with an average absolute error of $-0.78\text{ }^{\circ}\text{C}$ and a standard deviation of absolute errors of $0.74\text{ }^{\circ}\text{C}$ at 3:00 p.m. CEST. As there are no air temperature sensors directly exposed to solar radiation, the error due to the usage of non-ventilated radiation shields can be neglected. Further information on the validation results is provided in Appendix D.

The measurements and simulations were repeated in summer 2022 using ventilated radiation shields to be able to quantify the measurement error when using non-ventilated radiation shields. However, the results of the measurements in 2022 are not included in this study because the analysis of the data has not yet been completed. From the simulations performed so far, it is already apparent that a greening measure alone has very minor effects on the microclimate. To significantly reduce the risk of overheating in an inner courtyard or roof terrace in summer, greening systems must be implemented on a much larger scale.

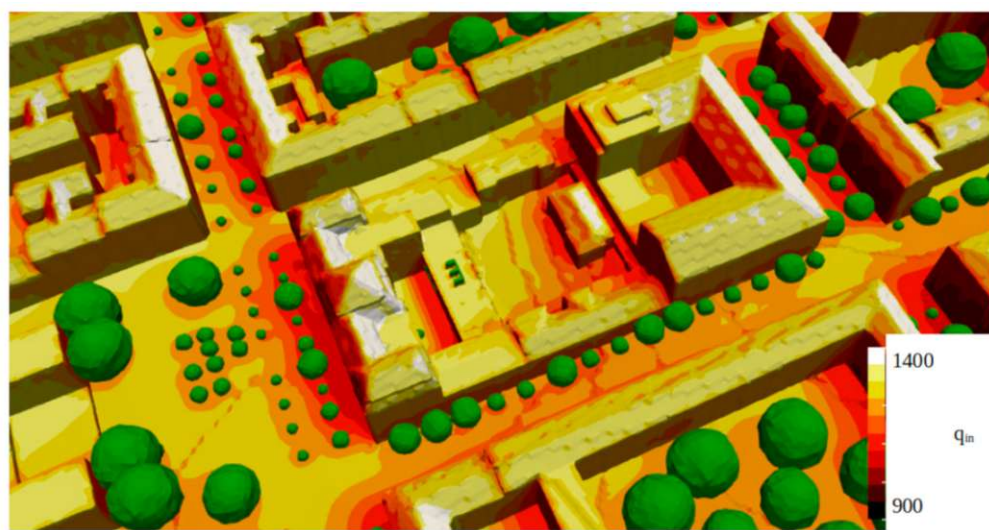


Figure 28. Incident radiation intensity (W/m^2) around Schuhmeierplatz School on the model day at 3:00 p.m. CEST.

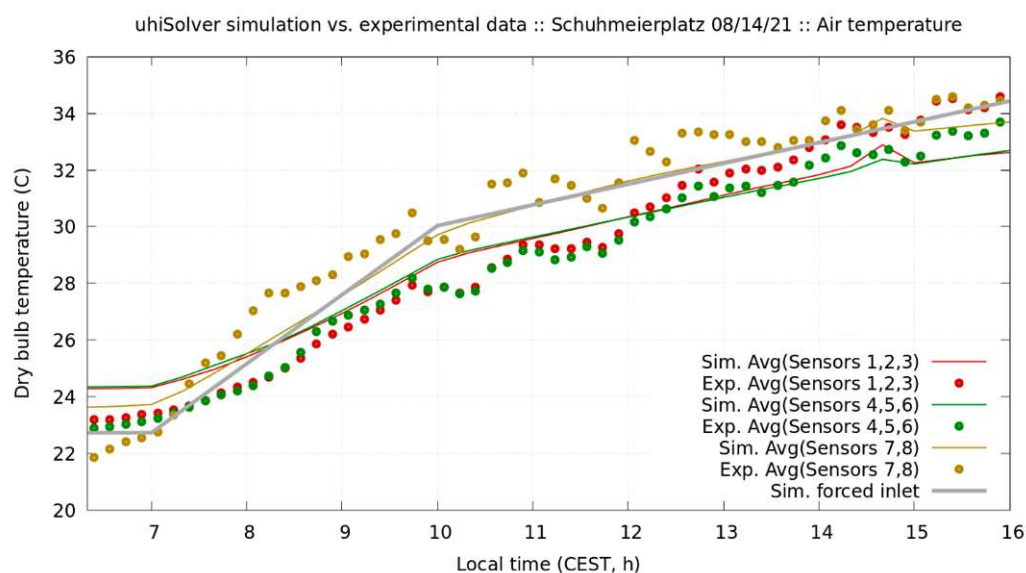


Figure 29. Validation of simulated air temperature with measured data at Schuhmeierplatz School on the model day from 06:20 a.m. to 4:00 p.m. CEST.

4. Discussion

In the present study, microclimate simulations are carried out with the software uhiSolver at two Viennese schools to investigate the influence of existing small-scale greenery systems in the inner courtyard and on the roof terrace, respectively, on the local microclimate. The simulation was validated with measurement data collected on-site. However, the measurement shows only minimal local effects of the greenery systems, even directly in front of the living walls and inside the green pergola. These insignificant effects are also seen in the closer free space in the simulation. These results are reproduced with tight intervals by uhiSolver. Hence, it is clearly shown that there is no significant local (0.5 m to 3 m distance from the wall) effect of small-scale living walls on thermodynamic and perceived temperatures on the outside, apart from building shading and lowered incident radiation behind the living wall (see Table 3). The green pergola is a special case, because of the larger shaded area compared to the living walls and proportionally bigger impact on outside apparent temperature. The biggest effect on apparent temperature is caused by the shading of the pergola, and not by air cooling due to evapotranspiration.

Table 3. Microclimatic effects of small-scale greenery on a hot summer day in Vienna.

	Air Temp.	Abs. Humidity	Shade	AT ¹
Living wall	No	Yes	Yes	No
Green pergola	No	Yes	Yes	Yes

¹ Apparent temperature by Steadman [33].

The greening of facades is currently a dominant topic in Vienna and many other metropolitan areas around the world. The city of Vienna has set the goal of significantly increasing its number of green facades in the coming years [34] and has, therefore, launched various options for the funding of vertical greenery systems. Nevertheless, implementation is mostly limited to individual small-scale greening projects, as large-scale implementation is still associated with considerable costs. The care and maintenance of vertical greenery systems is often neglected. Furthermore, failures of the irrigation systems occur frequently, which is why many systems, especially living walls, are in a poor condition. The results of this study, which showed a maximum air temperature reduction of 0.3 °C at a 0.1 m distance from the north and north-west-facing living walls and within the green pergola, are supported by the findings of Daemei et al., who detected a peak temperate reduction of 0.36 °C at 12 p.m. in front of a north-facing direct green façade [22]. The same value of air temperature reduction was measured by Galagoda et al., at a 1 m distance from south to east-oriented living walls [27], indicating a wider range of the cooling effect at vertical greenery systems that are more exposed to solar radiation.

Therefore, it seems obvious that a single vertical greenery system covering an area of just a few square meters is not enough to reduce the ambient air temperature and increase thermal comfort in summer. The greening of facades will have to be applied on a much larger scale, with estimated air temperature reductions of 0.3 °C when applying green facades with a coverage fraction of 50% within an east-west-oriented mid-rise low-density street canyon [24], and about 1 °C at a high-rise high-density scenario with 100% of the facades of a building block being covered with living walls [26]. Adding vegetation as avenue trees could lead to higher reductions in air temperature of up to 2 °C, especially in the shadow of the trees [23,24]. To substantially contribute to a reduction in the UHI effect in big cities, a combination of greenery systems with other microclimatic measures is needed, such as, for example, water sprays and fountains, enabling a decrease in the local air temperature by a maximum of 7 °C [23]. Furthermore, the influence of the increased humidity on the apparent (perceived) temperature must also be taken into account. At low wind speeds, the increased humidity of the vertical greenery system and/or water sprays will not be transported away and may lead to an increase in the perceived temperature, despite the air temperature being lowered. To ensure that an implemented greenery system has the desired effect on the microclimate, a combined consideration of the different effects of the greenery on the air temperature, the air humidity, and the surface temperature, as well as the incident surface radiation intensity must, therefore, be carried out.

Contributions to the fields of UHI research and policies of this study are as follows:

Scientific findings:

- It is clearly shown by both experimental and simulation data that small-scale greening measures—especially on north-facing or mostly shaded facades—cannot fulfill the expectations of any practical outside air cooling;
- The anticipated positive influence on microclimate is not achieved under a certain size (area, leaf area index, crown diameter, etc.) of the greening, which evidently has to be much larger than in the studied greenings;
- Providing convincing data on the ineffectiveness of some greening systems documents the root causes of failed implementations and incentivizes future research into apt measures in urban climate adaptation.

Recommendations for policy makers:

- Avoiding funding and construction of greening systems that are scientifically proven to be ineffective measures against overheating urban areas;
- In order to improve outside thermal comfort in summer, city authorities should focus on more differentiated, effective greening and shading measures instead of piecemeal living walls;
- Only perfectly maintained large-scale greening will provide some felt air cooling effect and, more importantly, reduce apparent temperatures and provide sufficient shade for pedestrians and buildings.

5. Conclusions

At two Viennese school buildings, north to northwest-facing living walls and a green pergola were examined. Transient dynamic microclimate simulations with the uhiSolver software were carried out that show a very small impact of the greening measures on the local microclimate, rapidly decreasing with increasing distance from the greenery. Compared to a bare wall, the maximum decrease in ambient air temperature at 0.1 m from the façade greening is 0.3 °C on a hot summer day at 3:00 p.m. local time (CEST). The same reduction in air temperature is obtained within the green pergola, whereas the apparent (perceived) temperature is reduced by up to 4 °C, mostly due to the shading of the green pergola compared to the unshaded roof terrace. A comparison with on-site measurement data shows a good agreement.

City departments' actions to mitigate UHI effects should simultaneously incorporate differentiated strategies and include the large-scale application of vertical greenery systems, green roofs—where possible and sensible—and large crown avenue trees. However, further research is needed to assess the influence of different vertical greenery systems on the local microclimate and to examine to what extent they may be able to contribute to mitigating UHI formation when applied at a city-scale.

Author Contributions: F.T.: conceptualization, investigation, methodology, resources, writing—original draft preparation, project administration. A.H. and M.L.: software, data curation, validation, visualization. A.K.: writing—review and editing, supervision, funding acquisition. All authors have read and agreed to the published version of the manuscript.

Funding: This research was funded by Klima- und Energiefonds and Österreichische Forschungsförderungsgesellschaft FFG, grant number 884762.

Institutional Review Board Statement: Not applicable.

Data Availability Statement: The data that support the findings of this study are available from Rheologic GmbH but restrictions apply to the availability of these data, which were used under license for the current study, and so are not publicly available. Data are however available from the authors upon reasonable request and with permission of Rheologic GmbH.

Acknowledgments: This research was supported by the Austrian Research Promotion Agency (FFG) as well as by the Climate and Energy Fund of the Federal Ministry for Climate Action, Environment, Energy, Mobility, Innovation and Technology (BMK) within the framework of the Smart Cities Demo—Boosting Urban Innovation funding line. Open Access Funding by TU Wien.

Conflicts of Interest: The authors declare no conflict of interest. The funders had no role in the design of the study; in the collection, analyses, or interpretation of data; in the writing of the manuscript, or in the decision to publish the results.

Appendix A

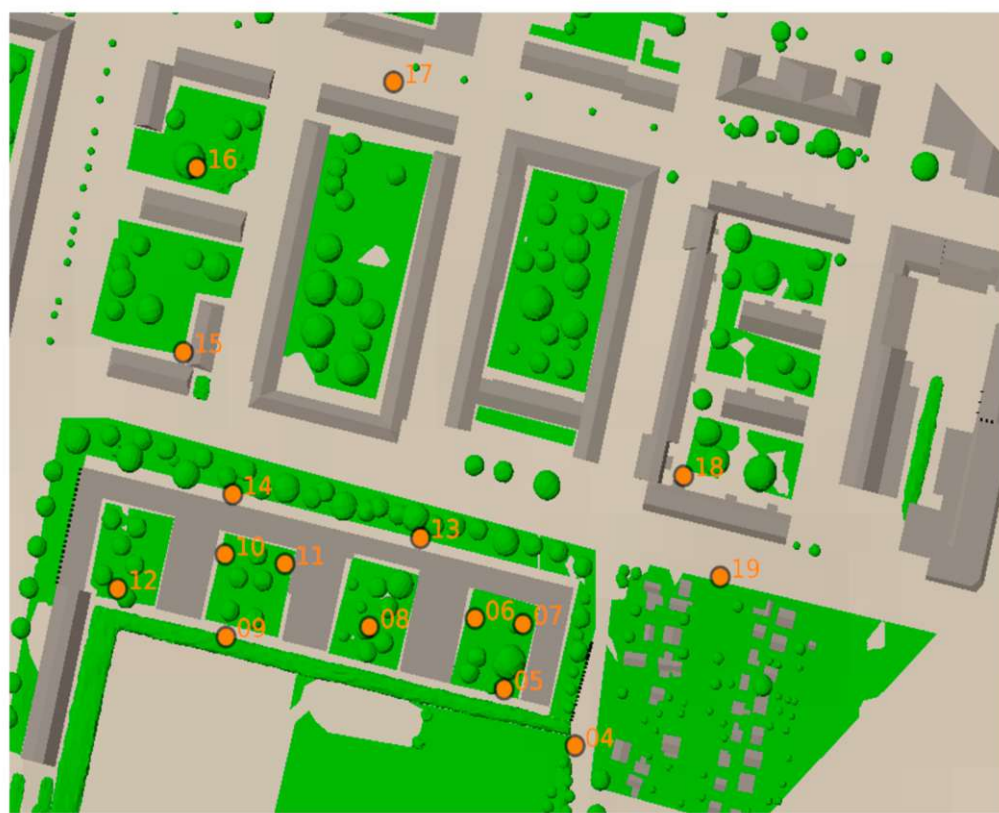


Figure A1. Sample positions at the 16.31954 E, 48.20599 N geo-coordinates for the validation case of Gablenzgasse.

Table A1. The uhiSolver simulation results for the validation case of Gablenzgasse, Vienna, on 29 June 2021 at 15:00 to 16:10 CEST.

Pos. (1)	Time (CEST)	U (m/s)	uhiSolver Simulation Results					
			T (Air) (K)	T (Air) (C)	RH (%)	AT (°C)	X (g/kg)	
04		0.95	303.6	30.5	0.43	39.36	11.937	
05	15:00	0.07	303.2	30.1	0.45	40.88	12.120	
06		0.13	303.0	29.8	0.46	40.22	12.301	
07		0.24	302.9	29.7	0.46	40.01	12.112	
08	15:10	0.16	302.9	29.7	0.46	40.19	12.206	
09	15:15	0.31	303.2	30.0	0.45	40.12	12.053	
10		0.17	302.9	29.7	0.46	39.90	12.087	
11		0.33	303.2	30.1	0.44	40.26	11.933	
12	15:30	0.31	303.0	29.8	0.45	39.81	12.019	
13		0.24	302.3	29.2	0.47	39.05	12.082	
14	15:45	0.03	302.4	29.2	0.47	39.53	12.124	
15		0.22	302.8	29.6	0.45	39.37	11.837	
16		0.15	302.5	29.4	0.47	39.61	12.078	
17	16:00	0.07	302.4	29.3	0.46	39.60	11.891	
18	16:10	0.11	301.9	28.7	0.49	38.83	12.167	
19		0.56	303.2	30.0	0.44	39.89	11.933	

Table A2. Experimental data for the validation case of Gablenzgasse, Vienna, on 29 June 2021 at 15:00 to 16:10 CEST.

Pos. (1)	Time (CEST)	U min (m/s)	U max (m/s)	U avg (m/s)	Experimental Data T (air) (C)	RH (%)	X (g/kg)
04		0.20	0.20	0.20	31.2	41.7	12.000
05	15:00	0.20	0.30	0.25	29.8	45.1	11.953
06		0.10	0.10	0.10	29.5	45.1	11.737
07		0.30	0.30	0.30	32.3	41.0	12.577
08	15:10	0.50	0.50	0.50	29.8	45.3	12.047
09	15:15	0.16	0.20	0.18	29.8	44.7	11.848
10		0.10	0.20	0.15	30.1	45.7	12.362
11		0.15	0.15	0.15	32.5	39.2	12.152
12	15:30	0.30	0.45	0.38	29.1	45.7	11.625
13		0.60	1.20	0.90	29.5	44.6	11.648
14	15:45	0.70	0.95	0.83	30.1	43.5	11.753
15		0.20	0.30	0.25	30.0	44.6	11.957
16		1.50	1.80	1.65	29.3	46.8	12.072
17	16:00	0.50	0.50	0.50	30.4	41.8	11.496
18	16:10	0.20	0.45	0.33	29.2	46.2	11.871
19		0.20	0.50	0.35	30.7	41.0	11.488

Table A3. Absolute error between the uhiSolver simulation results and experimental data for the validation case of Gablenzgasse, Vienna, on 29 June 2021 at 15:00 to 16:10 CEST.

Pos. (1)	Time (CEST)	uhiSolver U (m/s)	Absolute Error T (K)	Absolute Error X (g/kg)
04		0.75	-0.7	-0.063
05	15:00	-0.18	0.3	0.167
06		0.03	0.3	0.564
07		-0.06	-2.6	-0.466
08	15:10	-0.34	-0.1	0.160
09	15:15	0.13	0.3	0.205
10		0.02	-0.4	-0.275
11		0.18	-2.4	-0.218
12	15:30	-0.06	0.8	0.394
13		-0.66	-0.3	0.435
14	15:45	-0.79	-0.9	0.371
15		-0.03	-0.3	-0.120
16		-1.50	0.1	0.007
17	16:00	-0.43	-1.2	0.395
18	16:10	-0.22	-0.5	0.296
19		0.21	-0.7	0.445

Table A4. Averaged absolute errors and standard deviation of absolute errors for the validation case of Gablenzgasse, Vienna, on 29 June 2021 at 15:00 to 16:10 CEST.

Averaged Absolute Errors		
U (m/s) -0.18	T (K) -0.53	X (g/kg) 0.143
Std. Dev. of Absolute Errors		
U (m/s) 0.50	T (K) 0.93	X (g/kg) 0.302

Appendix B



Figure A2. Sample positions at the 16.36237 E, 48.19798 N geo-coordinates for the validation case of Naschmarkt.

Table A5. The uhiSolver simulation results for the validation case of Naschmarkt, Vienna, on 21 June 2022 at 14:00 to 15:55 CEST.

Pos. (1)	Time (CEST)	uhiSolver Simulation Results					
		U (m/s)	T (Air) (K)	T (Air) (C)	RH (1)	AT (°C)	X (g/kg)
01	14:00	1.4	304.9	31.7	0.45	40.2	13.45
02		0.9	305.4	32.2	0.43	41.6	13.45
03		0.6	305.8	32.7	0.42	44.1	13.45
04		0.5	305.8	32.7	0.42	42.8	13.47
05		1.2	305.7	32.5	0.43	41.2	13.48
06		0.2	306.1	32.9	0.43	45.2	13.76
07		0.0	304.9	31.7	0.46	43.0	13.78
08		0.1	304.3	31.2	0.48	42.2	13.88
09	15:00	0.1	303.2	30.0	0.52	41.4	14.37
10		0.2	305.6	32.5	0.45	44.6	14.09
11	15:10	0.1	304.6	31.4	0.48	42.7	14.14
12		0.2	304.1	30.9	0.47	41.7	13.60
13		0.9	305.2	32.1	0.44	41.5	13.47
14		1.4	305.7	32.5	0.43	40.8	13.45
15	15:40	0.5	304.8	31.6	0.45	42.0	13.47
16		2.0	305.4	32.3	0.43	39.7	13.44
17	15:55	2.3	305.9	32.8	0.42	39.6	13.44

Table A6. Experimental data for the validation case of Naschmarkt, Vienna, on 21 June 2022 at 14:00 to 15:55 CEST.

Pos.	Time	Experimental Data							
		(1)	(CEST)	U min (m/s)	U max (m/s)	U avg (m/s)	T (Air) (C)	RH (%)	X (g/kg)
01	14:00			1.2	2.6	1.9	31.0	33.3	10.77
02				1.5	1.5	1.5	31.0	32.6	10.13
03				0.9	0.9	0.9	30.1	30.6	8.46
04				0.3	0.7	0.5	31.1	32.9	10.40
05				0.8	0.8	0.8	31.7	32.3	9.86
06				1.1	1.1	1.1	31.7	29.5	7.65
07				0.2	0.2	0.2	30.9	30.3	8.23
08				0.5	0.5	0.5	30.7	33.0	10.49
09	15:00			0.5	1.0	0.8	31.7	33.5	10.96
10				0.3	0.7	0.5	31.6	32.3	9.86
11	15:10			0.3	0.3	0.3	30.1	35.8	13.36
12				0.7	0.7	0.7	32.1	31.6	9.26
13				0.7	0.7	0.7	32.2	31.7	9.35
14				1.1	1.1	1.1	34.0	29.6	7.72
15	15:40			0.7	2.1	1.4	33.4	29.5	7.65
16				0.4	1.4	0.9	33.1	29.3	7.51
17	15:55			0.7	2.5	1.6	32.5	31.3	9.02

Table A7. Absolute error between the uhiSolver simulation results and the experimental data for the validation case of Naschmarkt, Vienna, on 21 June 2022 at 14:00 to 15:55 CEST.

Pos.	Time	uhiSolver Absolute Error				
		(1)	(CEST)	U (m/s)	T (K)	X (g/kg)
01	14:00			-0.5	0.7	2.68
02				-0.6	1.2	3.32
03				-0.3	2.6	4.99
04				0.0	1.6	3.07
05				0.4	0.8	3.62
06				-0.9	1.2	6.11
07				-0.2	0.8	5.55
08				-0.4	0.5	3.39
09	15:00			-0.7	-1.7	3.41
10				-0.3	0.9	4.23
11	15:10			-0.2	1.3	0.78
12				-0.5	-1.2	4.34
13				0.2	-0.1	4.12
14				0.3	-1.5	5.74
15	15:40			-0.9	-1.8	5.83
16				1.1	-0.8	5.93
17	15:55			0.7	0.3	4.43

Table A8. Averaged absolute errors and standard deviation of absolute errors for the validation case of Naschmarkt, Vienna, on 21 June 2022 at 14:00 to 15:55 CEST.

Averaged Absolute Errors		
U (m/s)	T (K)	X (g/kg)
-0.19	0.09	4.19
Std. Dev. of Absolute Errors		
U (m/s)	T (K)	X (g/kg)
0.63	1.13	1.89

Appendix C

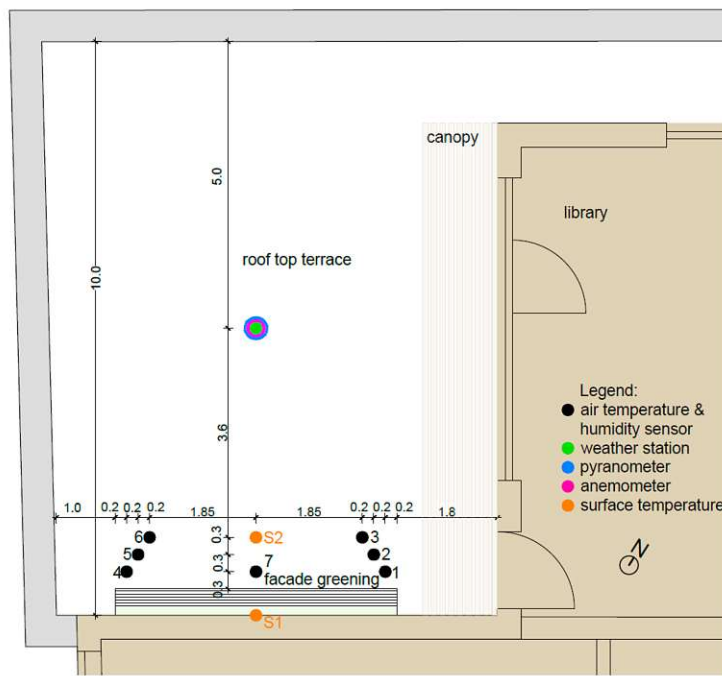


Figure A3. Sample positions at the 16.33293 E, 48.18555 N geo-coordinates for the Diefenbachgasse School with the air temperature and humidity sensors 1 to 7 and the surface temperature sensors S1 and S2.

Table A9. The uhiSolver simulation results for Diefenbachgasse School on the model day at 15:00 CEST.

Pos. (1)	uhiSolver Simulation Results				
	U (m/s)	Wind-Dir. (-)	T (Air) (°C)	RH (%)	X (g/kg)
1	0.4	WSW	31.2	47	0.0136
2	0.4	WSW	31.2	47	0.0136
3	0.4	WSW	31.2	47	0.0136
4	0.6	WSW	31.5	45	0.0135
5	0.6	WSW	31.7	45	0.0135
6	0.6	WSW	31.7	45	0.0135
7	0.6	WSW	31.7	44	0.0135
W.S.	0.6	WSW	31.6	45	0.0135

Table A10. Experimental data for Diefenbachgasse School on the model day at 15:00 CEST.

Pos. (1)	Experimental Data					
	U min (m/s)	U max (m/s)	U avg (m/s)	Wind-Dir. (-)	T (Air) (°C)	RH (%)
1	-	-	-	-	34.2	35
2	-	-	-	-	35.0	33
3	-	-	-	-	35.0	32
4	-	-	-	-	34.4	33
5	-	-	-	-	32.0	31
6	-	-	-	-	34.7	29
7	-	-	-	-	33.9	32
W.S.	0.4	3.2	1.6	SW	34.8	37
					X (kg/kg)	

Table A11. Absolute error between the uhiSolver simulation results and the experimental data for Diefenbachgasse School on the model day at 15:00 CEST.

Pos. (1)	uhiSolver Absolute Error		
	U (m/s)	T (K)	X (kg/kg)
1	-	-3.0	0.0021
2	-	-3.8	0.0016
3	-	-3.8	0.0016
4	-	-2.9	0.0025
5	-	-0.3	0.0045
6	-	-3.0	0.0045
7	-	-2.2	0.0030
W.S.	-1.0	-3.2	0.0005

Table A12. Averaged absolute errors and standard deviation of absolute errors for Diefenbachgasse School on the model day at 15:00 CEST.

Averaged Absolute Errors		
U (m/s)	T (K)	X (kg/kg)
-1.0	-2.78	0.0025
Std. Dev. of Absolute Errors		
U (m/s)	T (K)	X (kg/kg)
-	1.12	0.0014

Appendix D

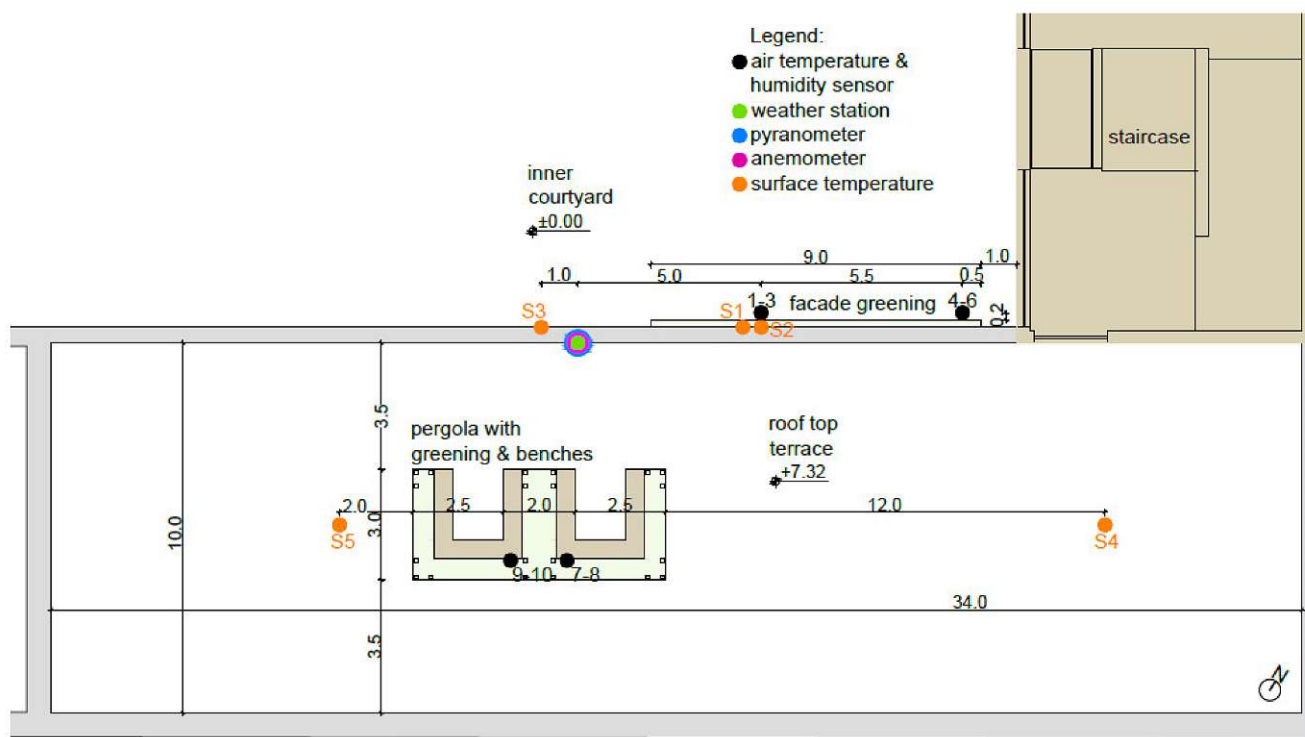


Figure A4. Sample positions at the 16.31892 E, 48.20989 N geo-coordinates for the Schuhmeier-platz School with the air temperature and humidity sensors 1 to 10 and the surface temperature sensors S1 to S5.

Table A13. The uhiSolver simulation results for Schuhmeierplatz school on the model day at 15:00 CEST.

Pos. (1)	uhiSolver Simulation Results				
	U (m/s)	Wind-Dir. (-)	T (Air) (°C)	RH (%)	X (kg/kg)
1	0.3	E	32.3	44	0.0136
2	0.3	E	32.3	44	0.0136
3	0.3	E	32.3	44	0.0136
4	0.3	E	32.1	44	0.0135
5	0.3	E	32.2	44	0.0135
6	0.3	E	32.3	43	0.0135
7	0.2	NNE	33.4	41	0.0136
8	0.2	NNE	33.4	41	0.0136
W.S.	0.3	ESE	32.6	43	0.0135

Table A14. Experimental data for Schuhmeierplatz school on the model day at 15:00 CEST.

Pos. (1)	Experimental Data						X (kg/kg)
	U min (m/s)	U max (m/s)	U avg (m/s)	Wind-Dir. (-)	T (Air) (°C)	RH (%)	
1	-	-	-	-	33.0	43	0.0140
2	-	-	-	-	34.5	41	0.0145
3	-	-	-	-	33.8	43	0.0145
4	-	-	-	-	32.5	43	0.0135
5	-	-	-	-	32.7	42	0.0135
6	-	-	-	-	32.3	45	0.0130
7	-	-	-	-	34.2	40	0.0135
8	-	-	-	-	33.2	43	0.0135
W.S.	3.2	4.8	4.0	ESE	33.7	40	0.0133

Table A15. Absolute error between the uhiSolver simulation results and the experimental data for Schuhmeierplatz School on the model day at 15:00 CEST.

Pos. (1)	uhiSolver Absolute Error		
	U (m/s)	T (K)	X (kg/kg)
1	-	-0.7	-0.0004
2	-	-2.3	-0.0009
3	-	-1.5	-0.0009
4	-	-0.4	0.0000
5	-	-0.5	0.0000
6	-	0.1	0.0005
7	-	-0.8	0.0001
8	-	0.2	0.0001
W.S.	-3.7	-1.1	0.0002

Table A16. Averaged absolute errors and standard deviation of absolute errors for Schuhmeierplatz School on the model day at 15:00 CEST.

Averaged Absolute Errors		
U (m/s)	T (K)	X (kg/kg)
-3.7	-0.78	0.0001
Std. Dev. of Absolute Errors		
U (m/s)	T (K)	X (kg/kg)
-	0.74	0.0005

References

- Mursch-Radlgruber, E.; Trimmel, H.; Gerersdorfer, T. *Räumliche Differenzierung der Mikroklimatischen Eigenschaften von Wiener Stadtstrukturen und Anpassungsmaßnahmen. Ergebnisse Kleinklimatischer Messungen. Teil 2 der Studie Räumlich und Zeitlich hoch Aufgelöste Temperaturszenarien für Wien und Ausgewählte Analysen Beziiglich Adaptationsstrategien*; University of Natural Resources and Life Sciences: Vienna, Austria, 2009.
- Steininger, K.W.; Haas, W.; König, M.; Pech, M.; Prettenthaler, F.; Prutsch, A.; Temessl, M.; Wagner, G.; Wolf, A. *Die Folgeschäden des Klimawandels in Österreich. Dimensionen unserer Zukunft in zehn Bildern für Österreich. Broschüre aus dem Forschungsprojekt COIN*; Klima Energie Fonds: Vienna, Austria, 2015.
- Larsen, L. Urban climate and adaptation strategies. *Front. Ecol. Environ.* **2015**, *13*, 486–492. [[CrossRef](#)]
- Köhler, M. Green facades—a view back and some visions. *Urban Ecosyst.* **2008**, *11*, 423–436. [[CrossRef](#)]
- Rakhshandehroo, M.; Mohd Yusof, M.J.; Deghati Najd, M. Green Façade (Vertical Greening): Benefits and Threats. *Appl. Mech. Mater.* **2015**, *747*, 12–15. [[CrossRef](#)]
- Hoelscher, M.-T.; Nehls, T.; Jänicke, B.; Wessolek, G. Quantifying cooling effects of facade greening: Shading, transpiration and insulation. *Energy Build.* **2016**, *114*, 283–290. [[CrossRef](#)]
- Hollands, J.; Tudiwer, D.; Korjenic, A.; Bretschneider, B.B. Greening Aspang—Messtechnische Untersuchungen zur ganzheitlichen Betrachtung mikroklimatischer Wechselwirkungen in einem Straßenzug einer urbanen Hitzeinsel. *Bauphysik* **2018**, *40*, 105–119. [[CrossRef](#)]
- Tudiwer, D.; Korjenic, A. The Risk of Humidity at Greened Façades. *Appl. Mech. Mater.* **2016**, *861*, 343–350. [[CrossRef](#)]
- Tudiwer, D.; Korjenic, A. The effect of living wall systems on the thermal resistance of the façade. *Energy Build.* **2017**, *135*, 10–19. [[CrossRef](#)]
- Tudiwer, D.; Höckner, V.; Korjenic, A. Greening Aspang—Hygrothermische Gebäudesimulation zur Bestandsanalyse und Bewertung unterschiedlicher Szenarien bezogen auf das Innenraumklima. *Bauphysik* **2018**, *40*, 120–130. [[CrossRef](#)]
- Besir, A.B.; Cuce, E. Green roofs and facades: A comprehensive review. *Renew. Sustain. Energy Rev.* **2018**, *82*, 915–939. [[CrossRef](#)]
- Solera Jimenez, M. Green walls: A sustainable approach to climate change, a case study of London. *Arch. Sci. Rev.* **2018**, *61*, 48–57. [[CrossRef](#)]
- Tan, C.L.; Wong, N.H.; Jusuf, S.K. Effects of vertical greenery on mean radiant temperature in the tropical urban environment. *Landsc. Urban Plan.* **2014**, *127*, 52–64. [[CrossRef](#)]
- Azkorra, Z.; Pérez, G.; Coma, J.; Cabeza, L.F.; Burés, S.; Álvaro, J.E.; Erkoreka, A.; Urrestarazu, M. Evaluation of green walls as a passive acoustic insulation system for buildings. *Appl. Acoust.* **2015**, *89*, 46–56. [[CrossRef](#)]
- Pettit, T.; Irga, P.J.; Torpy, F.R. Functional green wall development for increasing air pollutant phytoremediation: Substrate development with coconut coir and activated carbon. *J. Hazard. Mater.* **2018**, *360*, 594–603. [[CrossRef](#)] [[PubMed](#)]
- Susorova, I. Green facades and living walls: Vertical vegetation as a construction material to reduce building cooling loads. *Eco-Eff. Mater. Mitig. Build. Cool. Needs Des. Prop. Appl.* **2015**, *127*–153. (accessed on 1 June 2022). [[CrossRef](#)]
- Pérez, G.; Coma, J.; Martorell, I.; Cabeza, L.F. Vertical Greenery Systems (VGS) for energy saving in buildings: A review. *Renew. Sustain. Energy Rev.* **2014**, *39*, 139–165. [[CrossRef](#)]
- Lundholm, J.T. Green Roofs and Facades: A Habitat Template Approach. *Urban Habit.* **2006**, *4*, 87–101. Available online: <http://www.urbanhabitats.org> (accessed on 1 June 2022).
- Manso, M.; Castro-Gomes, J. Green wall systems: A review of their characteristics. *Renew. Sustain. Energy Rev.* **2015**, *41*, 863–871. [[CrossRef](#)]
- Korjenic, A.; Tudiwer, D.; Penaranda Moren, M.S.; Hollands, J.; Salonen, T.; Mitterböck, M.; Pitha, U.; Zluwa, I.; Stangl, R.; Kräftner, J.; et al. *GrünPlusSchule@Ballungszentrum: Hocheffiziente Fassaden- und Dachbegrünung mit Photovoltaik Kombination; optimale Lösung für die Energieeffizienz in Gesamtökologischer Betrachtung: Endbericht, Stadt der Zukunft*; Bundesministerium für Klimaschutz, Umwelt, Energie, Mobilität, Innovation und Technologie (BMK): Vienna, Austria, 2018.
- Teichmann, F.; Baumgartner, C.M.; Horvath, A.; Luisser, M.; Korjenic, A. Simulation of urban microclimate with uhiSolver: Software validation using simplified material data. *Ecol. Process.* **2021**, *10*, 67. [[CrossRef](#)]
- Daemei, A.B.; Shafiee, E.; Chitgar, A.A.; Asadi, S. Investigating the thermal performance of green wall: Experimental analysis, deep learning model, and simulation studies in a humid climate. *Build. Environ.* **2021**, *205*, 108201. [[CrossRef](#)]
- Fahed, J.; Kinab, E.; Ginestet, S.; Adolphe, L. Impact of urban heat island mitigation measures on microclimate and pedestrian comfort in a dense urban district of Lebanon. *Sustain. Cities Soc.* **2020**, *61*, 102375. [[CrossRef](#)]
- Gromke, C.; Blocken, B.; Janssen, W.; Merema, B.; van Hooff, T.; Timmermans, H. CFD analysis of transpirational cooling by vegetation: Case study for specific meteorological conditions during a heat wave in Arnhem, Netherlands. *Build. Environ.* **2015**, *83*, 11–26. [[CrossRef](#)]
- Morakinyo, T.E.; Lai, A.; Lau, K.K.-L.; Ng, E. Thermal benefits of vertical greening in a high-density city: Case study of Hong Kong. *Urb. For. Urban Green.* **2019**, *37*, 42–55. [[CrossRef](#)]
- Peng, L.L.H.; Jiang, Z.; Yang, X.; He, Y.; Xu, T.; Chen, S.S. Cooling effects of block-scale facade greening and their relationship with urban form. *Build. Environ.* **2020**, *169*, 106552. [[CrossRef](#)]
- Galagoda, R.U.; Jayasinghe, G.Y.; Halwatura, R.U.; Rupasinghe, H.T. The impact of urban green infrastructure as a sustainable approach towards tropical micro-climatic changes and human thermal comfort. *Urban For. Urban Green.* **2018**, *34*, 1–9. [[CrossRef](#)]

28. Korjenic, A.; Dopheide, R.; Knoll, B.; Pitha, U. GRÜNE Zukunft SCHULEN—*Grüne Schuloasen im Neubau. Fokus Planungsprozess und Bestandsgebäude: Endbericht*; Klima Energie Fonds: Vienna, Austria, 2020.
29. ENVI-met GmbH. Software: Designing Cities of the Future Today with ENVI-Met. Available online: <https://www.envi-met.com/software/> (accessed on 1 June 2022).
30. Dayer, S.; Herrera, J.C.; Dai, Z.; Burlett, R.; Lamarque, L.J.; Delzon, S.; Bortolami, G.; Cochard, H.; Gambetta, G.A. Nighttime transpiration represents a negligible part of water loss and does not increase the risk of water stress in grapevine. *Plant. Cell Environ.* **2021**, *44*, 387–398. [[CrossRef](#)]
31. Hollands, J. Ecological, Economic and Energy-Related Effects of Facade Greenery—Developing a Model of Evaluation. Master’s Thesis, TU Wien, Vienna, Austria, 2017.
32. Meteoblue, A.G. Wetterarchiv Wien. 2022. Available online: https://www.meteoblue.com/de/wetter/historyclimate/weatherarchive/wien_%c3%96sterreich_2761369 (accessed on 1 September 2022).
33. Steadman, R.G. Norms of apparent temperature in Australia. *Aust. Met. Mag.* **1994**, *43*, 1–16.
34. Damyanovic, D.; Reinwald, F.; Brandenburg, C.; Allex, B.; Gantner, B.; Morawetz, U.; Preiss, J. Pilot Action City of Vienna—UHI-STRAT Vienna. In *Counteracting Urban Heat Island Effects in a Global Climate Change Scenario*; Springer International Publishing: New York, NY, USA, 2016; pp. 257–280. [[CrossRef](#)]

8.3 Dritte Publikation

Status	Veröffentlicht am 28. Februar 2024
Original Titel (Englisch)	Measurement Errors When Measuring Temperature in the Sun
Titel (Deutsch)	Messfehler bei der Temperaturmessung in der Sonne
Autor:innen	Florian Teichmann, Alexander Pichlhöfer, Abdulah Sulejmanovski, Azra Korjenic
ISBN/ISSN	ISSN: 1424-8220 DOI: 10.3390/s24051564
Sprache	Englisch
Schlagwörter	radiation shield; radiation error; measurement error; air temperature measurement
Quelle	<i>Sensors</i> , Vol. 24, Issue 5, Artikel 1564 (2024), Special Issue: Integrated Sensor Systems for Environmental Applications, MDPI [Peer Reviewed Journal]

Article

Measurement Errors When Measuring Temperature in the Sun

Florian Teichmann *, Alexander Pichlhöfer , Abdulah Sulejmanovski  and Azra Korjenic 

Institute of Material Technology, Building Physics and Building Ecology, Vienna University of Technology (TU Wien), 1040 Vienna, Austria; azra.korjenic@tuwien.ac.at (A.K.)

* Correspondence: florian.teichmann@tuwien.ac.at

Abstract: In the validation of microclimate simulation software, the comparison of simulation results with on-site measurements is a common practice. To ensure reliable validation, it is crucial to utilize high-quality temperature sensors with a deviation smaller than the average absolute error of the simulation software. However, previous validation campaigns have identified significant absolute errors, particularly during periods of high solar radiation, possibly attributed to the use of non-ventilated radiation shields. This study addresses the issue by introducing a ventilated radiation shield created through 3D printing, aiming to enhance the accuracy of measurements on cloudless summer days with intense solar radiation. The investigation employs two pairs of sensors, each comprising one sensor with a ventilated and one with a non-ventilated radiation shield, placed on a south-oriented facade with two distinct albedos. Results from the measurement campaign indicate that the air temperature measured by the non-ventilated sensor is elevated by up to 2.8 °C at high albedo and up to 1.9 °C at a low albedo facade, compared to measurements with the ventilated radiation shield. An in-depth analysis of means, standard deviations, and 95% fractiles highlights the strong dependency of the non-ventilated sensor error on wind velocity. This research underscores the importance of employing ventilated radiation shields for accurate microclimate measurements, particularly in scenarios involving high solar radiation, contributing valuable insights for researchers and practitioners engaged in microclimate simulation validation processes.

Keywords: radiation shield; radiation error; measurement error; air temperature measurement



Citation: Teichmann, F.; Pichlhöfer, A.;

Sulejmanovski, A.; Korjenic, A.

Measurement Errors When Measuring Temperature in the Sun. *Sensors* **2024**, *24*, 1564. <https://doi.org/10.3390/s24051564>

Academic Editor: Michele Penza

Received: 5 February 2024

Revised: 23 February 2024

Accepted: 25 February 2024

Published: 28 February 2024



Copyright: © 2024 by the authors.

Licensee MDPI, Basel, Switzerland.

This article is an open access article distributed under the terms and conditions of the Creative Commons Attribution (CC BY) license (<https://creativecommons.org/licenses/by/4.0/>).

1. Introduction

Temperature measurements play a pivotal role in assessing the impact of building greening on the local microclimate and in validating corresponding microclimate simulations. Recent investigations have highlighted substantial disparities between on-site temperature measurements and simulation outcomes, particularly when temperature sensors are exposed to direct solar radiation. This exposure results in an average absolute error ranging from 0.78 °C to 2.78 °C, with a standard deviation of absolute errors spanning 0.74 °C to 1.12 °C at 3:00 p.m. CEST [1–3]. However, the precise attribution of this absolute error to either the effects of direct solar irradiation or the inaccuracies within Computational Fluid Dynamics (CFD) simulation programs remains indistinct. Hence, a comprehensive examination of on-site temperature measurements is imperative to facilitate a realistic interpretation of CFD simulation results.

The intricate relationship between various environmental factors and temperature has been explored in numerous studies. Avraham et al. [4] posit a robust and rapid connection between air temperature measurements derived from radiance power and changes in absolute humidity. As emphasized by Erell et al. [5], the presence of short or long-wave radiation can introduce unacceptable errors in measurement accuracy. Direct sunlight on the temperature sensor's surface heats the sensor, elevating the temperature around it compared to ambient air. To mitigate this, weather stations commonly employ radiation shields in front of temperature sensors. However, aging coatings diminish their ability to reflect sunlight, introducing errors up to 1.63 °C [6]. Moreover, reduced air

circulation within non-ventilated radiation shields can impede the sensor's response speed, resulting in a temperature error of 2–4 °C on clear, windless days at noon [7]. In summary, understanding the accuracy of temperature measurements necessitates the consideration of several environmental factors.

Research on radiation errors of fine-wire thermocouples (~0.1 mm diameter) within naturally aspirated radiation shields by Kurzeja [8] achieved a root-mean-square error of measured temperature at 0.35 °C and 0.16 °C, without and with correction, respectively. Nakamura and Mahrt [9], addressing the influence of wind speed and short-wave radiation on temperature measurements, proposed an empirical model with a root-mean-square error between measured and corrected values of 0.13 °C, albeit neglecting the impact of diffuse and direct solar radiation. Cheng et al. [10], analyzing temperature measurement errors between Chinese and imported radiation shields, achieved accuracies of 0.26 °C and 0.17 °C, respectively, with an improved correction method accounting for global solar radiation and wind speed effects on air temperature. Liu et al. [11] proposed a novel natural ventilated radiation shield, employing a back-propagation neural network algorithm to reduce radiation errors to within ± 0.1 °C at wind speeds exceeding 1.5 m/s. These results are comparable to those of ventilated radiation shields, which typically achieve a root-mean-square error of less than 0.2 °C [12,13].

Despite advancements in traditional radiation shields, a significant error range persists in measurements with direct and indirect solar radiation, primarily dependent on wind speed. This study aims to investigate the influence of wind speed on the accuracy of non-ventilated sensors. Two pairs of sensors, one equipped with a non-ventilated radiation shield and the other with a ventilated radiation shield, were mounted on a south-oriented facade with varying albedos. Simultaneously, wind speed measurements were conducted atop the test stand. The subsequent section details the test equipment and research setting.

2. Materials and Methods

The ventilated radiation shields used in this study were developed at the TU Wien in 2022 to reduce measurement errors in temperature measurements with the influence of radiation. To produce these radiation shields, a total of 7 plastic parts were printed using a 3D printer (XYZ resolution 12.5, 12.5, 5 microns). These can be assembled together with an electric fan (60 × 60 × 15 mm, 4200 rpm, 0.58 m³/min) and white-painted aluminum housing (sheet thickness 2 mm, diameters 60 mm and 80 mm) to form a radiation shield (see Figure 1). The aluminum housing provides effective thermal insulation and is less likely to heat up than non-ventilated radiation shields. The thermal insulation in ventilated radiation shields is achieved by airflow between two aluminum tubes. This helps reduce the heat generated by external solar radiation and allows the sensor inside the tube to accurately measure the ambient temperature. The size and power of the fan was chosen to provide a practical size for the radiation shield and to ensure an airflow speed of at least 3 m/s at the sensor.

The measurements were carried out at the outdoor test stand at the Campus Science Center of the Vienna University of Technology (see Figure 2). The test stand is a free-standing test building at 192 m above sea level (Adriatic Sea). The nearest building to the south is 10 m high and 40 m away. The south-facing facade of the test stand was painted half white and half black. Four temperature sensors were mounted on both sides: one sensor in a conventional non-ventilated radiation shield, one sensor in a ventilated radiation shield, one free-hanging sensor, each at a distance of 30 cm from the facade, and one surface temperature sensor (see Figures 3 and 4). The reference air temperature was measured in the 55 cm gap below the test stand in the shade. The wind velocity and direction were measured by a weather station on top of the test stand.

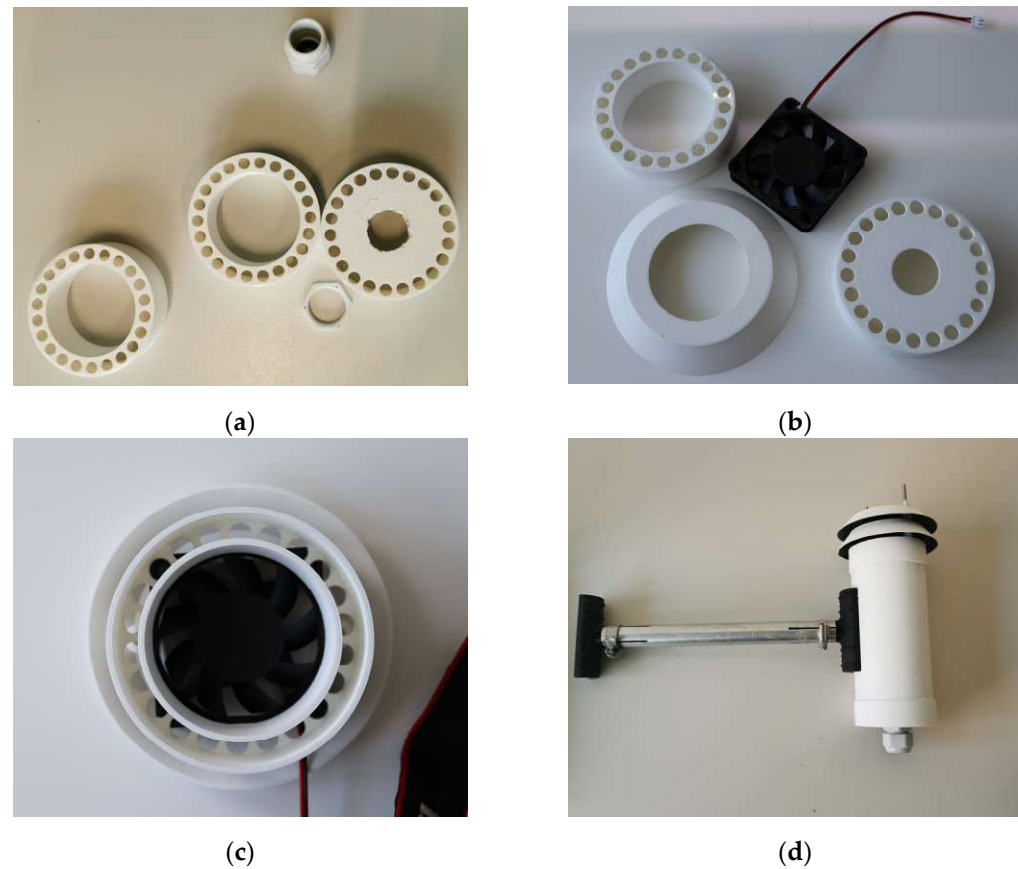


Figure 1. Assembly of the investigated ventilated radiation shields: (a) individual parts from the 3D printer; (b) individual parts including the fan for the lid; (c) assembled lid; (d) assembled radiation shield.

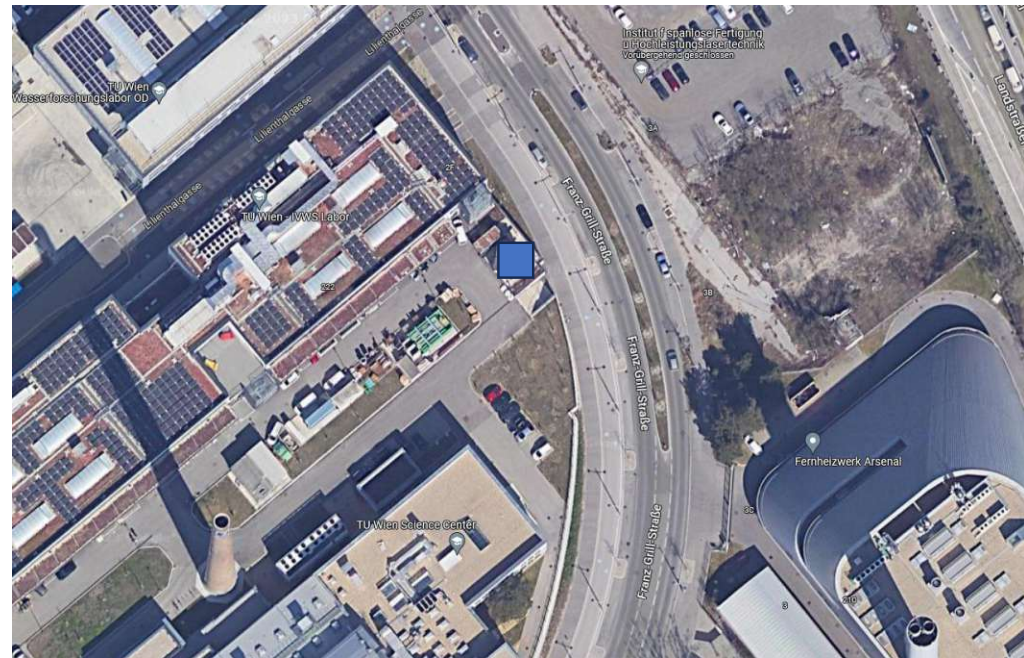


Figure 2. Location (blue square) and surroundings of the test stand at the Campus Science Center of the TU Wien [14].

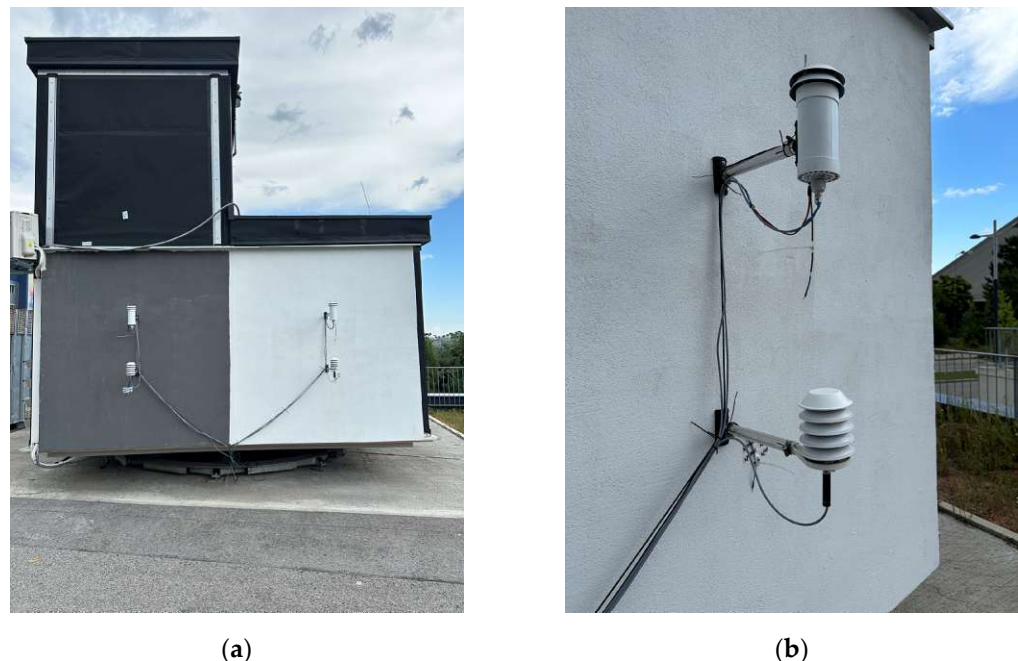


Figure 3. Set-up of the sensors at the test stand: (a) south facing facade of the test stand; (b) sensors on the white-painted part of the facade.

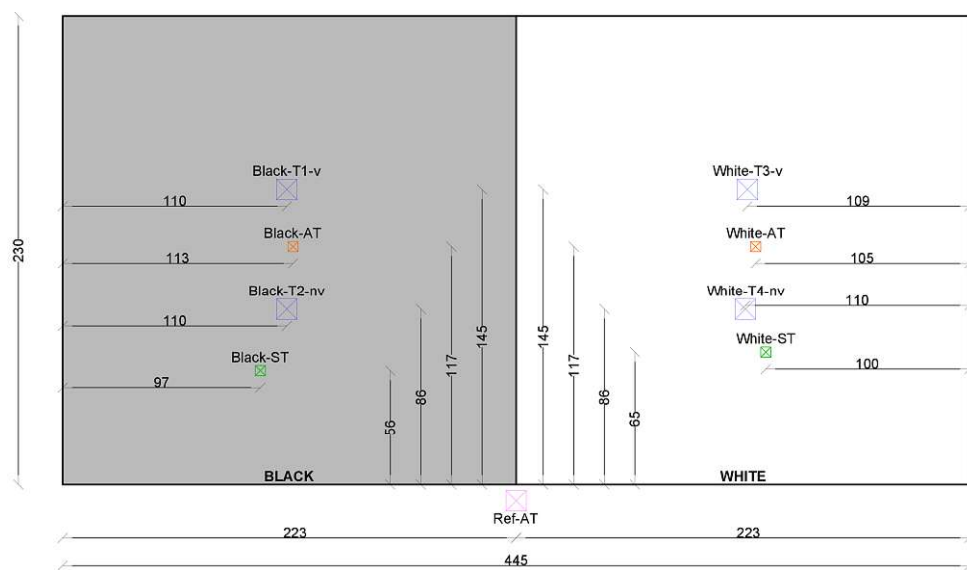


Figure 4. Scheme of the position of the sensors, with T1–T4 being the sensors within the ventilated (v) and non-ventilated (nv) radiation shields, AT being the air temperature sensors without a radiation shield, ST being the surface temperature sensors, and Ref-AT being the reference air temperature sensor.

The following instruments were used:

- Data logger, exporting the measurement data once a week;
- Temperature and humidity probes for temperatures from -40 to 60 $^{\circ}\text{C}$ and an accuracy at 23 $^{\circ}\text{C}$ of $\pm 0.5\%$ rh and ± 0.1 $^{\circ}\text{C}$ used for the sensors T1 to T4 as well as the reference temperature sensor;
- PT1000 probes (accuracy ± 0.3 $^{\circ}\text{C}$) used for the air temperature sensors without radiation shields as well as the surface temperature sensors;

- Weather station for wind measurement, using a solid-state magnetic sensor for wind speed (resolution 0.4 m/s and accuracy ± 0.9 m/s or $\pm 5\%$) and a wind vane with potentiometer for wind direction (display resolution 22.5° and accuracy $\pm 3^\circ$).

The temperature and humidity probes were calibrated at a temperature of 30°C and a humidity of 35, 50, and 70%rh using a humidity generator with a stability of 0.1%rh and 0.01°C . The measurements at the test stand were carried out in summer 2023 from 8 July to 27 August. After the measurements, all sensors were placed inside the test stand from 6 September to 11 September. Inside the test stand, the temperature was set to 22°C . All sensors recorded the same temperature.

Following the main measurements, another simplified measurement setup was installed to evaluate the validity of the reference temperature measurements under the test stand. For this purpose, three sensors were mounted next to each other centrally under the test stand, two of them without a radiation shield and one of them with a non-ventilated radiation shield. The temperatures were measured from 18 September to 20 September and compared to the temperature measurements of the ventilated sensor on the black facade (sensor Black-T1-v).

The evaluation of the measurement data is provided in the following section.

3. Results

The summer of 2023 was the seventh warmest summer in measurement history of Austria, with an average temperature 1.1 degrees above the average of the recent past (1991–2020) and 2.8 degrees above the mean compared with the 1961–1990 climate period [15]. The course of the air temperature (sensor Ref-AT) as well as the solar radiation (measured at a weather station in Unterlaa, Vienna, in a distance of 5 km) are shown in Figure 5. A comparison of the mean values of the air temperatures in front of the facade of the test stand for the entire measurement period with the mean temperature of the reference sensor under the test stand shows clear deviations for the freely suspended sensors without radiation shield (White-AT and Black-AT) of about +1.4 degrees (see Figure 6). For the sensors with radiation shielding (ventilated and non-ventilated), the mean deviations were within 0.1 degrees, with the sensor White-T3-v being the only sensor with a mean temperature below the temperature of Ref-AT.

For a detailed analysis of the temperature deviations of the different sensors in front of the test facade, in this study two representative model days were selected, which should represent summer days with clear skies, peak outdoor air temperatures, and high solar irradiation. The selected days were 27 July and 21 August. On 27 July, a moderate summer day with high solar irradiation, the reference temperature Ref-AT reached a maximum value of 26.2°C and the global radiation was up to 910 W/m^2 . On the other hand, 21 August was a hot summer day with a peak air temperature of 36.5°C and a maximum global radiation of 779 W/m^2 .

When looking at the temperature curves of the first reference day on 27 July (see Figure 7), a maximum temperature of the sensors White-AT and Black-AT (without radiation shield) of up to 32.5 and 32.8 degrees, respectively, can be seen. With a ventilated radiation shield, temperatures of only up to 27.4 degrees were measured in front of the black facade (Figure 7a), whereby the difference from the non-ventilated radiation shield was -0.3 degrees. In front of the white facade (Figure 7b), the maximum temperature with ventilated and non-ventilated radiation shields was 27.1 and 28.1 degrees, respectively. Compared to the maximum reference temperature under the test stand of 26.2°C , all sensors in front of the facade showed higher maximum values. A contrasting picture emerges during dusk, night, and dawn, from approximately 6 p.m. to 10 a.m. During these hours, the facade sensors measured temperatures up to 0.4 degrees lower than the reference sensor under the test stand. This could be due to the reduced sky view factor of the reference sensor and the long-wave radiation exchange between the test stand floor and the ground.

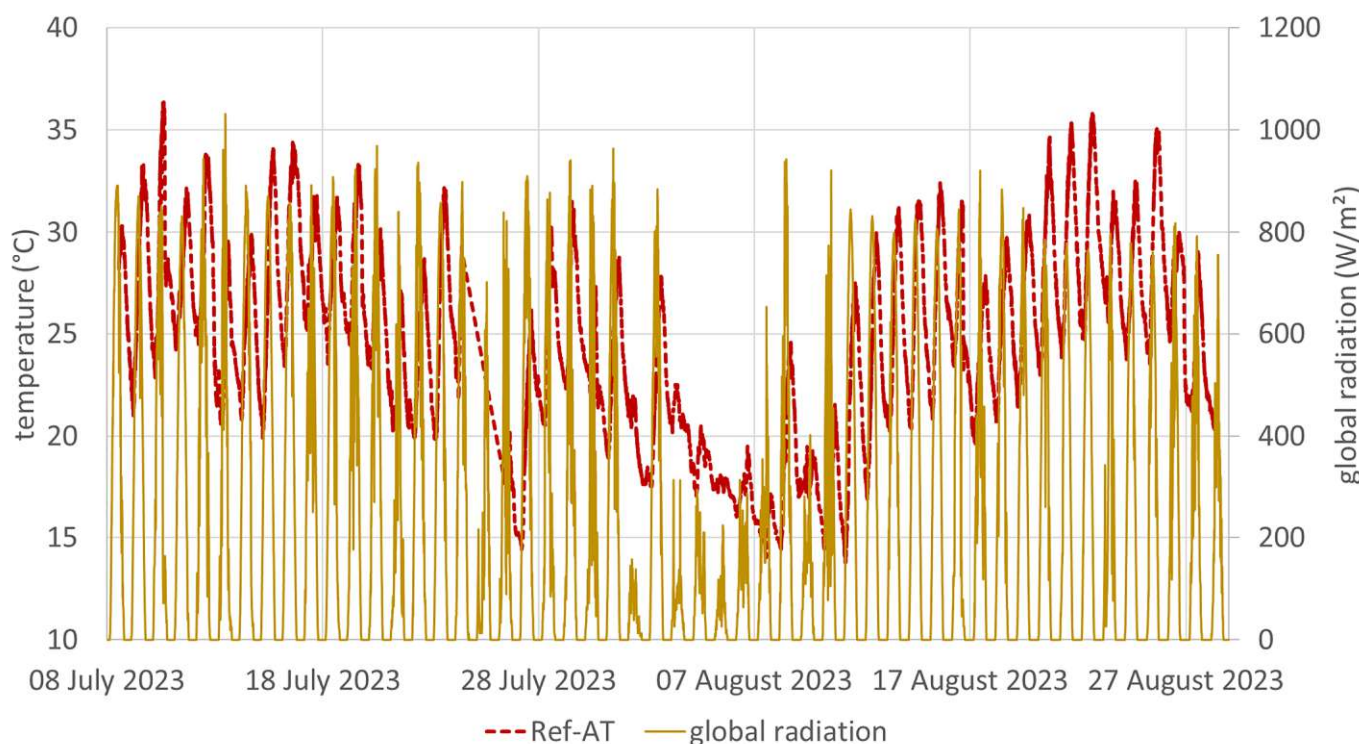


Figure 5. Air temperature (Ref-AT) at the test stand and global radiation of the weather station Wien Unterlaa from 8 July 2023 to 27 August 2023.

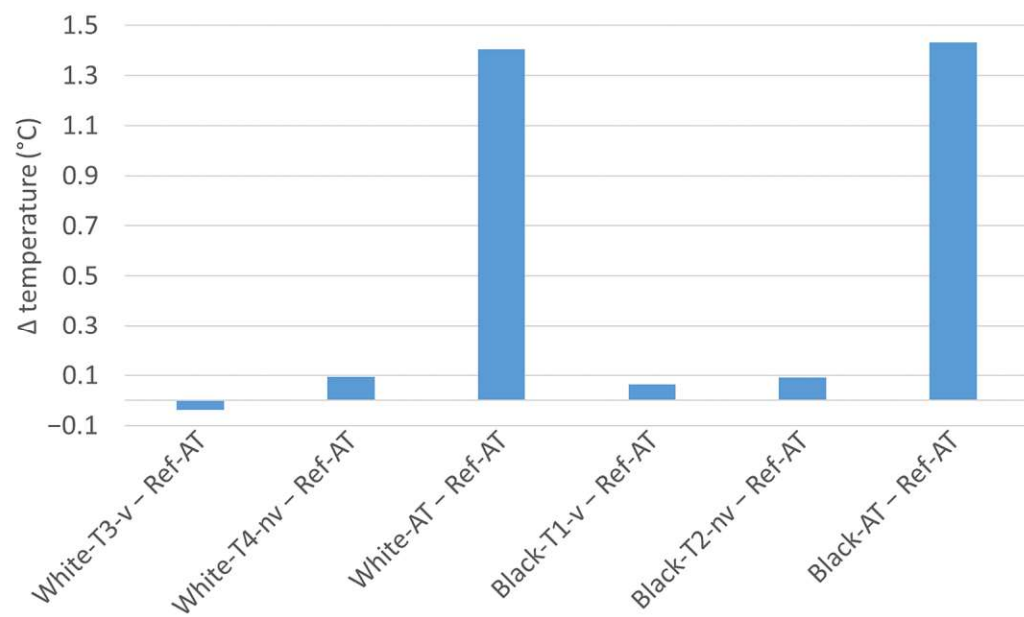


Figure 6. Differences in the mean temperatures of the sensors in front of the facade and the reference sensor below the test stand from 8 July 2023 to 28 August 2023.

The second reference day, 21 August, showed a similar course of temperatures, but with higher absolute values (see Figure 8), with a maximum reference temperature under the test stand reaching up to 36.5 °C. Also, the air temperatures in front of the white and black facade were elevated in both cases to 42.2 and 42.3 °C, respectively, without a radiation shield (White-AT and Black-AT); to 38.4 and 37.8 °C, respectively, with a non-ventilated radiation shield; and to 36.4 and 36.6 °C, respectively, with a ventilated radiation shield.

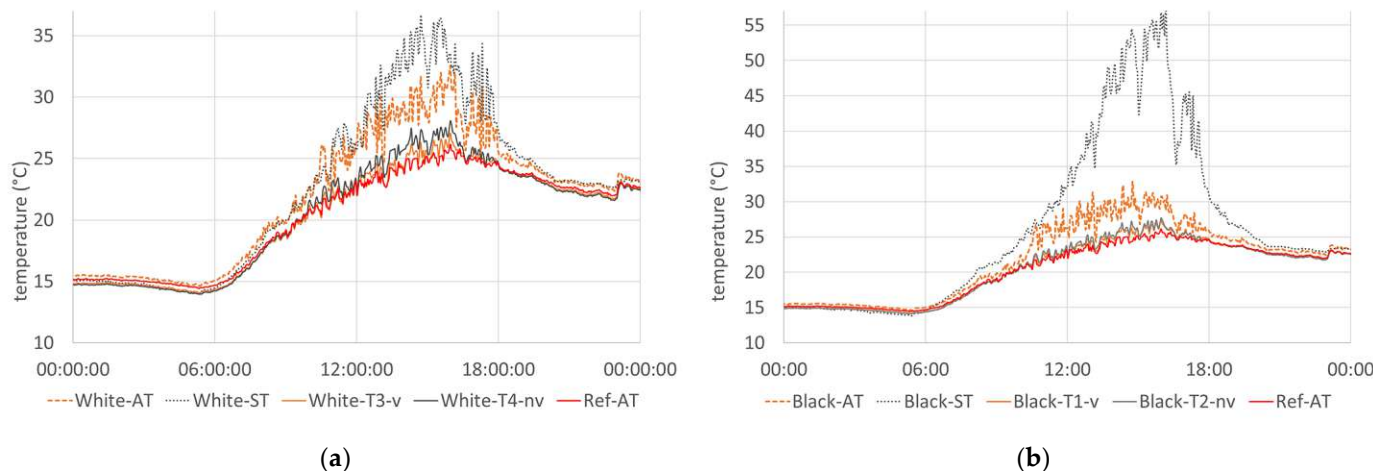


Figure 7. Measured temperatures on 27 July 2023: (a) temperatures of the sensors in front of the white facade; (b) temperatures of the sensors in front of the black facade.

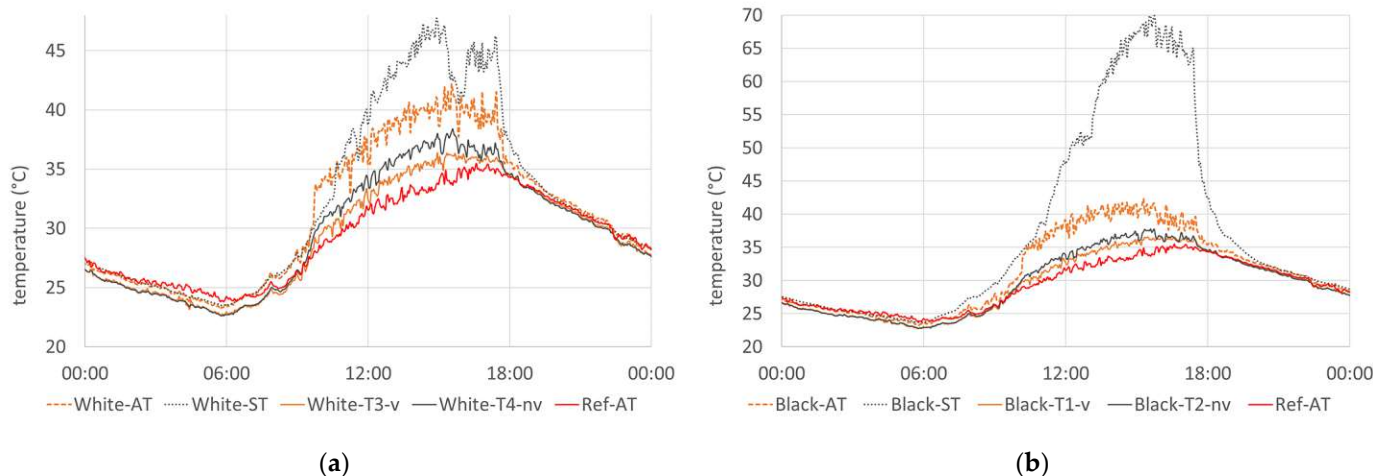


Figure 8. Measured temperatures on 21 August 2023: (a) temperatures of the sensors in front of the white facade; (b) temperatures of the sensors in front of the black facade.

Peak values of up to 36.7 and 47.7 degrees were measured on the surface of the white facade on 27 July and 21 August, respectively. On the surface of the black facade, temperatures reached up to 58.3 and 70.1 degrees on the two reference days, which was 21.6 and 22.4 degrees above the surface temperature values of the white facade.

The absolute deviation in the measured air temperatures of the non-ventilated sensors from the ventilated sensors in front of the black and white facade (Black-T2-nv–Black-T1-v and White-T4-nv–White-T3-v, respectively) is shown in Figure 9. On both reference days, higher daytime temperatures were recorded by the sensors with the non-ventilated radiation shield than by the sensors with the ventilated radiation shield. The deviation of up to 2.1 and 2.3 degrees in front of the white facade on 27 July and 21 August, respectively, was always greater than that for the sensors in front of the black facade, where the temperature differences were peaking at 1.0 and 1.6 degrees, respectively. The mean daytime temperature differences from 10 am until 6 pm were 0.2 and 0.8 degrees for the black and 0.7 and 1.2 degrees for the white facade on 27 July and 21 August, respectively. The higher values of temperature differences between ventilated and non-ventilated sensors in front of the white facade can be attributed to the higher reflection of solar radiation, leading to an increase in the radiation error of the non-ventilated radiation shields.

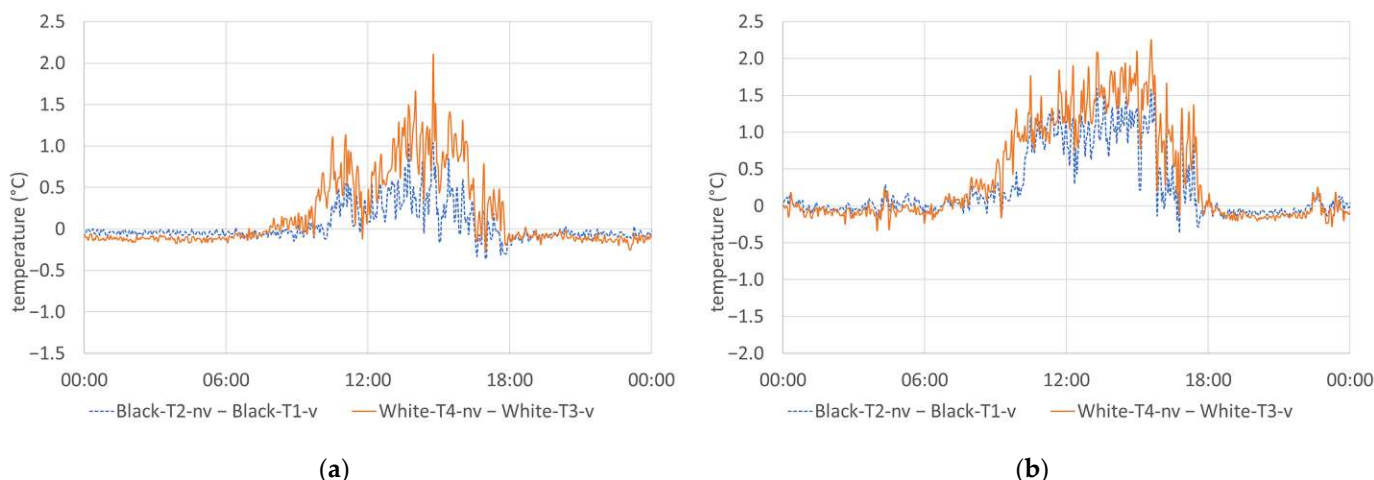


Figure 9. Measured temperature differences between non-ventilated and ventilated radiation shields in front of the black and the white facade: (a) 27 July 2023; (b) 21 August 2023.

During the night hours, however, the non-ventilated sensors tended to record slightly lower temperatures, which were, on both reference days, up to 0.3 and 0.4 degrees below the temperatures of the ventilated sensors in front of the white and black facade, respectively. This could be due to the effect of long wave radiation exchange with the sky, which becomes negligible in the case of ventilated radiation shields.

Compared with the reference temperature Ref-AT below the test stand, large deviations can be seen for both the non-ventilated and the ventilated sensors on both reference days (see Figure 10). The maximum deviation was 2.9 and 3.2 degrees between 2 p.m. and 4 p.m. local time on 27 July and 4.1 and 4.8 degrees on 21 August for the non-ventilated sensors in front of the black and white facade, respectively. For the ventilated sensors, the maximum deviation was still 1.9 and 2.0 degrees, respectively, on 27 July and 2.9 and 2.6 degrees, respectively, on 21 August.

On the other hand, during the night hours, between 7 p.m. and 9 a.m., the measured temperatures on the facade were up to 0.4 and 1.9 degrees lower than under the test stand on 27 July and 21 August, respectively.

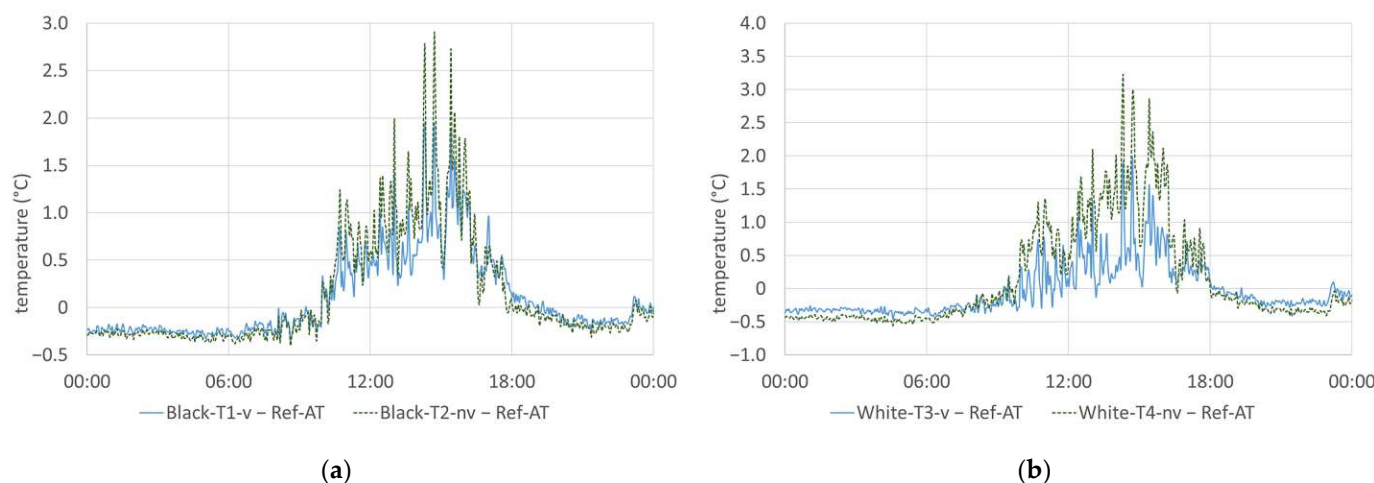


Figure 10. Cont.

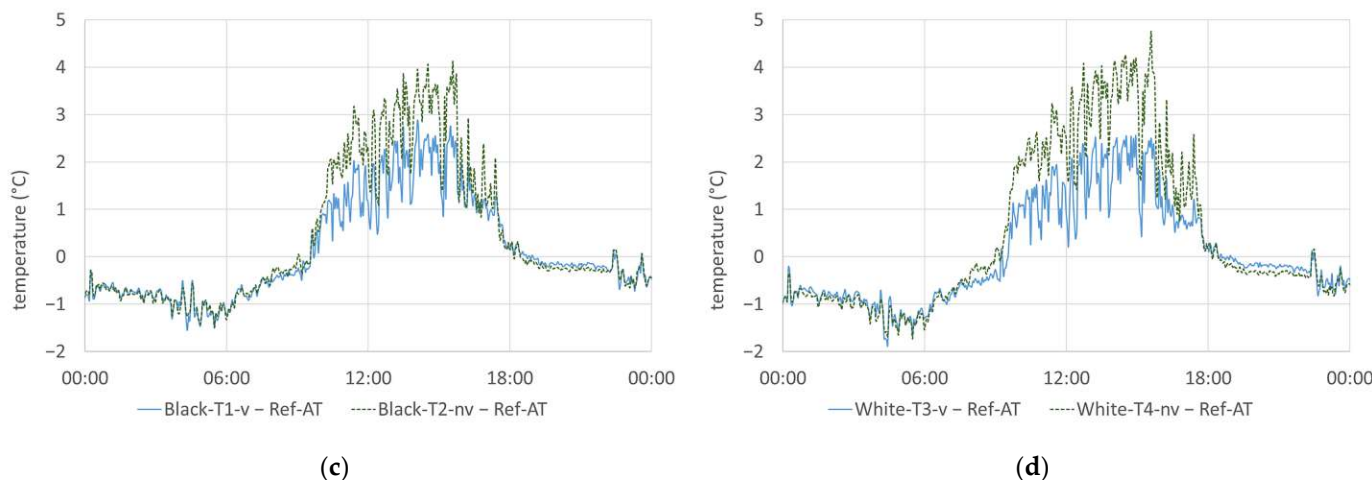


Figure 10. Deviation of the ventilated and non-ventilated sensors from the reference: (a) black facade—27 July 2023; (b) white facade—27 July 2023; (c) black facade—21 August 2023; (d) white facade—21 August 2023.

An analysis of the correlation of the temperature readings of the non-ventilated and the ventilated sensors over the entire measurement period shows for the white as well as the black facade a decrease in the correlation with increasing air temperature, with the scatter of the measured data increasing at the same time (see Figure 11). The reason for this is expected to be the increase in radiation error at increasing temperatures, which is more significant for the non-ventilated sensors than for the ventilated sensors. Comparing the white facade with the black facade, the radiation error is more significant in front of the white facade, with the trend line for the temperature difference between the ventilated and the non-ventilated sensor reaching $0.62\text{ }^{\circ}\text{C}$ at an air temperature (Ref-AT) of $36\text{ }^{\circ}\text{C}$. At the same air temperature, in front of the black facade the temperature difference was just $0.16\text{ }^{\circ}\text{C}$ (see Figure 12). The big scatter in the temperature differences at higher temperatures might also be explained by the increasing impact of the wind speed on the radiation errors: at low temperatures and subsequently low solar radiation, the radiation error is small, regardless of the wind speed; at higher temperatures, the radiation error remains low at high wind speeds—at low wind speeds, though, the radiation error increased proportional to solar irradiation. In all graphs in Figures 11 and 12, a red dotted line shows the linear trend line of the data, with the formula and the coefficient of determination shown in the bottom right.

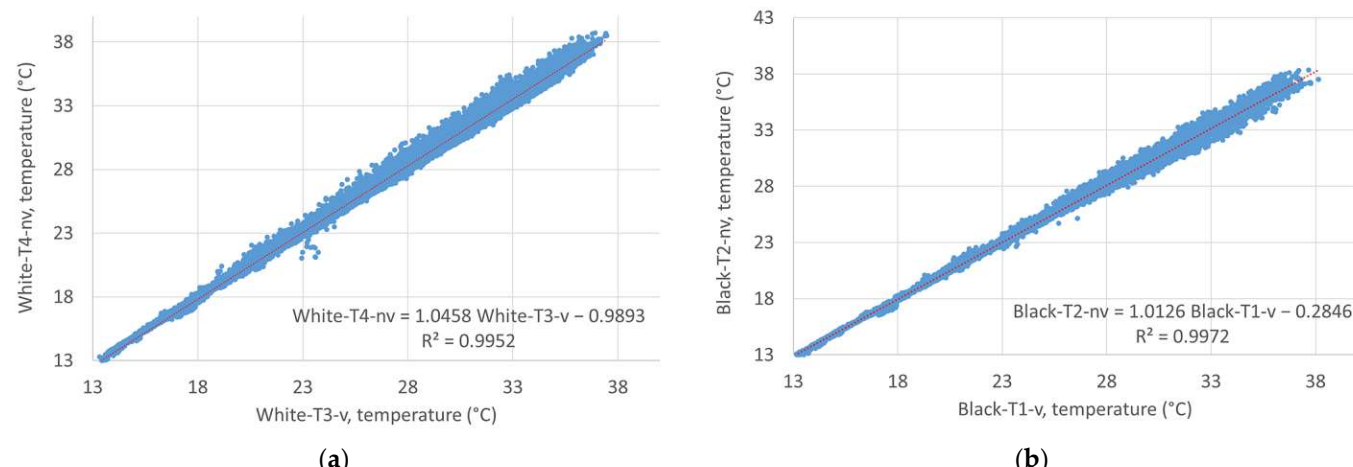


Figure 11. Correlation of the measurement values of the non-ventilated and ventilated sensors for the entire measurement period: (a) white facade; (b) black facade.

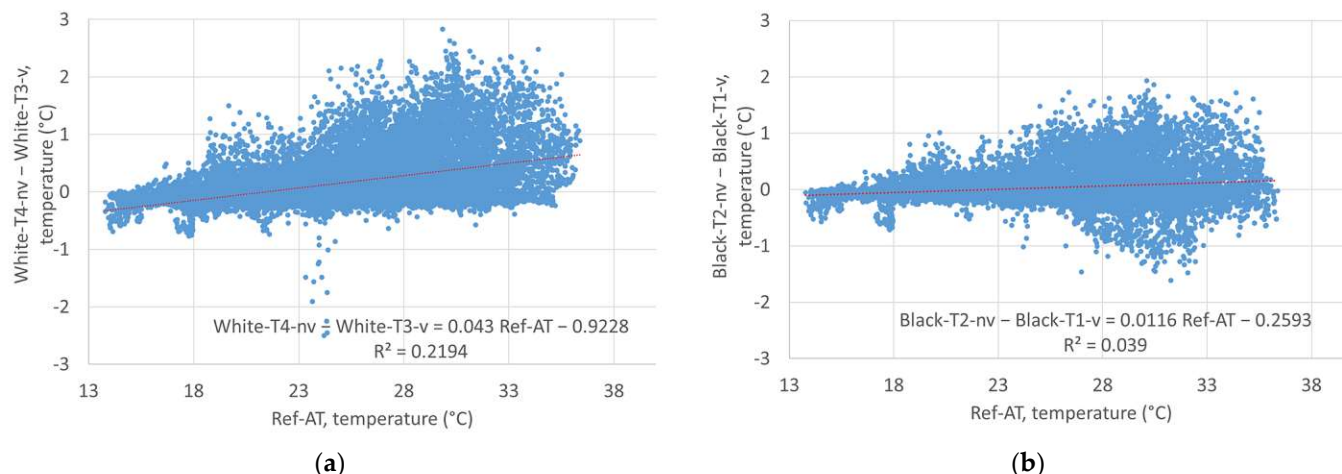


Figure 12. Temperature difference of the non-ventilated and ventilated sensors as a function of the reference temperature for the entire measurement period: (a) white facade; (b) black facade.

To assess the significance of the correlation between Ref-AT and the difference between “Black-T2-nv” and “Black-T1-v” as well as “White-T4-nv” and “White-T3-v”, Student’s *t*-test was used together with the Pearson correlation. The Pearson correlation showed a weak positive correlation between Ref-AT and the temperature differences for the white facade ($r = 0.1975$) and a medium correlation for the black facade ($r = 0.4683$). Student’s *t*-tests for dependent samples, between the measured values Black-T1-v and Black-T2-nv as well as between the measured values White-T3-v and White-T4-nv, showed a significant difference between the mean values. For Black-T1-v and Black-T2-nv the *t*-statistic was -13.68 , while for White-T3-v and White-T4-nv the *t*-statistic was -46.39 . In both cases, the *t*-statistics were significantly larger than the critical *t*-values for both one-sided and two-sided tests. This indicates that the difference between the means was significant in both cases. The *p*-values were extremely low (very close to or equal to zero), indicating that the null hypothesis that there is no difference between the means is rejected. Overall, the results of both *t*-tests show that there is a statistically significant difference between the mean values of the measurements with ventilated and non-ventilated radiation shields.

The correlation of the measured temperatures in front of the facade and under the test stand over the entire measurement period is shown in Figure 13 for the ventilated and non-ventilated sensors with linear trend lines for both the black and the white facade data. Again, the correlation was decreasing and the scatter increasing at higher temperatures, with the scatter of the non-ventilated sensors being greater.

In each case, the results of the Student’s *t*-test yielded *t*-statistics well outside the critical range for both one-sided and two-sided tests, and *p*-values close to zero, indicating that the probability of obtaining such results purely due to chance is negligible. Therefore, we can reject the null hypothesis and conclude that statistically significant differences exist between the mean values of the reference temperature Ref-AT and the temperatures Black-T1-v, Black-T2-nv, White-T3-v, and White-T4-nv.

The means, standard deviations, and 95% fractiles of the relative temperature differences of the ventilated and non-ventilated sensors in front of the white and black facade, as well as the respective differences to the reference sensor Ref-AT for the entire measurement period, are listed in Table 1. The mean values show very small temperature differences between -0.04 and $+0.13$ degrees due to the described phenomenon that the differences change the plus/minus sign at night hours. Accordingly, the standard deviations showed higher values between 0.28 and 1.01 degrees. Additionally, the 95% fractiles are included, stating that there is a 95% probability that the actual temperature differences will not exceed these values. In total, it can be stated that, in the case of non-ventilated radiation shields, the temperature differences, and thus the radiation errors, are bigger in front of the white facade compared to the black facade. As stated above, this phenomenon can be attributed

to the additional reflections of solar radiation reflected from the wall onto the sensors. Due to the higher reflectivity of the white facade, the influence on the radiation error is bigger. On the other hand, in the case of ventilated radiation shields, the radiation error was slightly bigger in front of the black facade, as the reflections from the facade became negligible due to the active ventilation of the radiation shields. Instead, the effect of the black facade heating up more due to a higher absorption of solar radiation and heating up the air in front of the facade at the same time seems to be predominant in this case.

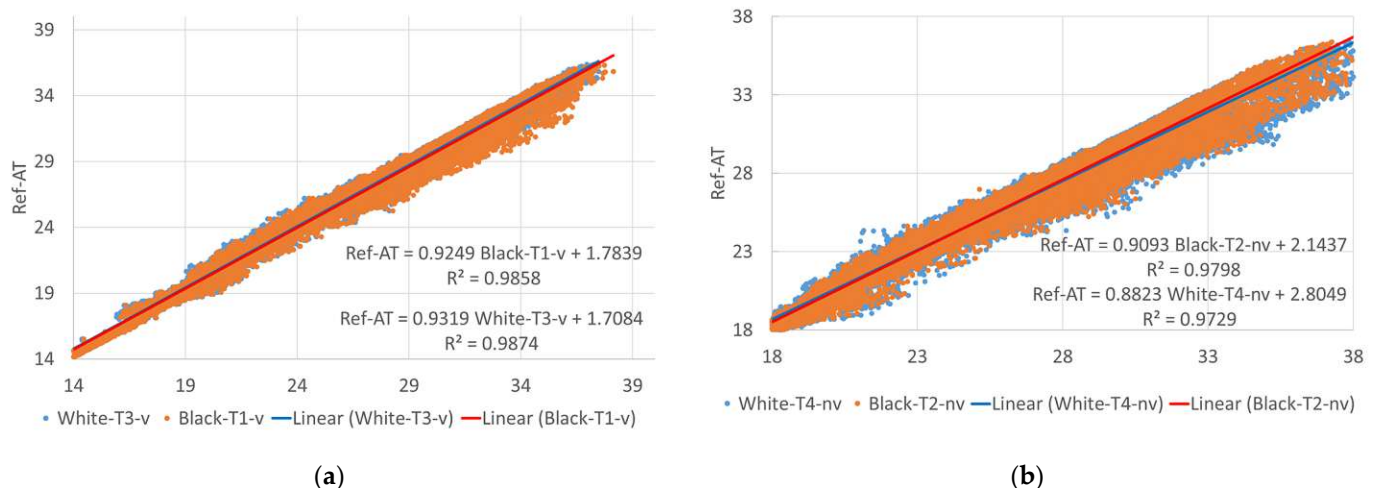


Figure 13. Correlation of the measurement values of the different sensors in front of the facade with the reference sensor Ref-AT below the test stand for the entire measurement period: (a) ventilated radiation shield; (b) non-ventilated radiation shield.

Table 1. Means, standard deviations, and 95% fractiles for the relative temperature differences of the ventilated and non-ventilated sensors in front of the white and black facade, and the reference from 8 July 2023 to 28 August 2023.

Values in °C	Black-T2-nv–Black-T1-v	Black-T1-v–Ref-AT	Black-T2-nv–Ref-AT
Mean	0.03	0.07	0.09
Standard deviation	0.28	0.69	0.83
95% fractile	0.63	1.51	1.95
	White-T4-nv–White-T3-v	White-T3-v–Ref-AT	White-T4-nv–Ref-AT
Mean	0.13	-0.04	0.10
Standard deviation	0.44	0.64	1.01
95% fractile	1.13	1.34	2.38

Based on the assumption that large scattering at higher temperatures, as seen especially in Figure 12, might be related to the current wind strength, the wind strength was also recorded from 13 August. The wind speed was recorded every ten minutes with one digit after the decimal point. Its course is shown in Figure 14, together with the reference air temperature Ref-AT. The highest wind speed recorded was 5.4 m/s, and the mean wind speed was 1.27 m/s, with the mean wind direction being approximately south (177°). Peak wind speeds were generally during daytime, frequently coinciding with peak temperatures.

With regard to the correlation of the wind speeds with the difference between the temperatures in front of the facade and underneath the test stand, there was a clear tendency for temperature differences to be lower at higher wind speeds (see Figure 15). This was most obvious for the non-ventilated sensor in front of the white facade, which showed the largest radiative errors at low wind speeds. At wind speeds close to zero, the temperature differences were often negative, which was due to the phenomenon observed during night hours with low wind, where temperatures below the test stand were higher than

in front of the facade. Therefore, these measurement data should not be considered for further analysis.

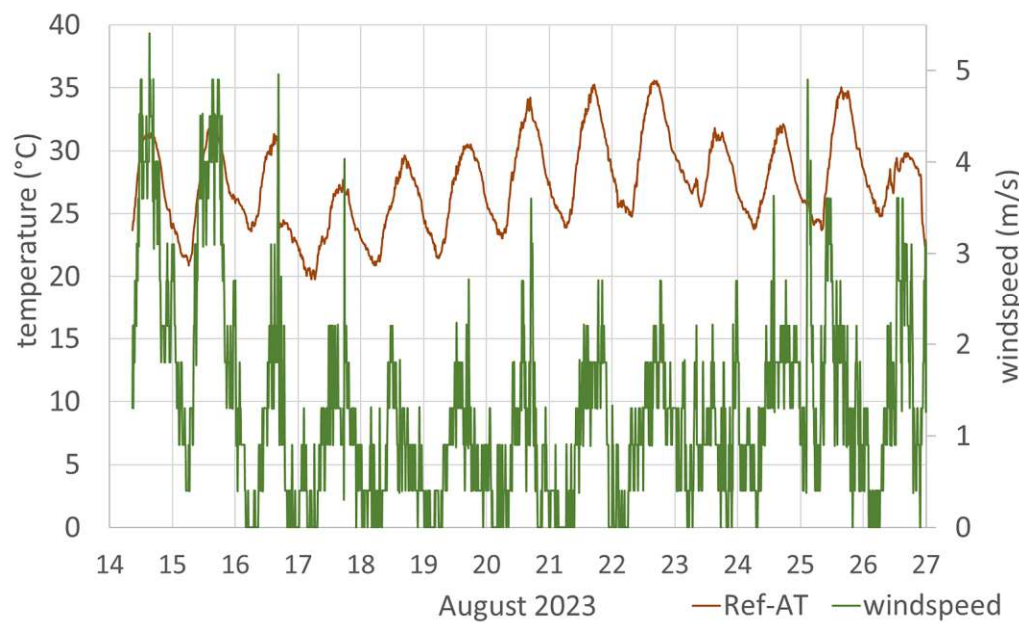


Figure 14. Air temperature (Ref-AT) and wind speed at the test stand from 14 August 2023 to 27 August 2023.

When grouping the measured data by wind speed, starting from the group 1–2 m/s, both the standard deviation and the 95% fractile values became smaller with increasing wind speed (see Table 2). A similar observation can be made for the mean values of the temperature differences. For the ventilated sensors, though, the mean values were almost constant for wind speeds from 1 to 5 m/s, which was due to their continuous mechanical ventilation. At the black facade, this resulted in a negative difference between the non-ventilated and the ventilated sensor at wind speeds above 3 m/s, indicating lower temperatures for the non-ventilated sensor. However, there is no explanation for this phenomenon at the present time.

Table 2. Means, standard deviations, and 95% fractiles of temperature differences depending on wind speed from 14 August 2023 to 27 August 2023.

Wind Speed	ms^{-1}	0–1	1–2	2–3	3–4	4–5
Black-T2-nv–Black-T1-v	°C	0.09; ± 0.26 ; 0.71	0.29; ± 0.42 ; 1.12	0.12; ± 0.36 ; 0.93	-0.06; ± 0.26 ; 0.62	-0.22; ± 0.12 ; -0.03
White-T4-nv–White-T3-v	°C	0.11; ± 0.42 ; 1.08	0.49; ± 0.64 ; 1.63	0.26; ± 0.53 ; 1.36	0.15; ± 0.36 ; 1.10	0.04; ± 0.17 ; 0.26
Black-T1-v–Ref-AT	°C	-0.23; ± 0.56 ; 0.92	0.50; ± 0.86 ; 2.10	0.48; ± 0.88 ; 2.23	0.53; ± 0.70 ; 2.21	0.49; ± 0.33 ; 0.85
Black-T2-nv–Ref-AT	°C	-0.15; ± 0.77 ; 1.70	0.79; ± 1.26 ; 3.19	0.61; ± 1.20 ; 3.14	0.47; ± 0.91 ; 2.81	0.27; ± 0.33 ; 0.53
White-T3-v–Ref-AT	°C	-0.31; ± 0.57 ; 0.90	0.41; ± 0.86 ; 2.02	0.40; ± 0.85 ; 2.13	0.42; ± 0.66 ; 2.04	0.36; ± 0.30 ; 0.66
White-T4-nv–Ref-AT	°C	-0.20; ± 0.92 ; 1.89	0.91; ± 1.46 ; 3.56	0.65; ± 1.36 ; 3.54	0.57; ± 1.00 ; 3.12	0.40; ± 0.41 ; 0.79

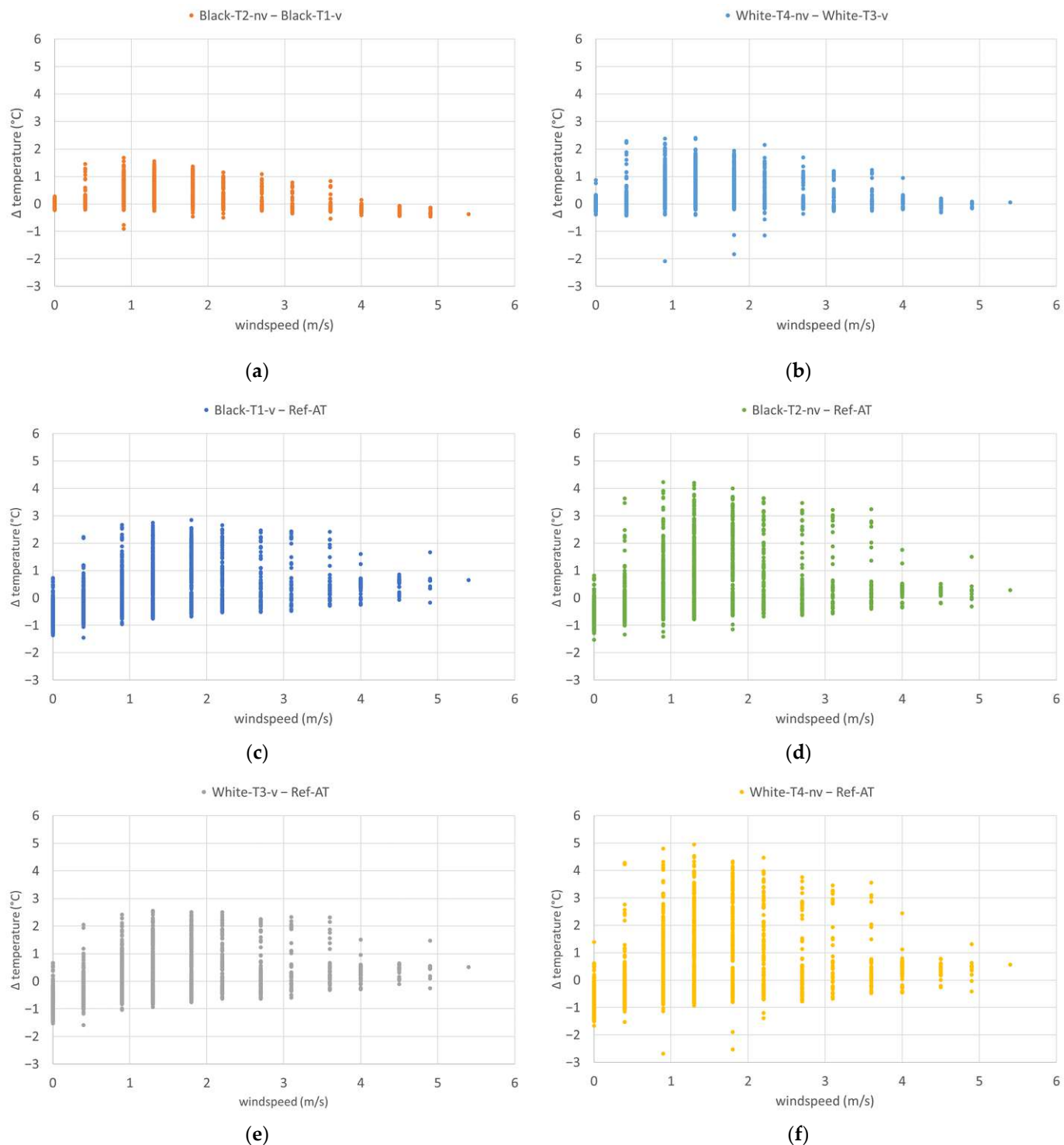


Figure 15. Temperature differences at different wind speeds from 14 August 2023 to 27 August 2023: (a) Black-T2-nv–Black-T1-v; (b) White-T4-nv–White-T3-v; (c) Black-T1-v–Ref-AT; (d) Black-T2-nv–Ref-AT; (e) White-T3-v–Ref-AT; (f) White-T4-nv–Ref-AT.

There is no group for wind speeds above 5 m/s, as there was only one datapoint available. In any case, it can be expected that temperature differences between ventilated and non-ventilated sensors become negligible at these wind speeds.

A detailed examination of temperature variations between the ventilated and non-ventilated sensors in relation to wind direction reveals a significant impact. Predominant wind directions at the research site included WNW, North, South-East, and SSE (see

Figure 16a). When winds originate from the north, sensors positioned in front of the south-facing facade are affected by wind shadows, resulting in implausible results (Figure 16b): elevated wind speeds atop the test stand roof correlate with increased temperature disparities, with ventilated sensors registering higher temperatures. Conversely, when the test facade faces winds from the SE and SSE, unventilated sensor temperatures consistently exceed those of ventilated sensors (Figure 16c). The radiation error, averaging below 0.2 degrees for wind speeds below 1 m/s, escalates to 0.56 and 0.82 degrees for wind speeds up to 2 m/s in front of the black and white facade, respectively. For wind speeds up to 4 m/s, the error decreases to 0.44 degrees in front of the black facade, holding relatively steady for sensors on the white facade. In the prevailing wind direction WNW, where the wind flows nearly parallel to the test facade, the most significant temperature differences of 0.15 degrees in front of the black facade and 0.36 degrees in front of the white facade occur at low wind speeds below 2 m/s (Figure 16d). At higher wind speeds of up to 5 m/s, these differences decrease to 0.04 degrees in front of the white facade, while turning negative in front of the black facade, indicating average temperatures recorded by ventilated sensors up to 0.24 degrees higher than those recorded by unventilated sensors.

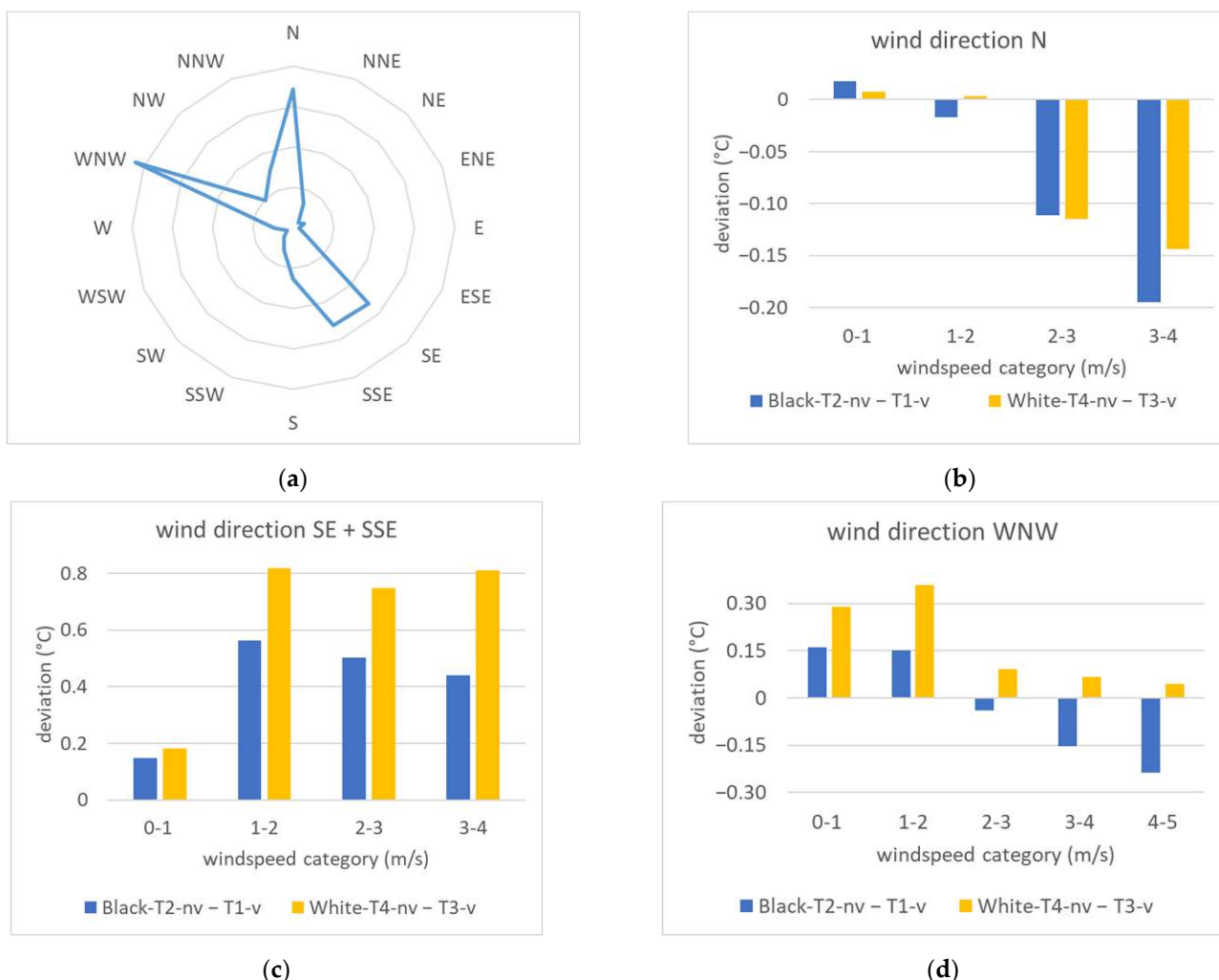


Figure 16. Temperature differences by wind direction with measurement data from 14 August 2023 to 27 August 2023: (a) wind rose; (b) temperature differences for north wind; (c) temperature differences for SE and SSE wind; (d) temperature differences for WNW wind.

4. Discussion

The findings of this study underscore the significant impact of direct solar radiation on the accuracy of temperature measurements, highlighting the crucial role of sensor ventilation influenced by prevailing wind conditions and built-in mechanical ventilation in radiation shields. In the absence of wind, non-ventilated radiation shields can lead to measurement errors of up to 5 degrees due to solar radiation. The utilization of ventilated radiation shields mitigates these errors; however, in the presence of direct irradiation on hot summer days, their radiation error can also reach up to 3 degrees. Achieving precision, with an accuracy of less than one degree, appears feasible only at high wind speeds exceeding 4 m/s.

Our observed measurement errors with a non-ventilated radiation shield align with the findings of Lin et al., who reported temperature errors of 2–4 degrees on clear, windless days at midday. This deviation corresponds to the air temperature measured with a ventilated US Climate Reference Network (CRN) shield ([7], p. 1224ff). Nakamura and Mahrt also based their evaluations on a sensor with a ventilated radiation shield, noting a radiation error of more than one degree in 2.6% of the measurement data, with individual points deviating by more than 2 degrees ([9], p. 1054). It is noteworthy that the inaccuracy of the ventilated radiation shield was not considered in the assessments of both studies.

Benchmarking the accuracy of temperature sensors against mechanically aspirated, shaded, multi-walled tubes, typically assumed to have negligible error ($<0.1\text{ }^{\circ}\text{C}$) ([8], p. 185), is a common approach. In this study, the reference sensor under the test stand met these criteria. The accuracy of all measurements at a distance of 30 cm in front of the facade was determined in relation to this reference sensor. Both non-ventilated and ventilated sensors exhibited significant measurement errors when air temperature was measured under direct solar radiation influence. The radiation error remained within ± 2.4 and ± 1.3 degrees in 95% of cases for non-ventilated and ventilated radiation shields, respectively, in front of the white facade. For the black facade, the errors were ± 2.0 and ± 1.5 degrees in 95% of cases. This emphasized the necessity for an additional reference measurement with a ventilated sensor in a permanently shaded position when measuring temperatures in the sun, allowing subsequent data correction.

Local wind speed emerged as a crucial parameter influencing temperature measurement accuracy. According to Kurzeja [8], reliable temperature readings are attainable at a wind speed of 1 m/s. Consistent with Nakamura and Mahrt ([9], p. 1056), a radiation error of 0.6 degrees occurred at wind speeds below 1 m/s, decreasing to 0.3 degrees at higher wind speeds. Richardson et al. [16] recorded air temperature errors of up to 1.8 degrees during windless periods. In both studies, the temperature reference is a temperature sensor in a mechanically aspirated shield which itself has an accuracy of 0.3 degrees and a radiation error of 0.2 degrees at 1000 W/m^2 [17]. In this study, the temperature differences of non-ventilated sensors compared to ventilated sensors were below 0.6 and $1.1\text{ }^{\circ}\text{C}$ for black and white facades, respectively, for 95% of cases. The most significant temperature differences (with 95% fractiles of 1.1 and $1.6\text{ }^{\circ}\text{C}$, respectively) occurred at wind speeds below 2 m/s, with differences within measurement accuracy at wind speeds exceeding 4 m/s.

The proximity of sensors to the facade may impact measurement accuracy, with lower wind speeds and solar reflections potentially introducing additional radiation errors. Conversely, depending on facade orientation, sensors in close proximity may experience more shading from the building, reducing exposure to direct solar radiation and thus lowering average radiation errors. Future studies should investigate the optimal distance between sensors and facades to minimize radiation errors. Additionally, the influence of wind direction on radiation errors near facades using ventilated radiation shields should be explored, potentially employing a weather station to measure wind speed and direction near temperature sensors positioned in front of the facade.

In conclusion, this study underscores the critical importance of ventilated radiation shields for achieving high-quality temperature measurements in the sun. Nevertheless,

ventilated shields can still lead to considerable radiation errors when fixed in front of a south-oriented facade. White facades may exacerbate errors due to additional reflections of solar radiation, while black facades introduce heating of the air layer, contributing to measurement errors. Future research should delve into evaluating radiation errors of different ventilated radiation shields and establishing requirements for reference temperature measurements when assessing temperatures in the sun. Establishing these measurement standards is essential for providing accurate temperature data to evaluate the impact of facade greening and other Urban Heat Island mitigation measures, crucial for guiding cities towards a sustainable future.

Author Contributions: Conceptualization, F.T.; methodology, A.P. and A.S.; formal analysis, F.T.; investigation, F.T.; resources, A.S.; data curation, A.P.; writing—original draft preparation, F.T.; writing—review and editing, F.T.; visualization, A.P.; supervision, A.K.; project administration, F.T. All authors have read and agreed to the published version of the manuscript.

Funding: Open Access Funding by TU Wien.

Institutional Review Board Statement: Not applicable.

Informed Consent Statement: Not applicable.

Data Availability Statement: The raw data supporting the conclusions of this article will be made available by the authors on request. The data are not publicly available due to confidentiality reasons.

Acknowledgments: Special thanks are due to Andras Horvath from Rheologic GmbH, 1060 Vienna, for his support in defining the test setup and his expertise in interpreting the test results.

Conflicts of Interest: The authors declare no conflicts of interest.

References

1. Teichmann, F.; Horvath, A.; Luisser, M.; Korjenic, A. The Impact of Small-Scale Greening on the Local Microclimate—A Case Study at Two School Buildings in Vienna. *Sustainability* **2022**, *14*, 13089. [[CrossRef](#)]
2. Teichmann, F.; Baumgartner, C.M.; Horvath, A.; Luisser, M.; Korjenic, A. Simulation of urban microclimate with uhiSolver: Software validation using simplified material data. *Ecol. Process.* **2021**, *10*, 67. [[CrossRef](#)]
3. Detommaso, M.; Costanzo, V.; Nocera, F. Application of weather data morphing for calibration of urban ENVI-met microclimate models. Results and critical issues. *Urban Clim.* **2021**, *38*, 100895. [[CrossRef](#)]
4. Avraham, M.; Yadid, H.; Blank, T.; Nemirovsky, Y. Air Temperature Measurement Using CMOS-SOI-MEMS Sensor Dubbed Digital TMOS. *Eng. Proc.* **2022**, *27*, 64. [[CrossRef](#)]
5. Erell, E.; Vi, V.; Leal, V.; Maldonado, E. Measurement of air temperature in the presence of a large radiant flux: An assessment of passively ventilated thermometer screens. *Bound. Layer Meteorol.* **2005**, *114*, 205–231. [[CrossRef](#)]
6. Lopardo, G.; Bertiglia, F.; Curci, S.; Roggero, G.; Merlone, A. Comparative analysis of the influence of solar radiation screen ageing on temperature measurements by means of weather stations. *Int. J. Climatol.* **2014**, *34*, 1297–1310. [[CrossRef](#)]
7. Lin, X.; Hubbard, K.G.; Baker, C.B. Surface air temperature records biased by snow-covered surface. *Int. J. Climatol.* **2005**, *25*, 1223–1236. [[CrossRef](#)]
8. Kurzeja, R. Accurate temperature measurements in a naturally-aspirated radiation shield. *Bound. Layer Meteorol.* **2010**, *134*, 181–193. [[CrossRef](#)]
9. Nakamura, R.; Mahrt, L. Air temperature measurement errors in naturally ventilated radiation shields. *J. Atmos. Ocean. Technol.* **2005**, *22*, 1046–1058. [[CrossRef](#)]
10. Cheng, X.; Su, D.; Li, D.; Chen, L.; Xu, W.; Yang, M.; Li, Y.; Yue, Z.; Wang, Z. An improved method for correction of air temperature measured using different radiation shields. *Adv. Atmos. Sci.* **2014**, *31*, 1460–1468. [[CrossRef](#)]
11. Liu, Q.; Jin, W.; Yang, J.; Zhu, H.; Dai, W. Design and Experiments of a Naturally-Ventilated Radiation Shield for Ground Temperature Measurement. *Atmosphere* **2023**, *14*, 523. [[CrossRef](#)]
12. R. M. Young Company. Aspirated Radiation Shield. Available online: <https://www.youngusa.com/product/aspirated-radiation-shield/> (accessed on 3 April 2023).
13. Apogee Instruments Inc. Aspirated Radiation Shield. Available online: <https://www.apogeeinstruments.com/aspirated-radiation-shield/> (accessed on 3 April 2023).
14. Google Maps. Available online: <https://www.google.at/maps/place/Lilienthalgasse,+1030+Wien/@48.1817342,16.3974312,184m/data=!3m1!1e3!4m6!3m5!1s0x476da9e71a64bcbf:0x42eab8b2870b4a56!8m2!3d48.1804589!4d16.3943432!16s/g/1tggmfzt?entry=tu> (accessed on 7 September 2023).
15. GeoSphere Austria. Siebtwärmlster Sommer der Messgeschichte. Available online: <https://www.zamg.ac.at/cms/de/klima/news/siebtwaermster-sommer-der-messgeschichte> (accessed on 23 October 2023).

16. Richardson, S.J.; Brock, F.V.; Semmer, S.R.; Jirak, C. Minimizing Errors Associated with Multiplate Radiation Shields. *J. Atmos. Ocean Technol.* **1999**, *16*, 1862–1872. [[CrossRef](#)]
17. Campbell Scientific, Inc. 43408-L. R. M. Young Aspirated Radiation Shield. Available online: <https://www.campbellsci.com/43408-shield> (accessed on 18 December 2023).

Disclaimer/Publisher's Note: The statements, opinions and data contained in all publications are solely those of the individual author(s) and contributor(s) and not of MDPI and/or the editor(s). MDPI and/or the editor(s) disclaim responsibility for any injury to people or property resulting from any ideas, methods, instructions or products referred to in the content.